UNIVERSITY OF NAIROBI

GEOPHYSICAL MAPPING OF SHALLOW STRUCTURES CONTROLLING GEOTHERMAL RESERVOIR RECHARGE IN EBURRU GEOTHERMAL FIELD, KENYA RIFT

BY

HENRY KUBAI MWAURA

I56/74227/2014

A dissertation submitted in partial fulfillment of the requirement for Master of Science degree in Geology (Applied Geophysics).

Department of Geology

November, 2016

DECLARATION

I declare that this dissertation is my original work and has not been submitted elsewhere for award of Master of Science degree. Where other people's work or my own work has been used, this has been acknowledged and referenced in accordance with the University of Nairobi's requirements.

Signature ……………………………………… Date ………………………………

Henry Kubai Mwaura

I56/74227/2014

Department of Geology

School of Physical Sciences

University of Nairobi

This dissertation is submitted with our approval as research supervisors: -

	Signature	Date
Prof. J.O. Barongo	……………	………………

Department of Geology

University of Nairobi

P.O BOX 30197-00100

Nairobi, Kenya

jbarongo@uonbi.ac.ke

Dr. Z.N. Kuria	……………….	………………

Department of Geology

University of Nairobi

P.O BOX 30197-00100

Nairobi, Kenya

kuriazack@yahoo.com

DEDICATION

I dedicate this dissertation to my dear Parents Mr. and Mrs. Wallace Mwaura and siblings Geoffrey, Leah, Monica and Titus.

ACKNOWLEDGEMENTS

First and foremost, my appreciation goes to Almighty God for His continued assistance, in particular, by provision of necessary resources for completion of this dissertation.

I wish to express my gratitude to my supervisors; Professor J.O. Barongo and Dr. Z.N. Kuria for their continued assistance and guidance which they have accorded me throughout the research.

I also wish to recognize the contribution from all members of staff in the Department of Geology for their moral support and peaceful environment they provided for me to work in.

I wish to recognize the assistance given to me by staff from KENGEN through provision of borehole logs from Eburru geothermal field.

Last but not least, I wish to thank my fellow students for their continued cooperation and insights during the research process.

ABSTRACT

Eburru Geothermal Field, herein referred to as the study area, that lies in the Kenya rift has been geophysically investigated. The aim of the research was to delineate shallow geological structures beneath Eburru geothermal field with a view to determining their influence to the recharge of Eburru geothermal reservoir. A total of 149 VES data were used to generate both 2D geo-resistivity sections and 3D images. From the research findings, it is envisaged that the study area is underlain by a three layered earth to a depth of about 1000 m. Cross cutting vertical geo-electric features are fault lines connecting shallow aquifers to deep aquifers. Pockets of low resistivity (< 10 Ωm) observed in the study area are possibly due to low temperature secondary minerals of clay such as smectite and illite. On the basis of these findings, it is noted that the geothermal reservoir is recharged through surface infiltration and deep faults. Thus, the deep faults facilitate connection of shallow and deep aquifers. Buried fissure have facilitated accumulation of water behind them and in some cases controlled groundwater flow.

TABLE OF CONTENTS

DECLARATION ii

DEDICATION iii

ACKNOWLEDGEMENTS iv

ABSTRACT v

LIST OF ABBREVIATIONS xii

CHAPTER 1.0: INTRODUCTION 1

1.1 Background 1

1.2 Problem Statement 2

1.3 Aim and Objectives 2

1.3.1 Aim 2

1.3.2 Specific Objectives 2

1.4 Research Questions 2

1.5 Justification and Significance of the Research 2

1.6 Outputs 3

1.7 Study Area 3

1.7.1 Location 3

1.7.2 Physiographic Features 3

1.7.3 Climate 4

1.7.4 Vegetation 6

1.7.5 Land Use and Land Resources 6

1.7.6 Drainage 6

1.7.7 Soils 6

1.8 Scope of the Research 8

CHAPTER 2.0: LITERATURE REVIEW 9

2.1 Introduction 9

2.2 Previous Studies 9

2.3 Geology, Structures and Hydrogeology 11
2.3.1 Geology 11
2.3.1.1 Regional Geology 11
2.3.1.2 Local Geology 12
2.3.1.3 Stratigraphy 13
2.3.1.4 Structures 15
2.3.1.5 Hydrothermal Alteration 15
2.3.2 Hydrogeology 15
2.4 Principles of Electrical Resistivity Method 16
2.4.1 General 16
2.4.2 Flow of Current into the Ground from a Single Electrode 16
2.4.3 Current Flow through a Wire 16
2.4.4 Potential of a Single Electrode 17
2.4.5 General Four Electrode Approach 18
2.4.6 Apparent Resistivity 19
2.4.7 True Resistivity 19
2.4.8 Vertical Electrical Sounding (VES) 20
2.4.9 Modeling 20
2.4.10 Apparent Resistivity Curve Types 21
2.4.11 Inversion 21
2.4.12 Factors determining Conductivity of Earth Materials 23
2.4.12.1 Porosity 23
2.4.12.2 Water Content 23
2.4.12.3 Temperature 23
CHAPTER 3.0: MATERIALS AND METHODS 24
3.1 Materials 24
3.1.1 Softwares 24

3.1.2 Hardware **24**

3.1.3 Data **24**

3.1.3.1 Open Source Databases **24**

3.1.3.2 Data from Company and Organization **25**

3.1.3.3 Data obtained from other Sources **25**

3.2 Methods **25**

3.2.1 Desktop Studies **25**

3.2.2 Data Acquisition **25**

3.2.2.1 Data Preparation **26**

3.2.3 Data Processing and Analysis **27**

3.2.3.1 Inversion **27**

3.2.3.2 2D Geo-section Section **27**

3.2.3.3 3D Visualization **28**

3.2.4 Piezometric Surface Map **28**

CHAPTER 4.0: RESULTS AND DISCUSSIONS **29**

4.1 Introduction **29**

4.2 Results **30**

4.2.1 Mode of Data Presentation **30**

4.2.2 2D Geo-electric Sections for Traverses within the Study Area **30**

4.2.2.1 Geo-electric Section along Traverse I-I′ **30**

4.2.2.2 Geo-electric Section along Traverse II-II′ **31**

4.2.2.3 Geo-electric Section along Traverse III-III′ **32**

4.2.2.4 Geo-electric Section along Traverse IV-IV′ **33**

4.2.3 Geo-electric Structure Beneath Block A **34**

4.2.3.1 Iso-resistivity Maps in Block A taken at 2000 m.a.s.l **34**

4.2.3.2 3D Visualization of Geo-electric Structure in Block A- Lines O-M-K **35**

4.2.4 Geo-electric Structure Beneath Block B **37**

4.2.4.1 Iso-resistivity Maps in Block B taken at 2000 m.a.s.l 37

4.2.4.2 Combined Lines I-H-G in Block B 37

4.2.5 Geo-electric Structure Beneath Block C 40

4.2.5.1 Iso-resistivity Maps in Block C taken at 2000 m.a.s.l 40

4.2.5.2 Combined Lines A-C-R in Block C 40

4.2.5.3 Geo-electric Structure Beneath Entire Study area 43

4.3 Discussions 45

4.3.1 Geo-electric Structure 45

4.3.2 Influence of Shallow Geo-electric Structure to Recharge of the Eburru Geothermal Reservoir 46

4.3.2.1 Correlation of Well EW-01 and Geo-electric Section along Survey Line R .. 46

4.3.2.2 Correlation of Well EW-02 and Geo-electric Section along Survey Line D .. 47

4.3.2.3 Correlation of Well EW-03 and Geo-electric Section along Survey Line H .. 48

4.3.2.4 Correlation of Well EW-04 and Geo-electric Section along Survey Line R .. 49

4.3.2.5 Correlation of Well EW-05 and Geo-electric Section along Survey Line A .. 50

4.3.2.6 Correlation of Well EW-06 and Geo-electric Section along Line A 51

4.3.3 Piezometric Surface Map 53

4.3.4 Shallow and Deep Aquifers 54

CHAPTER 5.0: CONCLUSIONS AND RECOMMENDATIONS 55

5.1 Conclusions 55

5.1.1 Shallow Geological Structures 55

5.1.2 Influence of Shallow Geological Structures to Recharge of Geothermal Reservoir ..55

5.1.3 Relationship between Shallow and Deep Aquifers 55

5.2 Recommendations 56

REFERENCES..57

LIST OF FIGURES

Figure 1.1: Location Map of the Study Area (Kariuki and Russell, 2007)......................................4

Figure 1.2: Eburru Rainfall Map in Millimeters per Year (Kariuki and Russell, 2007)...............5

Figure 1.3: Soil Map of the Study Area. The fine clays denote soils with high content of montmorillonite while clays have illite content (Kariuki and Russell, 2007)..................................7

Figure 2.1: Geological Map of Eburru geothermal field (Modified from Thompson (1956)).....14

Figure 2.2: Current Flow Distribution from a Point Source and the Resulting Equipotential surfaces (Aizebeokhai, 2010)..16

Figure 2.3: Electric Field Lines and Equipotential Surfaces around a Single Electrode at the Surface of a Uniform Half-space: (b) Source and (c) Sink: Modified from Lowrie (2007). 18

Figure 2.4: Electrode Configuration for Resistivity Measurement Consisting of two Pairs of Electrode (Current A, B and Potential Electrodes C, D)*(Lowrie, 200*7)..19

Figure 2.5: Common Apparent Resistivity Curves for a Layered Structure Consisting of Three Horizontal Layers (Lowrie, 2007)..21

Figure 2.6: A Sample Flow Chart for an Inverse Problem (Roy, 2008)..22

Figure 3.1: Location of Eburru Survey Lines, Traverses, Wells and Sounding Stations............26

Figure 3.2: A Sample of Inverted VES Data (A13) along Line A...27

Figure 3.3: A Sample of 2D geo-section along Survey Line H..28

Figure 4.1: Location of Blocks and Traverses utilized in this Study..29

Figure 4.2: 2D Geo-electric Section along Traverse *I-I'* Running in E-W direction....................31

Figure 4.3: 2D Geo-electric Section along Traverse *II-II'* Running in N-S direction...................32

Figure 4.4: 2D Geo-electric Section along Traverse *III-III'* (N-S)..33

Figure 4.5: 2D Geo-electric Section along Traverse *IV-IV'* in Block B (E-W)..............................34

Figure 4.6: Iso-resistivity Map in Block A taken at about 2000 m.a.s.l..35

Figure 4.7: 3D Visualization between Survey Lines O, M and K...36

Figure 4.8: Iso-resistivity Map in Block B taken at about 2000 m.a.s.l..37

Figure 4.9: 3D Visualization between Survey Lines I, H and G...39

Figure 4.10: Iso-resistivity Map in Block C taken at about 2000 m.a.s.l......................................40

Figure 4.11: 3D Visualization between Survey Lines A, C and R..42

Figure 4.12: 3D Visualization between Survey Lines O, K,-H and A...44

Figure 4.13: Comparison of Geological log of Well EW-01 and 2D geo-section along Survey Line R..47

Figure 4.14: Comparison of Geological log of Well EW-02 and 2D geo-section along Survey Line D.........48
Figure 4.15: Comparison of Geological log of Well EW-03 and 2D geo-section along Survey Line H.........49
Figure 4.16: Comparison of Geological log of Well EW-04 and 2D geo-section along Survey Line R.........50
Figure 4.17: Comparison of Geological log of Well EW-05 and 2D geo-section along Survey Line A.........51
Figure 4.18: Comparison of Geological log of Well EW-06 and 2D geo-section along Survey Line A.........52
Figure 4.19: A Piezometric Surface Map of Nakuru County. The Study area is marked in purple rectangle. 53

LIST OF APPENDICES

Appendix 1: FORTRAN Codes for Converting Raw VES Data for use in Earth Imager (Barongo, 2016) ii
Appendix 2: Modeled VES Data within the Study Area (Barongo, 1982)......... iii
Appendix 3: Hydrological Condition around L. Naivasha (Adapted from Reta, 2011) xii
Appendix 4: Eburru Geological Well Log Data (KENGEN, 1990)......... xiii
Appendix 5: Piezometric Data for the Larger Nakuru County (Courtesy of Water Resource Management Authority, n.d.) xv

LIST OF ABBREVIATIONS

Ωm	Ohms Metre
2D	Two Dimensional
3D	Three Dimensional
^0C	Degree Celsius
ALT.	Altitude
BH-No.	Borehole Number
CO_2	Carbon Dioxide
DEM	Digital Elevation Model
DC	Direct Current
DLAT.	Degree Latitude
DLONG.	Degree Longitude
E	East
Est.	Easting
E.R	Electrical Resistivity
ILRI	International Livestock Research Institute
KENGEN	Kenya Electricity Generating Company
L	Vertical line from the surface below each vertical electrical sounding station
Layer	Layer
m	Metres
Mbgl	Metre below ground level
MT	Magnetotellurics
mV	Microvolt
MW	Megawatt
Nthg.	Northing
O.L.S	Old Land Surfaces
N	North
R.M.S	Root Mean Square
S	South
SAS	Signal Averaging System
TEM	Transient Electromagnetic
W	West
W.R.L	Water Rest Level
WRMA	Water Resource Management Authority

CHAPTER 1.0: INTRODUCTION

1.1 Background

The East African Rift System (EARS) dissects Kenya in N-S direction. The Kenya part of the rift, herein referred to as the Kenya Rift Valley, has numerous geothermal manifestation in the form of fumaroles, geysers, surface alterations and hot water springs (Thompson and Dodson, 1963).

In the recent past, different government and international organization have embarked on promoting and advocating use of green energy. Geothermal energy is one of the most efficient sources of green energy. Formulation of carbon credits policy has also attracted numerous private and public entities to compete for these credits hence the need to clearly define geothermal fields within the Kenya rift valley of which Eburru is one of them.

There have been various geophysical surveys carried out in Eburru geothermal field together with drilling of six wells in the same area and out of the six wells drilled, only three wells discharged with temperature above 180^0C (Mwarania, 2014).

The Kenya Rift Valley has a potential for geothermal energy of over 10000 MW (Mburu, 2009). Currently, Eburru geothermal field is producing 2.5MW at well EW-01 while well EW-04 and EW-06 have not been developed for production (see Figure 1.1). Due to increased drilling for geothermal resources in the region, there is a need to map geological structures that affect recharge into the Eburru geothermal reservoir.

In this research, the direct current method, in particular the vertical electrical sounding data was utilized in order to delineate resistivity structures beneath Eburru geothermal prospects. Thomas (2002) suggested that the vertical electrical resistivity method gives higher resolution in terms of resistivity for the first few metres below the surface, as opposed to Transient Electromagnetic Methods (TEM). Vertical electrical sounding data is considered accurate especially in locating aquifers (Loke, 2001) that are in part related to geothermal systems.

1.2 Problem Statement

Over the years, various geophysical surveys have been carried out in Eburru geothermal field and out of six wells previously drilled in the area, only three wells discharged (Omenda and Karingithi, 1993).

Most of previous studies focused on deep geological structures hosting geothermal resources with little attention paid to shallow geological structures (Omiti, 2013; Onacha, 1990 and Mwangi, 2012).

This research has utilized the vertical electrical sounding method to delineate shallow geological structures and assessed their contribution to the recharge of Eburru geothermal reservoir.

1.3 Aim and Objectives

1.3.1 Aim

The aim of this research was to delineate shallow geological structures beneath Eburru geothermal fields with a view to determining their potential influence on the recharge of geothermal reservoir underneath.

1.3.2 Specific Objectives

- To determine the shallow geo-electric structure beneath the Eburru Geothermal field.
- To determine the influence of the shallow geo-electric structures on the recharge of geothermal reservoir.
- To determine the relationship between shallow and deep aquifers.

1.4 Research Questions

1. What is the geo-electric structure of the study area?
2. Do shallow geological structures beneath Eburru geothermal field affect the deep geothermal reservoir?
3. Are there shallow aquifers in the study area and how do they relate with deep aquifers?

1.5 Justification and Significance of the Research

Out of six wells previously drilled in Eburru geothermal field, only three wells discharged (Omenda and Karingithi, 1993). One of the reasons for failure could be attributed to lack of information on shallow geological structures and their influence on the recharge of geothermal reservoir. This research explored the contribution of shallow geological structures to recharge of Eburru geothermal reservoir.

The vertical electrical sounding method was adopted since it gives high resolution for shallow geological structures. Other methods such as TEM and MT are useful for detecting deep geological structures but have poor resolution for shallow structures.

The research findings will contribute to knowledge and understanding of how shallow geological structures affect the recharge of a geothermal reservoir and thus, optimizing the geothermal resource.

With the understanding of how shallow geological structures influence recharge of geothermal reservoir, more geothermal energy rich areas are likely to be discovered and brought to production hence benefiting the local community and the country at large.

1.6 Outputs

The following is summary of outputs based on the stated objectives: -

- 2D and 3D images of the shallow geo-electric structure beneath Eburru Geothermal prospect.
- A piezometric surface map of the larger Nakuru County.
- A final report with conclusions and recommendations.

1.7 Study Area

1.7.1 Location

The present research project is confined within Eburru geothermal field, Nakuru County. It is bounded by longitudes $36^0 13'3.8''$E and $36^0 19'11.73''$E and latitudes $0^0 34'11''$S and $0^0 39'45''$S as shown in Figure 1.1.

1.7.2 Physiographic Features

The study area has several surface geological features that include: - craters, Eburru Mountain, portion of the badland mountain, dry river valley, altered grounds and fumaroles among others.

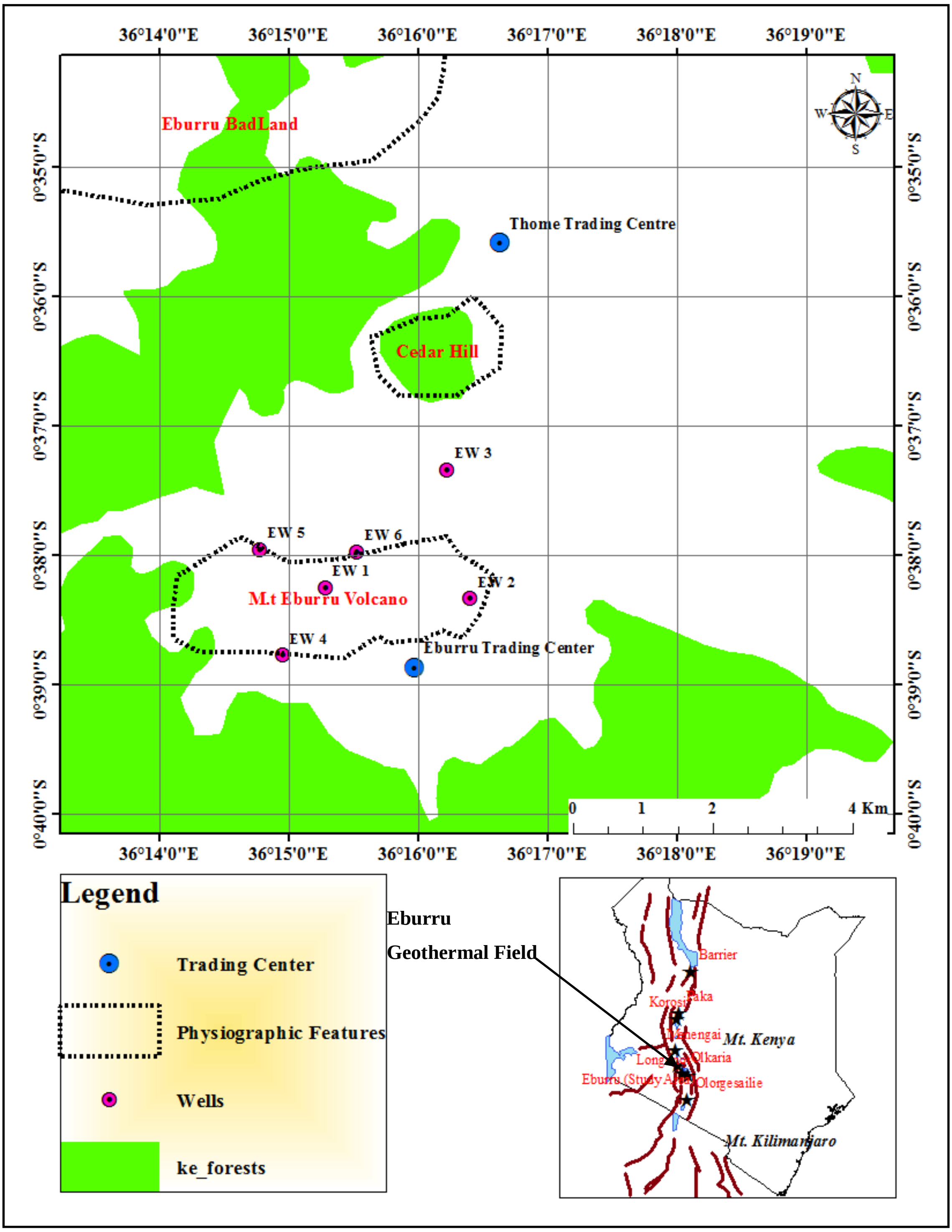

Figure 1.1: Location Map of the Study Area (Kariuki and Russell, 2007)

1.7.3 Climate

The area experiences a bimodal rainfall; long rains (April-June) and short rains (October-November). The average rainfall is well over 800mm but reduces towards the low lying areas of the Elementaita badland (Figure 1.2).

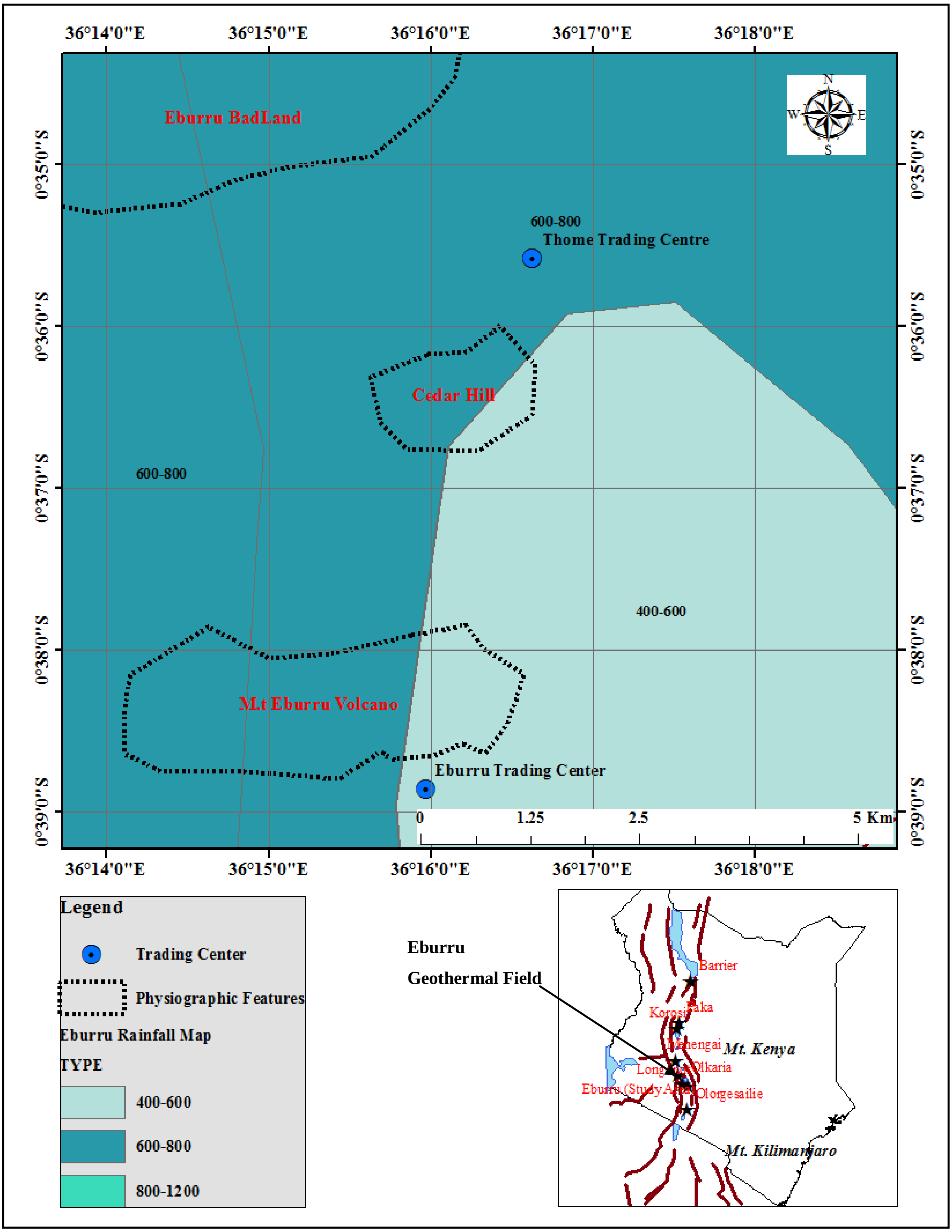

Figure 1.2: Eburru Rainfall Map in Millimeters per Year (Kariuki and Russell, 2007)

1.7.4 Vegetation

Eburru geothermal field comprises two distinct vegetation types based on elevation. The area towards Eburru Mountain has thick forests (Figure 1.1) as compared to the low lying areas towards Lake Naivasha and badland area.

1.7.5 Land Use and Land Resources

The study area is mainly hilly and forested precluding it from extensive agricultural activities. The badland area is less fertile compared to the Eburru station and only support grazing lands. Other than agricultural activities, the area is richly endowed with natural resources mainly geothermal steam. A 2.5MW power plant is in the process of being developed by KENGEN for production of clean energy.

1.7.6 Drainage

Eburru geothermal field forms a hydro-geological divide between Lake Naivasha and Lake Elmenteita drainage basins where shallow aquifers discharges on either side of the two basins (Mang'erere, 2005). The area generally lacks perennial surface flows except the surface runoff flows that occur during rainy season. Faulting has greatly influenced the drainage pattern in the entire region (Thompson and Dodson, 1963).

1.7.7 Soils

The soil characteristic is influenced by the nature of terrain, amount of infiltrating water, parent rock and vegetation covers. The study area has steep slopes, low lying and gentle slopes resulting in the formation of three types of soil (Clayey, sandy and loamy soil) as illustrated in Figure 1.3. The dominant rock types are the pyroclastic that have yielded clayey soils. Loamy soil, on the other hand is a product of deep weathering of iron rich rocks in the sub-humid part of the study area.

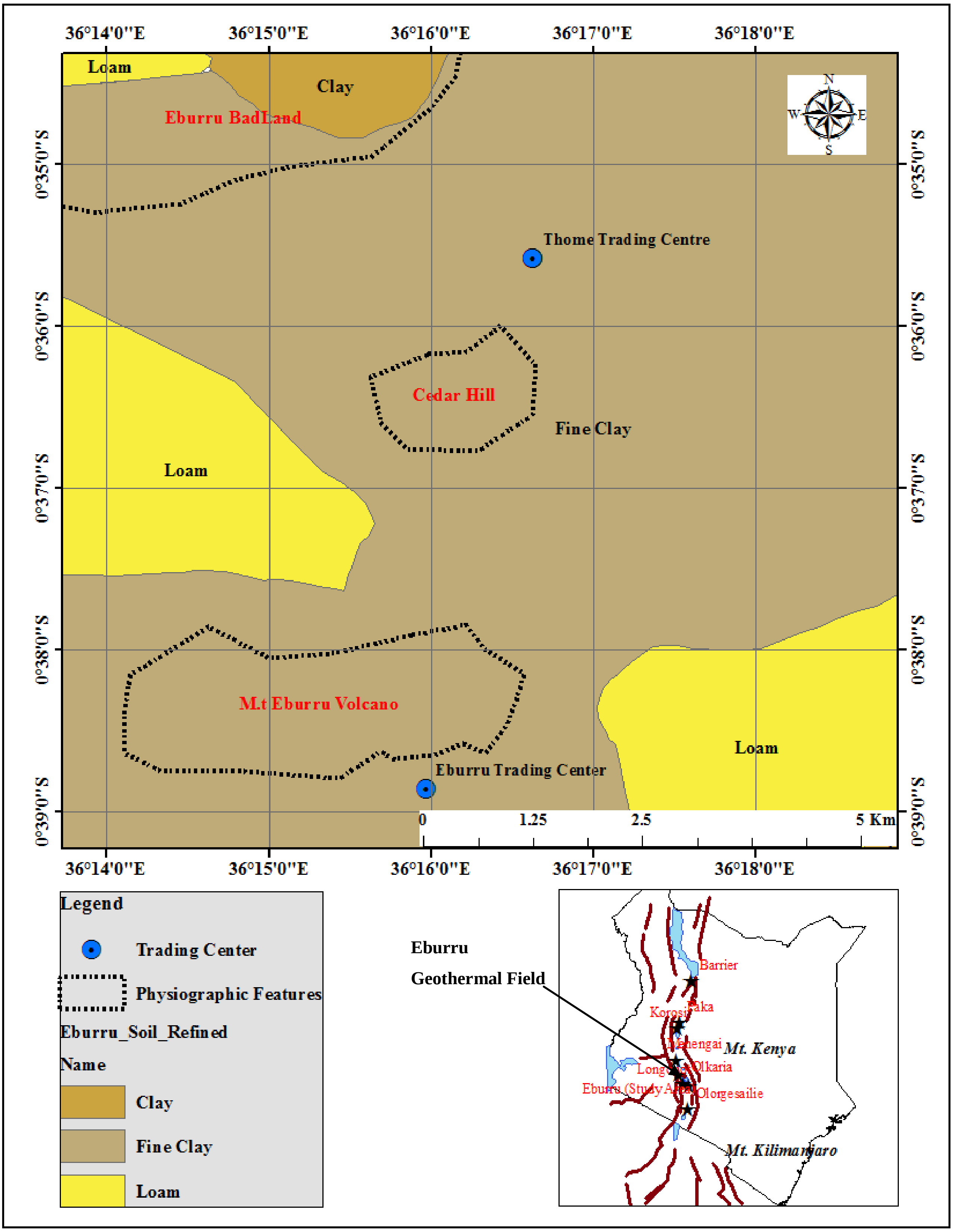

Figure 1.3: Soil Map of the Study Area. The fine clays denote soils with high content of montmorillonite while clays have illite content (Kariuki and Russell, 2007)

1.8 Scope of the Research

The study area is confined around Eburru geothermal prospect and covers approximately 99 km^2. The research involved analysis and interpretation of existing secondary data. VES data was used to identify 2D and 3D geo-electric structures in the Eburru geothermal prospects. In addition, borehole data was used to constrain the inversion process.

CHAPTER 2.0: LITERATURE REVIEW

2.1 Introduction

Several studies have been carried out in or near the study area with a view to determine different aspects: Geology, geothermal exploration methods, geothermal potential and hydro-geological condition.

2.2 Previous Studies

Barongo (1982) conducted a geophysical survey at Eburru geothermal prospect in 1981 and 1982. The report confirmed presence of a high geothermal potential in the southern region. The report also indicated high probability for geothermal potential in the central and northern regions of the study area.

Onacha (1990) noticed that lower resistivity below 1000 m a.s.l. in the Badlands region, might be an indication of either higher temperature or permeability. A critical observation in his project is that resistivity of between 20 Ωm -100 Ωm for layers at depth represents areas of temperature between 50^0 -150^0C depending on the permeability distribution and degree of hydrothermal alterations. He recommended a combination of Schlumberger, MT and TEM methods in order to clearly map the geothermal boundaries.

Lagat (2003) used piezometric levels where he observed that water flows into the floor of the rift in lateral direction but discharge axially. He observed that water flows through deeply fractured trachyte that is forms the main pre-shied building volcanic and a host of most of the geothermal systems.

Kuria (2011) used aeromagnetic data to determine seismo-tectonic characteristics of the Southern Kenya rift. He established that Eburru geothermal field has slightly thinner magnetic crust as compared to the neighboring Olkaria, Suswa and Longonot geothermal fields.

Mwangi (2012) observed that Eburru geothermal field has three distinct resistivity zones namely; a resistivity of about 10 Ωm representing the surface alteration, a conductive layer of over 10 Ωm dominated by smectites and zeolites enclosing the geothermal reservoir, and a third zone representing the heat source of Eburru geothermal field.

Omiti (2013) used 43 TEM and 45 MT soundings to map out the boundaries of Eburru geothermal field. He observed a five layer model that sharply contrasts observations made by Mwangi (2012).

Mulwa and Mariita (2013) did an integrated geophysical study in Bogoria basin using gravity and MT methods to a depth of ≈12 km where they observed a 3 layered earth. They concluded that the main geothermal reservoir is hosted within the fractured basement system.

In their work at Hamam Faraun in Sinai, Egypt, (El-Qady et al., 2000) utilized the power of 2D inversion of vertical electrical sounding data to delineate geothermal systems, geological structures and aquifers present.

Leli et al. (2003) demonstrated the usefulness of a priori information for constraining the inversion process. They observed that even though the inversion process gives a rough image of the target structure, incorporation of information such as well log, shape of the body and expected electrical resistivity properties of a geo-structure help in resolving them well.

Ha (1997) utilized 43 Schlumberger sounding data to locate a geothermal reservoir and associated structures in Reykjavik, Iceland. He then compared the results of a pair of schlumberger sounding and TEM methods where he concluded that the Schlumberger sounding method gave better resolution for shallow structures.

Odada et al. (2005) during the 11th World lake conference indicated that fresh lakes that are on a high topographic elevation, drain their water through surface out flow or ground water flow.

Aguado (2010) utilized the vertical electrical sounding data in Los Azufres, Mexico to delineate hydrothermal minerals that are associated with geothermal systems. He observed that the vertical electrical sounding is able to map both low and high conductive subsurface geo-structures.

Olaka (2011) did a study on vulnerability of east African lakes by using hydro-geological data where she established that Paleo-lake Naivasha discharged in to Lake Nakuru and Elmenteita in the Holocene during high volume season.

In his thesis, Reta (2011) did a water balance analysis between surface water flow in Lake Naivasha and subsurface water outflow. He observed that Lake Naivasha is not salty as many other lakes in the floor of the rift valley yet it does not have surface outflows. In his works, he concluded that there is substantive subsurface out flow into deep aquifers of Olkaria and Eburru geothermal fields as illustrated in Appendix 3.

In their work, Flores and López-moya (2011) did a comparison between three geo-electric methods in shallow subsurface investigation. They found out that the VES method gave better resolution for shallow geo-structures and was not affected much by conduction inconsistencies.

In their work in Iceland, Harðarson et al. (2012) utilized resistivity surveying and electromagnetic methods to delineate geothermal resources and associated geo-structures. They observed that these methods are highly reactive to changes in temperature and hydrothermal alteration activities.

2.3 Geology, Structures and Hydrogeology

2.3.1 Geology

The geology of the study area is covered in Geology of Naivasha area report no.55; degree sheet 43 S.W (Thompson and Dodson, 1963). The geology of the study area is captured on both regional and local scale.

2.3.1.1 Regional Geology

Eburru is part of the southern section of the Kenya rift system. The rift valley is a product of several interconnected geological activities. They are divided into: Doming, rifting and alkali magmatism (Saemundsson, 2008). Crustal doming results from the action of hotspots within the mantle. The rising and falling of the crust, result to formation of fractures that provide pathways for intruding magma. Subsequent eruption leads to emptying of magma chambers. Collapsing magma chamber leads to formation of fault lines and graben structures.

The Kenya Rift Valley was formed approximately 2 million years ago during late Pleistocene and has shown continued activity till present. The rifting process started in the northern part of Turkana and proceeded southwards. This is evidenced by presence of active geothermal features that include: fumaroles, geysers, altered grounds and hot springs that are common features in the southern Kenya and northern Tanzania. Surface manifestation of these geological features on the surface is a clear indication of ongoing rifting activities.

The fact that Eburru volcanic centres form the highest peaks in the entire Kenya rift is a clear indication that the main magma upwelling is centered in this area. Presence of several volcanic craters in the Eburru geothermal field indicates that the area underlay one of the most geologically active areas.

2.3.1.2 Local Geology

Volcanic rocks and geological structures in this area are mainly of Quaternary to Recent in age (Lagat, 2003). Eburru geothermal field is mainly composed of a series of trachyte flows (Figure 2.1) down the north-southeast flank (Barongo, 1982) which are in turn overlain by pumice lapilli. Other volcanic series include: rhyolites, obsidian, basalts and syenite. Eburru volcanic shield forms the highest topology in the entire Kenya rift valley standing at an average elevation of about 2800 m.a.s.l (Mwangi, 2012). Eburru fields are composed of two volcanic centres oriented in E-W directions towards Mau escarpment (Eburru Mountain and Badland). To the North of Eburru volcanic shield, lies the basaltic badlands that form an expansive low lying area.

2.3.1.2.1 Pyroclastic

Pyroclastic rocks occur in association with the different eruption cycle in the geologic calendar. It is mainly thickened near or at the crater (>200 m) and then it thin outwards to < 10m (Omenda and Karingithi, 1993).

2.3.1.2.2 Obsidian

This is a fine-grained volcanic rock formed from sudden cooling of magma. It is found mainly on Cedar hill and the immediate adjacent land. The one forming the cone is Recent in age while the surrounding one is of Upper-Pleistocene in age (Lagat, 2003).

2.3.1.2.3 Rhyolites

These are felsic igneous rocks with a composition of more than 70% silica content (Rutley, 1988). They are volcanic equivalent of granite and have aphanitic to porphiritic texture. Other mineral assemblages are sanidine (K- feldspar) and plagioclase. In Eburru geothermal field, the rhyolite is pantellitic as compared to the comendites and rhyolite in Olkaria approximately 30 km south of Eburru geothermal prospect. The Pantellitic-Rhyolite is deficient of aluminum, resulting to enhancement of sodium-potassium elements than is needed for formation of feldspar.

2.3.1.2.4 Trachytes

Trachyte is a felsic volcanic equivalent of syenite. It is formed from partial melting of an igneous rock, releasing alkaline feldspars. It has aphanitic texture and in some cases porphiritic (Rutley, 1988). In the study area, trachyte form the main bedrock as established from drill cores and is of different ages i.e. from Recent to Quaternary.

2.3.1.2.5 Basalts

Basalt is a fine-grained volcanic rock mainly composed of plagioclase and pyroxenes. In the study area, basalt is extensively found in the badland area forming low lying plains. From drilling samples (Omenda and Karingithi, 1993), several layers appear to alternate representing different eruption cycles. Basalts found in the badland area is bluish green, porphiritic and highly vesicular. The groundmass is mainly of iron ore plagioclase and pyroxenes (Thompson and Dodson, 1963).

2.3.1.2.6 Syenite

Syenite is a coarse grained igneous plutonic rock formed from calcium deficient magma resulting from partial melting (Rutley, 1988). It is the plutonic equivalent of trachyte. It is formed in the areas of thickened continental crust.

In the study area, syenite is inferred from the surface by presence of syenitic dykes and fragments of syenite in the pyroclastic material and on many volcanic cones. The rock has dull whitish feldspar that contrast dark colored ferromagnesian minerals. The main accessory minerals are hornblende, diopsidic pyroxene, greenish aegirine, magnetite, analcites and epidote (Thompson and Dodson, 1963). Drilling results indicates that syenite forms the main intrusive body occurring at more than 2600 m.b.g.l (Omenda and Karingithi, 1993).

2.3.1.3 Stratigraphy

The rocks can be divided into three based on the time of their extrusion: - Shield building, pre-shield and intrusive (Omenda and Karingithi, 1993). Stratigraphy of the study area based on drilled well information shows a pyroclastic layer of more than 200 m within the crater section and thins outwardly to about 10 m (Appendix 4). A pantelliritic rhyolite is found below the pyroclastic and extends to about 1400 m.a.s.l. with occasional inclusions of tuffs and Trachyte believed to be the shield building volcanic rocks. A third layer composed of trachyte and minor inclusions of rhyolite, basalts and tuffs form the main pre-shield building rocks. The pre-shield volcanic rocks form the main reservoir rock for the Eburru geothermal system (Omenda and Karingithi, 1993). Presence of dykes of syenitic composition encountered in most of the wells drilled in Eburru with the shallowest occurrence at 800 m.a.s.l. (EW-04) (Appendix 4) reinforce the belief of existence of larger body beneath the eastern volcano (Omenda and Karingithi, 1993). Pyroclastic, comendites and rhyolite form much of the post shield building material Appendix 4.

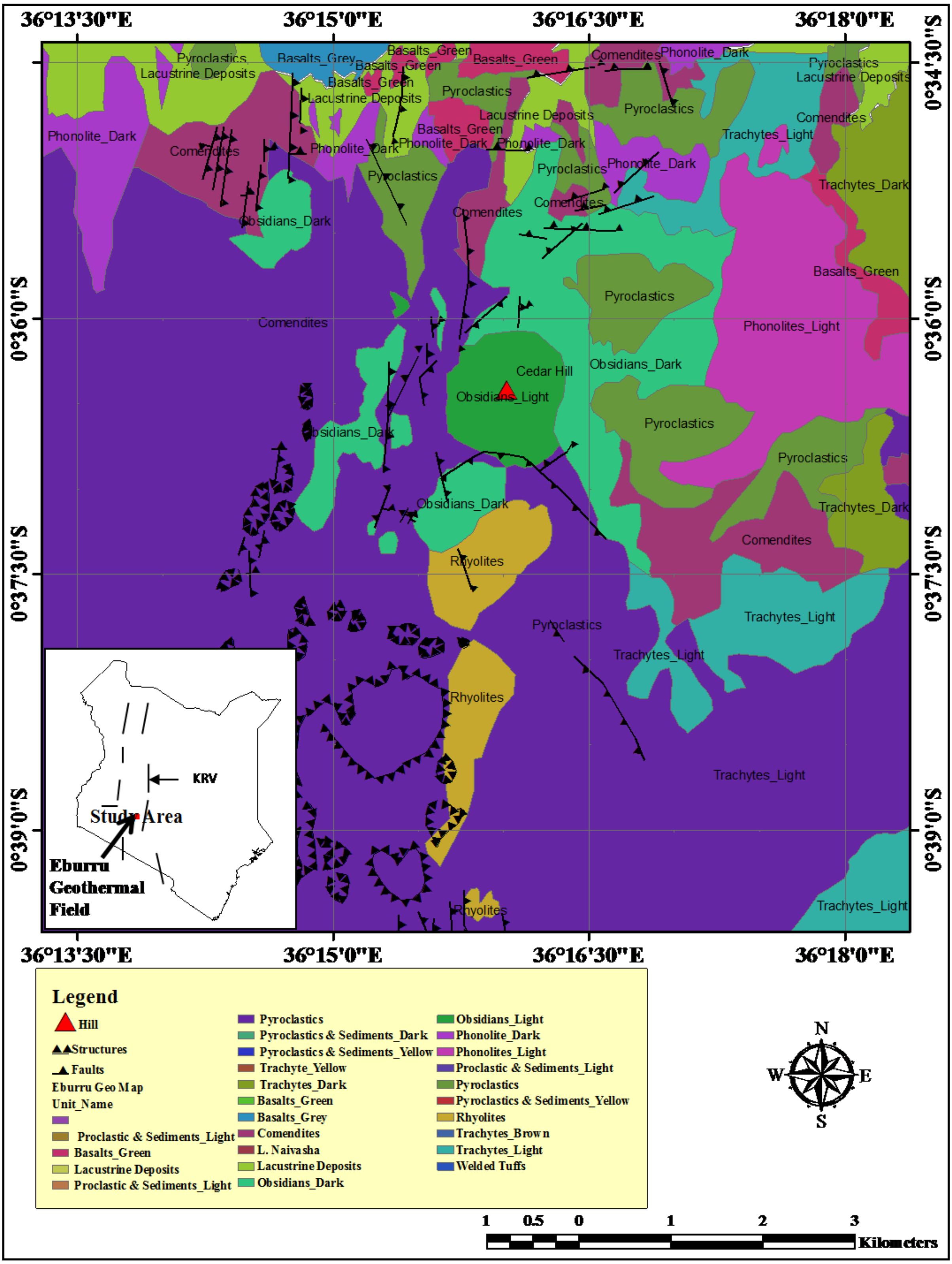

Figure 2.1: Geological Map of Eburru geothermal field (Modified from Thompson (1956))

2.3.1.4 Structures

The main geological features in the study area are: - Caldera, craters, faults, altered grounds and fumaroles. Geological structures in this area are closely associated with faults oriented in N-S direction (Biggs et al., 2009). Presence of fumaroles and hot ground is an indication of an active volcanic region. Presence of hydrothermal alteration is inferred from secondary minerals such as kaolinite, smectite, native sulfur and sinter. These minerals indicate temperatures of $< 180^0$c (Omenda and Karingithi, 1993). From 1500 m.a.s.l., high temperature minerals such epidote, garnet, calcite, biotite, illite, vermiculite and chlorite are found in wells within the ring structure which is an indication of temperatures of more than 220^oC.

2.3.1.5 Hydrothermal Alteration

This involves alteration of primary mineral in rock formations by the action of geothermal fluids from within the geothermal reservoir (Spichak and Zakharova, 2014). This is manifested in the study area as altered grounds and incase of drilled geothermal wells they are associated with alteration minerals of clay (zeolite, illite and smectite), chlorite and epidote.

2.3.2 Hydrogeology

Groundwater occurs within contact zones of different rock formation; fracture zones, OLS and as perched aquifers in clay pockets among others. The flow on the other hand is influenced by structural controls such as fault lines. Most of the water is drained into the ground through highly porous pyroclastic rocks. Several springs in Elementeita derive their water from the Eburru fields (Arusei, 1991). Piezometric map of the larger Nakuru County shows that water flows into the floor of the rift in lateral direction but discharge axially along the rift. There are two main aquifers in the study area i.e. deep and shallow aquifer. Water flowing within Eburru shallow aquifers probably outflow in the Lake Naivasha while water flowing in deep aquifers from Lake Naivasha is deviated by Eburru volcanic ridge ending up into the Elementaita (Yihdego, 2005). In general, groundwater flow is controlled by the EW, NS and NE-SW treading faults with Mau and Nyandarua ranges acting as the main source of recharge via fault lines (Kiende and Kandie, 2015).

2.4 Principles of Electrical Resistivity Method

2.4.1 General

The electrical properties of rocks in the upper crust are dependent upon the lithology, porosity, and degree of pore space saturation, temperature and the salinity of the pore water. Saturated rocks have lower resistivity than unsaturated and dry rocks. High porosity, salinity and presence of clays minerals reduces the resistivity of the rock (Lowrie, 2007). The resistivity of earth materials can be studied by measuring electrical potential distribution produced at the earth's surface by an electric current passed through the earth.

2.4.2 Flow of Current into the Ground from a Single Electrode

Where current is injected into the ground from a point source, it forms equipotential surfaces that are perpendicular to electric field lines as shown in Figure 2.2.

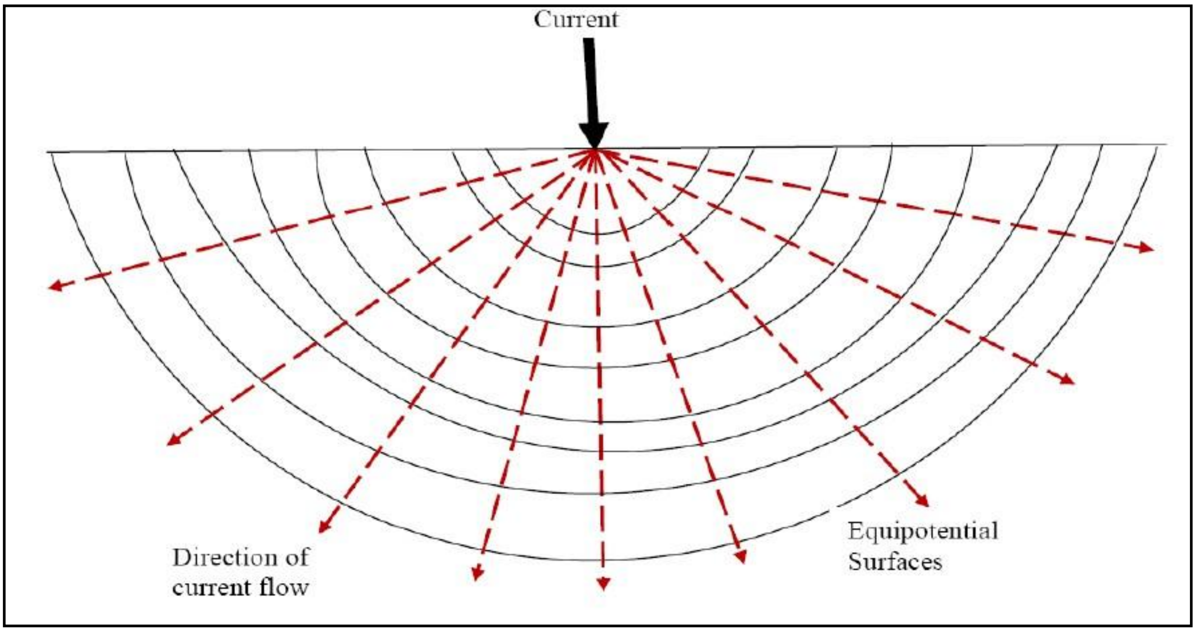

Figure 2.2: Current Flow Distribution from a Point Source and the Resulting Equipotential surfaces (Aizebeokhai, 2010)

2.4.3 Current Flow through a Wire

The resistance (R) of a certain material is directly proportional to its length L, and cross-sectional area A, expressed as: -

$$R = Rs * L/A \quad \text{(in Ohm)} \qquad (2\text{-}1)$$

where Rs is known as the specific resistivity, characteristic of the material and it's independent of its shape or size.

With Ohm's Law;

$$R = dV/I \quad \text{(Ohm)} \quad \ldots\ldots\ldots\ldots\ldots\ldots\ldots\ldots\ldots\ldots \text{(2-2)}$$

where dV is the potential difference across the resistor and I is the electric current through the resistor. The specific resistivity may be determined by: -

$$Rs = (A/L) * (dV/I) \quad \text{(in Ohm m)} \ldots\ldots\ldots\ldots\ldots\ldots\ldots\ldots \text{(2-3)}$$

2.4.4 Potential of a Single Electrode

Electric field distribution due to a point source into a sink (the earth) is always positive and negative from the earth to the electrode source. It decreases as the distance **r**, increases as shown in Figure 2.2. Resistance above the ground is assumed to be infinite hence the ground forms a Dirichlet boundary condition (Herman, 2001). Expressing Ohms law in vector form, Electric field **E**, is directly proportional to current density **j**, where the constant of proportionality is the resistivity **ρ** (Lowrie, 2007) and are related as shown in equation below:

$$E = \rho * j \quad \ldots\ldots\ldots\ldots\ldots\ldots\ldots\ldots\ldots\ldots\ldots\ldots \text{(2-4)}$$

where current density **j**, is equal to current **I**, divided by the cross- sectional area of the conducting medium.

$$J = I/A \ldots\ldots\ldots\ldots\ldots\ldots\ldots\ldots\ldots\ldots\ldots\ldots \text{(2-5)}$$

For a hemispherical surface, the area **A** is equivalent to $\mathbf{4\pi r^2/2\ (2\ \pi r^2)}$. Equation 2-4 above becomes: -

$$E = \rho * I / 2\pi r^2 \ldots\ldots\ldots\ldots\ldots\ldots\ldots\ldots\ldots\ldots \text{(2-6)}$$

From Figure 2.3 (a), **E** can be expressed as the least unit of the potential energy at different distances **r**, from the source. Hence we have: -

$$E = \delta U/dr \ldots\ldots\ldots\ldots\ldots\ldots\ldots\ldots\ldots\ldots\ldots\ldots \text{(2-7)}$$

Relating equation 2-6 and 2-7, we have the following new expression: -

$$\delta U/dr = \rho I / 2\pi r^2 \ldots\ldots\ldots\ldots\ldots\ldots\ldots\ldots\ldots\ldots \text{(2-8)}$$

Differentiating equation 2-8 with respect to **r** will yield the potential due to a single electrode, we have the following: -

$$U = -\rho I / 2\pi r \quad \text{...} (2\text{-}9)$$

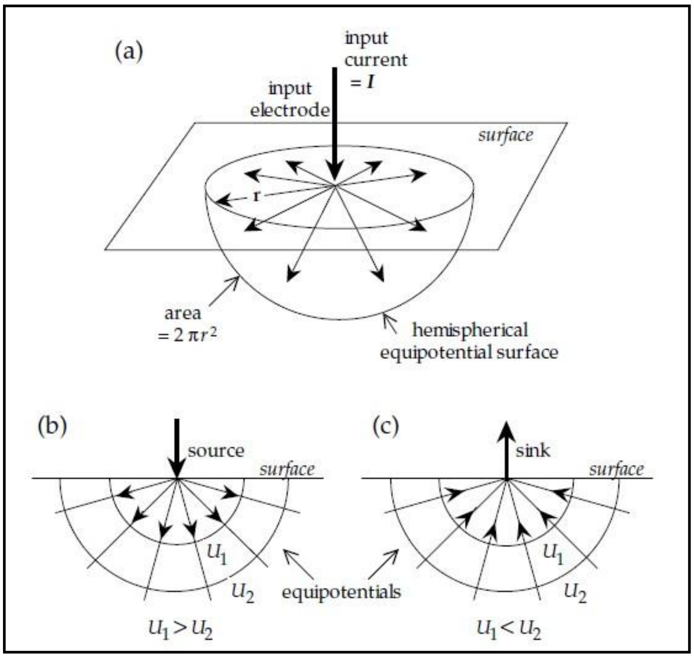

Figure 2.3: Electric Field Lines and Equipotential Surfaces around a Single Electrode at the Surface of a Uniform Half-space: (b) Source and (c) Sink: Modified from Lowrie (2007).

2.4.5 General Four Electrode Approach

In this scenario, we consider potential at C due to source A and sink B (Lowrie, 2007).: -

Due to A $$U_{AC} = \frac{\rho I}{2\pi r(AC)} \quad \text{.................} (2\text{-}10)$$

Due to B $$U_{CB} = -\frac{\rho I}{2\pi r(CB)} \quad \text{.................} (2\text{-}11)$$

*Noting that the sink at **B** has negative potential energy as indicated in equation 2-11

We then determine the combined potential energy $\mathbf{U_C}$ due to **A** and **B** at **C** to have the following: -

$$U_{C\ at\ C} = \frac{\rho I}{2\pi r(AC)} - \frac{\rho I}{2\pi r(CB)} = \frac{\rho I}{2\pi}\left(\frac{1}{r(AC)} - \frac{1}{r(AC)}\right) \quad \text{..........} (2\text{-}12)$$

Repeating the same procedure now at **D** due to **A** and **B**, we have the following: -

Due to A $$U_{AD} = \frac{\rho I}{2\pi r(AD)} \quad \text{.................} (2\text{-}13)$$

Due to B $$U_{DB}=-\frac{\rho I}{2\pi r(DB)} \quad \ldots\ldots (2\text{-}14)$$

$$U_{C\ at\ D}=\frac{\rho I}{2\pi r(AD)}-\frac{\rho I}{2\pi r(DB)}=\frac{\rho I}{2\pi}\left(\frac{1}{r(AD)}-\frac{1}{r(DB)}\right) \quad \ldots\ldots (2\text{-}15)$$

The potential difference **V**, measured between **C** and **D** is given by the following equation: -

$$V=\frac{\rho I}{2\pi}\left[\left(\frac{1}{r(AC)}-\frac{1}{r(CB)}\right)-\left(\frac{1}{r(AD)}-\frac{1}{r(DB)}\right)\right] \quad \ldots\ldots (2\text{-}16)$$

Resistivity ρ is therefore equal to: -

$$\rho=\frac{2\pi V}{I}\left[\left(\frac{1}{r(AC)}-\frac{1}{r(CB)}\right)-\left(\frac{1}{r(AD)}-\frac{1}{r(DB)}\right)\right]^{-1} \quad \ldots\ldots (2\text{-}17)$$

Introducing a constant G: -

$$G=\left[\left(\frac{1}{r(AC)}-\frac{1}{r(CB)}\right)-\left(\frac{1}{r(AD)}-\frac{1}{r(DB)}\right)\right]^{-1} \quad \ldots\ldots (2\text{-}18)$$

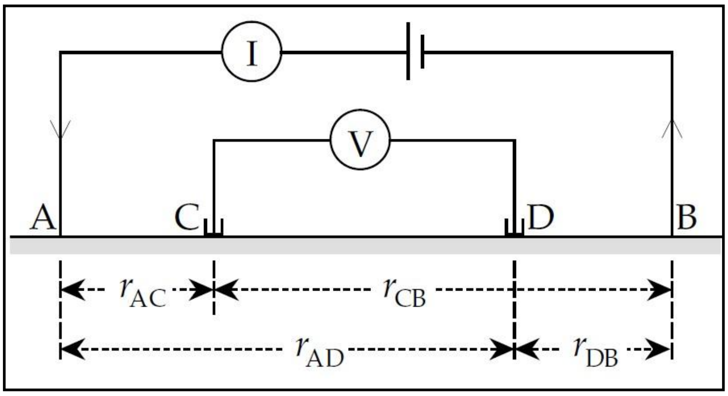

Figure 2.4: Electrode Configuration for Resistivity Measurement Consisting of two Pairs of Electrode (Current A, B and Potential Electrodes C, D)*(Lowrie, 2007*).

2.4.6 Apparent Resistivity

Due to in-homogeneity of the earth materials, we determine the apparent resistivity **ρ** expressed as follows (Lowrie, 2007): -

$$\rho=\frac{2\pi V}{I}G=\frac{V}{I}K \quad \ldots\ldots (2\text{-}19)$$

where; K is the Geometrical factor.

2.4.7 True Resistivity

True resistivity is obtained from inversion of apparent resistivity data. It represents the approximate resistivity for an idealized homogeneous layered earth.

2.4.8 Vertical Electrical Sounding (VES)

Vertical electrical sounding method is a DC method of geophysical survey. DC methods have their origin in 1920's due to schlumberger brothers and quantitative interpretation methods were used (Koefoed and Mallick, 1979). Vertical electrical sounding method is easy to deploy and the theory involved is not complicated. Thomas (2002) suggested that vertical electrical resistivity method gave higher resolution in terms of resistivity for the first few metres below the surface, as opposed to Transient Electromagnetic Methods (TEM). The Schlumberger array provides a high signal-to noise ratio, good resolution of horizontal layers, and good depth sensitivity (Ward, 1990).

When carrying out a resistivity sounding, current is led into the ground by means of two electrodes. With two other electrodes, situated near the center of the array, the potential field generated by the current is measured.

From the observations of the current strength and the potential difference, and taking into account the electrode separations, the ground resistivity can be determined.

During a resistivity sounding, the separation between the electrodes is step-wise increased (in what is known as a Schlumberger Array), thus causing the current to penetrate greater depths. When plotting the observed resistivity values against depth on double logarithmic paper, a resistivity curve is formed, which depicts the variation of resistivity with depth. This curve can be interpreted with the aid of a computer program, and the actual resistivity layering of the subsoil is obtained. The depths and resistivity values provide the geophysicists with information on the geological layering.

2.4.9 Modeling

Modeling involves representation of a portion of earth using numerical representations based on geophysical or geological information. To determine parameters constituting the model, inversion process is carried out using data from a synthetic data and measured data. Of particular interests in this research project is resistivity data and geological logs that were used to construct a 2D and 3D geo-electric structure. Geological information facilitates constraining the inversion process. Borehole logs for instance, provide a priori information when constraining depth of layers.

2.4.10 Apparent Resistivity Curve Types

There are four types of apparent resistivity curves (Lowrie, 2007) based on their orientation or the slope as indicated in Figure 2.5. They include: -

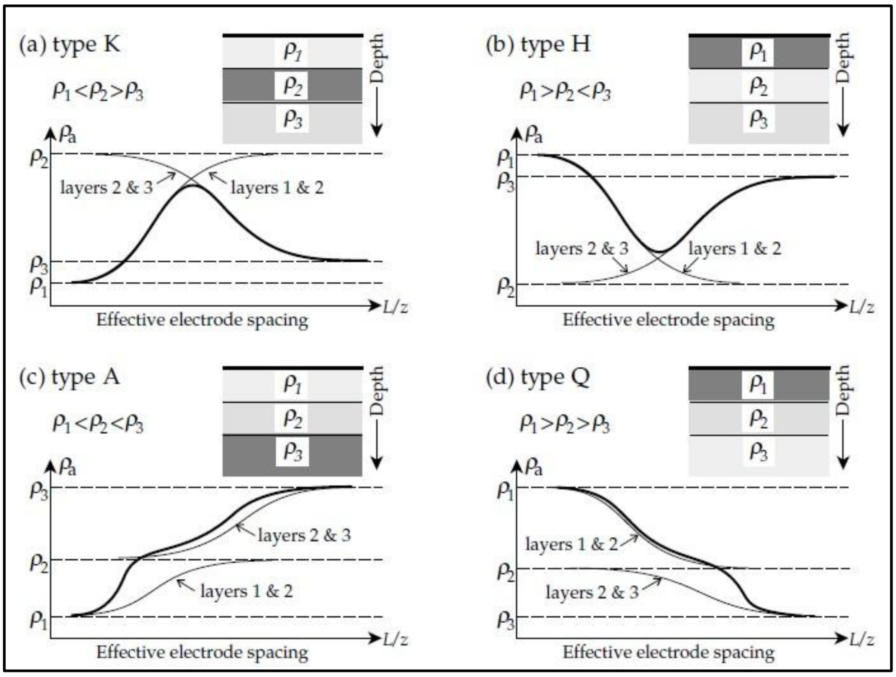

Figure 2.5: Common Apparent Resistivity Curves for a Layered Structure Consisting of Three Horizontal Layers (Lowrie, 2007)

K-Curve type: - The type displays a rise to maximum and then drops indicating a high resistivity layer embedded in between two-low resistivity.

H-Curve type: - This curve type is a complete opposite to K-type curve where it drops and then rise indicating that the middle layer is a low resistivity layer as compared to the bottom and top layer in a three layer model.

A-Curve type: - In this case, the resistivity rises with increasing depth. The rising curve exhibits slight slow down as a result of several layers encountered with depth. Their resistivity increases with depth.

Q- Curve type: - This type is a complete opposite of A-type since the curve fall sharply with slight gradient change indicating successive changes in layers with increasing depth.

2.4.11 Inversion

Inversion is the process of converting observed measurements into a material physical property. Inversion involves development of initial model (Lowrie, 2007). Inversion is the process of finding connections between data and model space (Roy, 2008) . Figure 2.6 shows a sample flow chart for an inversion process.

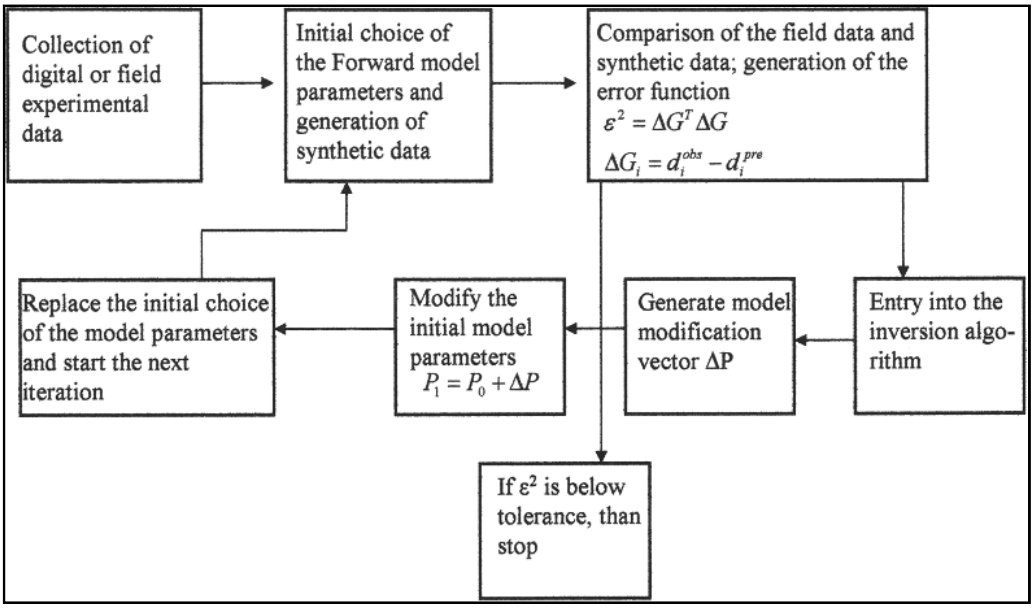

Figure 2.6: A Sample Flow Chart for an Inverse Problem (Roy, 2008)

Smoothness constrained least-squares method is one of the common routine used in most inversion processes. The method is based on equation 4-20 (Loke, 2013).

$$(\mathbf{J^TJ} + \lambda \mathbf{F})\, \Delta \mathbf{q_k} = \mathbf{J^Tg} - \lambda \mathbf{Fq_k}, \quad \text{……………………………………………(2-20)}$$

where,

	$\mathbf{F}$	=	$\alpha_x \mathbf{C_x}^T\mathbf{C_x} + \alpha \mathbf{C_y}^T\mathbf{C_y} + \alpha \mathbf{C_z}^T\mathbf{C_z}$
	$\mathbf{C_x}$, $\mathbf{C_y}$	=	Horizontal roughness filter
	$\mathbf{C_z}$	=	vertical roughness filters
	$\mathbf{J}$	=	Jacobian matrix of partial derivatives
	$\mathbf{J^T}$	=	Transpose of **J**
	λ	=	Damping factor
	$\mathbf{q}$	=	Model perturbation vector
	$\mathbf{g}$	=	Data misfit vector

To solve the system of simultaneous equation involved partial derivatives in **J,** Gauss-Newton method is used. The inversion process involves subdivision of the subsurface into smaller blocks and through the optimization procedure, after a number of iterations, the inversion process attempts to reduce the difference between calculated and observed resistivity for each block. A consistent R.M.S after a 5th to 6th iteration will yield an approximate model of the true subsurface. The partial differential equation in Jacobian matrix is solved using either finite difference or finite element method.

2.4.12 Factors determining Conductivity of Earth Materials

2.4.12.1 Porosity

Porosity is a function of amount of voids in the earth material. It is expressed a as percentage of the total volume of a material. Pore spaces provide storage or conduits for ground water flow and as such, the more the pore spaces the more the water will be allowed through or held at any one given moment hence allowing electricity flow. Sediments have high porosity hence hold more water and in most cases well connected. Crystalline rocks have low porosity hence low water content and as a result, current flow in the rock is inhibited leading to high resistivity.

Groundwater contains dissolved minerals from the wall rock depending on duration of contact (Lowrie, 2007). When injected into the earth, current is easily transmitted through such saturated medium hence reduced electrical resistivity.

At high temperatures (> 300^0 c at about 500 bars), the resistivity of earth materials increases due to loss of porosity (Hersir and Árnason, 2009 and Ussher et al., 2000).

2.4.12.2 Water Content

Different rock types have different lithological characteristics i.e. mineral characteristics, rate of weathering among others. Wet or moist material have low resistivity factor due to uninhibited current flow. Dry materials on the other hand resist current flow leading to high resistivity.

2.4.12.3 Temperature

Conductivity of rock material is directly proportional to amount of water contained in it and directly proportional to dissolved ions (Lowrie, 2007). Temperature determines the dissolving capacity of fluids and as such, rock conductivity increases with the amount of dissolved ions.

CHAPTER 3.0: MATERIALS AND METHODS

3.1 Materials

3.1.1 Softwares

After acquisition of secondary data, relevant softwares were used to process, analyze and interpret VES data set. They include: -

Formula Translation (FORTRAN): - This is an open source computer programming language by Silverfrost (FTN95 Plato.exe). It was used to convert raw VES data for use in 1D Earth Imager. It is easy to use and easily adaptable.

Quantum Geographical Information System (Q-GIS-Version 2.10.1): - The open source software was used to prepare relevant maps (Geological map, rainfall map, structural map, topographical map and piezometric map).

Earth Imager: - This commercial Software was used to generate true resistivity values after modeling and inversion.

Geosoft (Oasis Montaj- Version 6.4.2 HJ): - This is commercial software and was used to generate 2D maps. It was preferred since it does not incorporate data gaps when contouring.

Surfer 9: - The software was obtained from the department of Geology and used to prepare piezometric surface maps.

3.1.2 Hardware

To compile data from different sources, specific hardwares were used: - Laptop, photocopying machines, scanning machine and printing machine among others.

3.1.3 Data

Data utilized in this research was from different sources i.e. open source databases from the internet, previous studies, companies/ organizations among others.

3.1.3.1 Open Source Databases

The following databases provided specific geographical information of the study area: -

i. International Livestock Research Institute (ILRI) is an open source archive for GIS data. This includes among others; Geology of Kenya, administrative boundaries, rainfall data, vegetation covers. The site was accessed from the following website: -

   http://192.156.137.110/gis/search.asp

ii. World Resource Institute provides open source archive for GIS data for specific attributes about Kenya. They include among others: - Elevation and land use data.

http://www.wri.org/resources/data-sets/kenya-gis-data

3.1.3.2 Data from Company and Organization

Borehole data was provided by WRMA and was used to construct piezometric maps. Geological well log data was provided by KENGEN and was used during inversion process.

3.1.3.3 Data obtained from other Sources

Data obtained from other sources include: - geological map obtained from previous geological reports in Naivasha area. The main data type utilized in this study was the vertical electrical sounding data which was obtained from previous studies by Barongo, 1982.

3.2 Methods

To achieve the objectives, a comprehensive desktop study, data collection, analysis and interpretation were carried out.

3.2.1 Desktop Studies

Extensive desktop study was carried out which included among others: Study of base maps reports and papers from literature.

3.2.2 Data Acquisition

VES data used in this study were obtained from previous work done by Barongo (1982) in the same study area. A total of 149 VES data along specific survey lines A to U running from West to East (Alphabetically: - A-U) as shown in Figure 3.1 were used. Important thing to note is that traverses ***I-I′, II-II′, III-III′*** and ***IV-IV′*** coincides with profiles 1, 3, 4 and 8 in Omiti (2013) where: - Traverse ***I-I′*** coincides with profile 1 in Omiti (2013), traverse ***II-II′*** with profile 8, traverse ***III-III′*** with profile 4 and traverse ***IV-IV′*** with profile 3 in Omiti (2013).

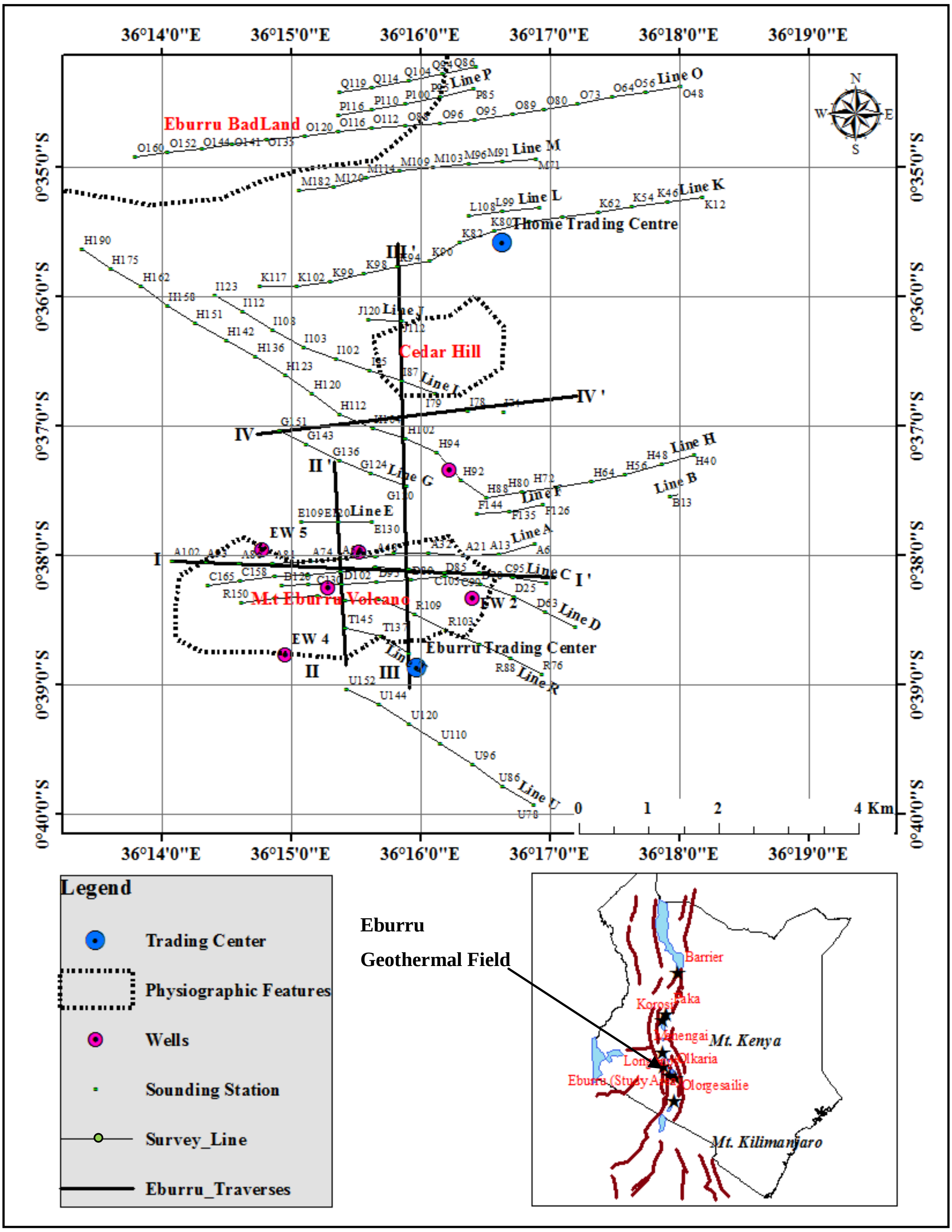

Figure 3.1: Location of Eburru Survey Lines, Traverses, Wells and Sounding Stations

3.2.2.1 Data Preparation

The secondary VES data was initially in hard copy and had to be typed. To upload VES data into Earth Imager, FORTRAN codes provided in Appendix 1 were used to arrange raw VES data into a format that could be read by 1D Earthimager. After loading data into 1D Earthimager, data smoothing was done to correct for outliers.

3.2.3 Data Processing and Analysis

Data processing and analysis was done in four stages as explained in the following subsections.

3.2.3.1 Inversion

After cleaning data, specific settings were set (Number of iterations and Minimum standard deviation). To create a 1D model, electrical resistivity, number of layers and depth of layer were first guessed and set in what is known as forward model. Inversion process was then carried out using the guessed parameters and the software calculated consequent parameter values. The inversion process was constrained using borehole logs as priori information. The final product in this stage was 1D models showing layer thickness, electrical resistivity and depth to layer (Figure 3.2).

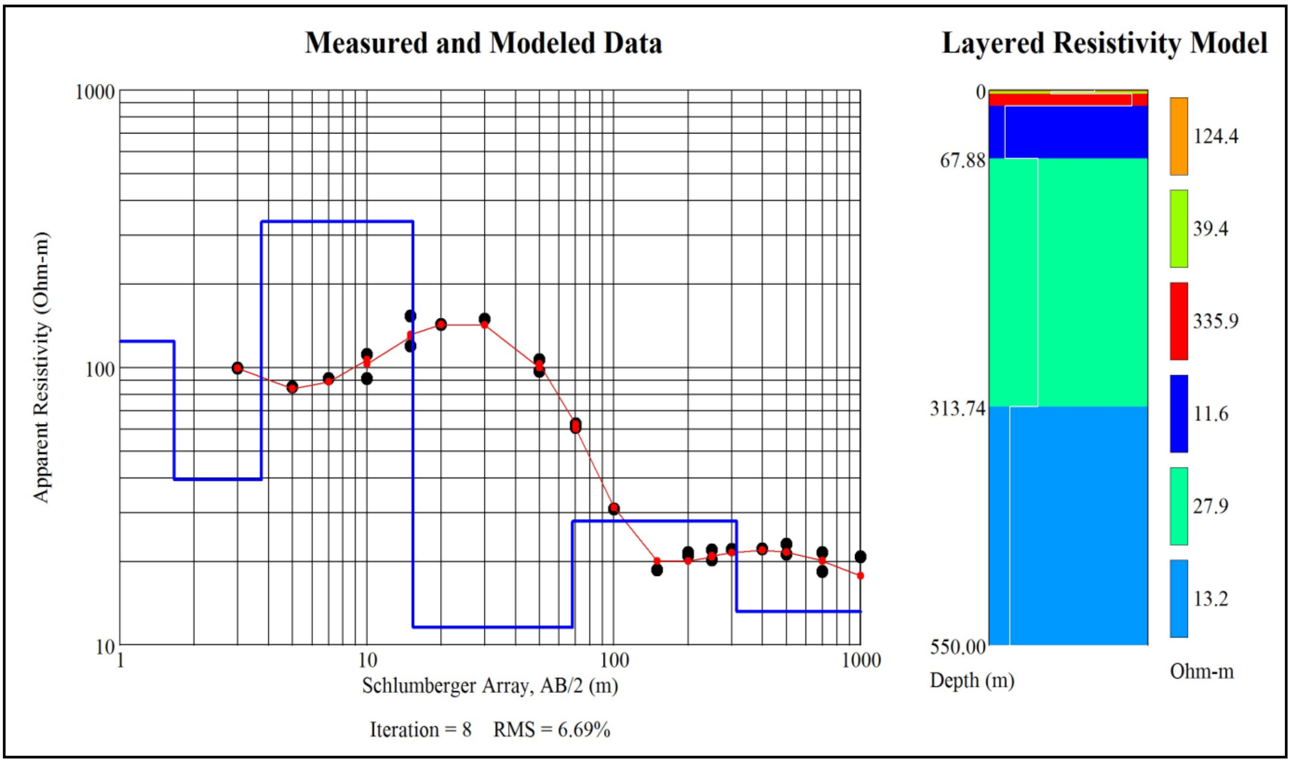

Figure 3.2: A Sample of Inverted VES Data (A13) along Line A.

3.2.3.2 2D Geo-section Section

In this stage, 1D model data was formatted for use in Oasis montaj in order to produce 2D view. Among the parameters set were: - (Grid cell sizes of 2.25cm by 2.25cm and approximation method; Akima method was used since it gave the best resolution and stable to outliers). To increase the weight of specific data points, the bi-directional line gridding method was used since it give more weight to points along vertical lines from the surface to the deepest level penetrated. The resulting 2D images were prepared by inserting a base map as illustrated in Figure 3.3.

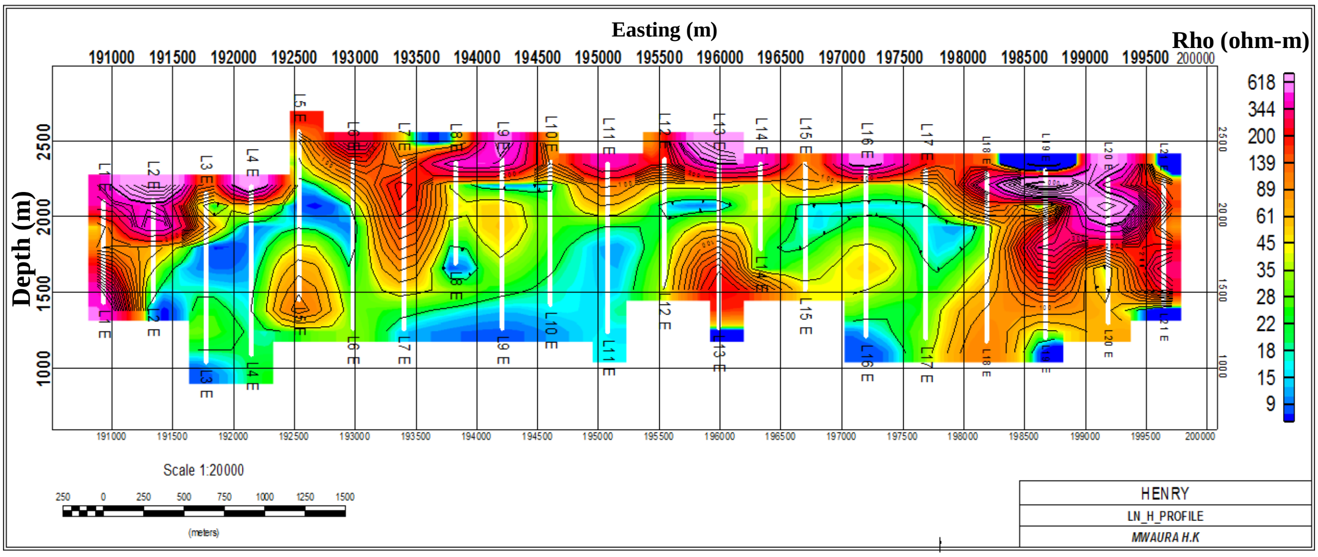

Figure 3.3: A Sample of 2D geo-section along Survey Line H

3.2.3.3 Iso-surface Maps

Iso-surface maps were plotted from the true resistivity values on a uniform elevation of 2000 m.a.s.l where the interface between overburden and the aquiferous formation intersects. The easting and northing values for sounding points within each block were used for horizontal positioning.

3.2.3.4 3D Visualization

3D geo-electric maps were also constructed using 2D geo-electric sections by juxtaposing adjacent lines for a given block through coinciding the easting's values.

3.2.4   Piezometric Surface Map

Piezometric map for the larger Nakuru County was constructed by subtracting the static water level from the surface level to get the elevation of the water rest level. The adjusted water levels in reference to the sea level are plotted on horizontal surface resulting to piezometric surface map. A higher piezometric level value is an indication of higher hydraulic head and vice versa. Higher hydraulic head is an indication of recharge area; while low hydraulic head indicates discharge areas as in illustrated in Figure 4.19.

CHAPTER 4.0: RESULTS AND DISCUSSIONS

4.1 Introduction

A total of 149 VES data were analyzed and interpreted based on the selected blocks within the study area (Figure 4.1).

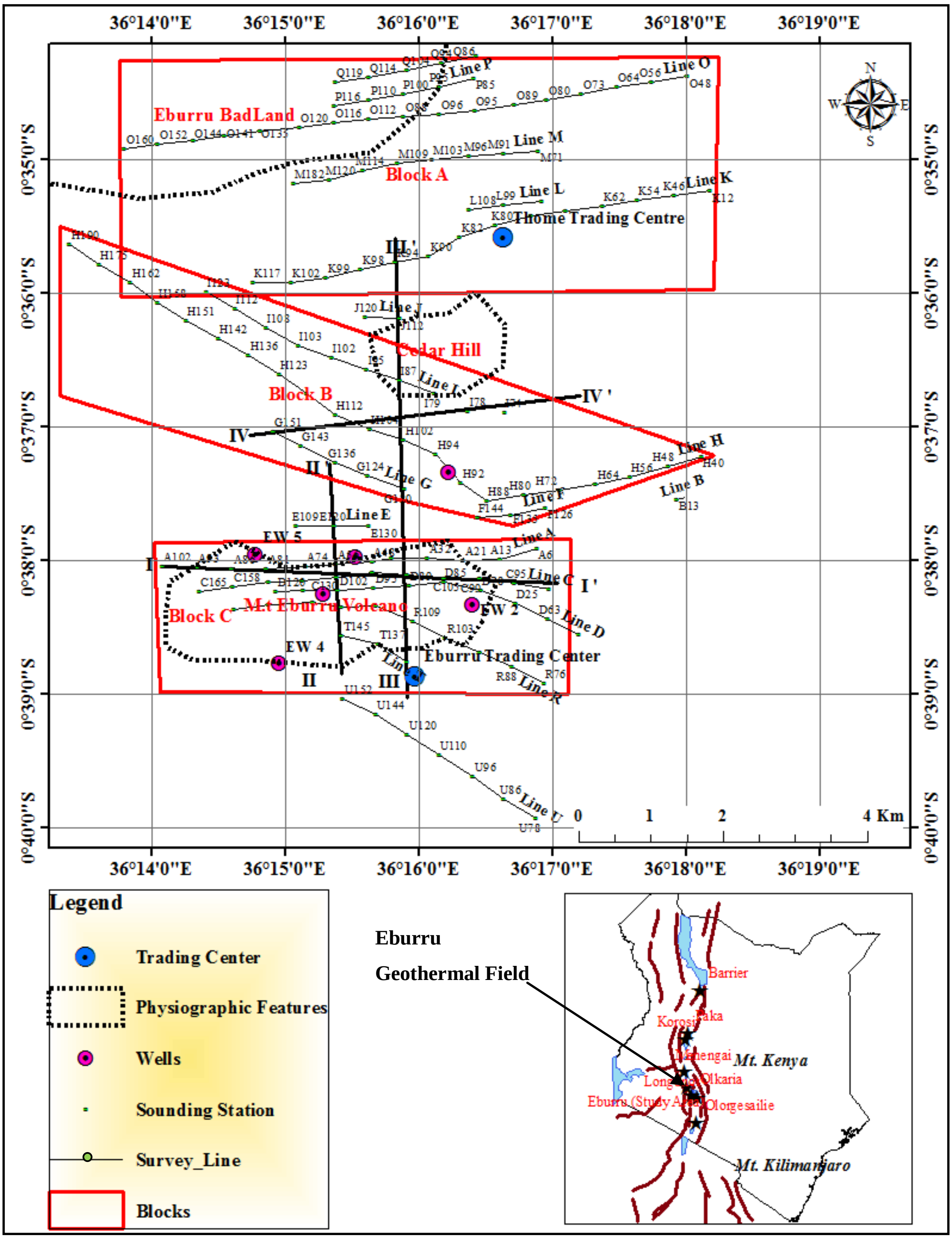

Figure 4.1: Location of Blocks and Traverses utilized in this Study

4.2 Results

4.2.1 Mode of Data Presentation

As guided by the stated objectives in chapter one, results of data analysis are presented in both 2D geo-sections, iso-resistivity maps and 3D images for clear understanding of the subsurface shallow geo-electric structure. Iso-resistivity maps were set at about 2000 m.a.s.l in order to capture structural changes within the transitional boundary between the first and middle geo-electric layers. 2D images were constructed using Oasis montaj software. The study area was divided into several blocks A, B and C (Figure 4.1). 3D images were constructed by juxtaposing 2D geo-electric sections.

4.2.2 2D Geo-electric Sections for Traverses within the Study Area

A 2D geo-electric section provides an image of a specific line observed from the surface to the bottom layer. A total of 4 traverses were utilized to construct 2D geo-sections through block B and C (Figure 4.1) in order to compare with findings from other researchers such as Omiti (2013) where he used TEM and MT to map deep resistivity structure beneath Eburru geothermal prospect. To compare results of the geological well log for the six wells, 2D geo-electric sections for line R, D, H and A (Figure 4.1) were used.

4.2.2.1 Geo-electric Section along Traverse I-I′

A total of 10 VES data points were used to construct a 2D image along traverse ***I-I′*** as illustrated in Figure 4.2. The geo-electric section displays H-type curve where two highly resistive (> 200 Ωm) layers sandwich a relatively less resistive layer. A highly resistant (> 200 Ωm) convex structure is observed along the section, sandwiched between two fault lines. The low electrical resistivity (15 Ωm - 100 Ωm) zone located about 2250 m.a.s.l. is an indication of aquiferous geo-electric layer. Pockets of low electrical resistivity (< 10 Ωm) are observed especially near the inferred fault lines. It is observed that the resistivity decreases steadily along the fracture zone. KENGEN drilled a well (EW-06) less than 50m from traverse ***I-I′*** at the location of L1E (Figure 4.2) and it gave the highest discharge equivalent to 2.9MW.

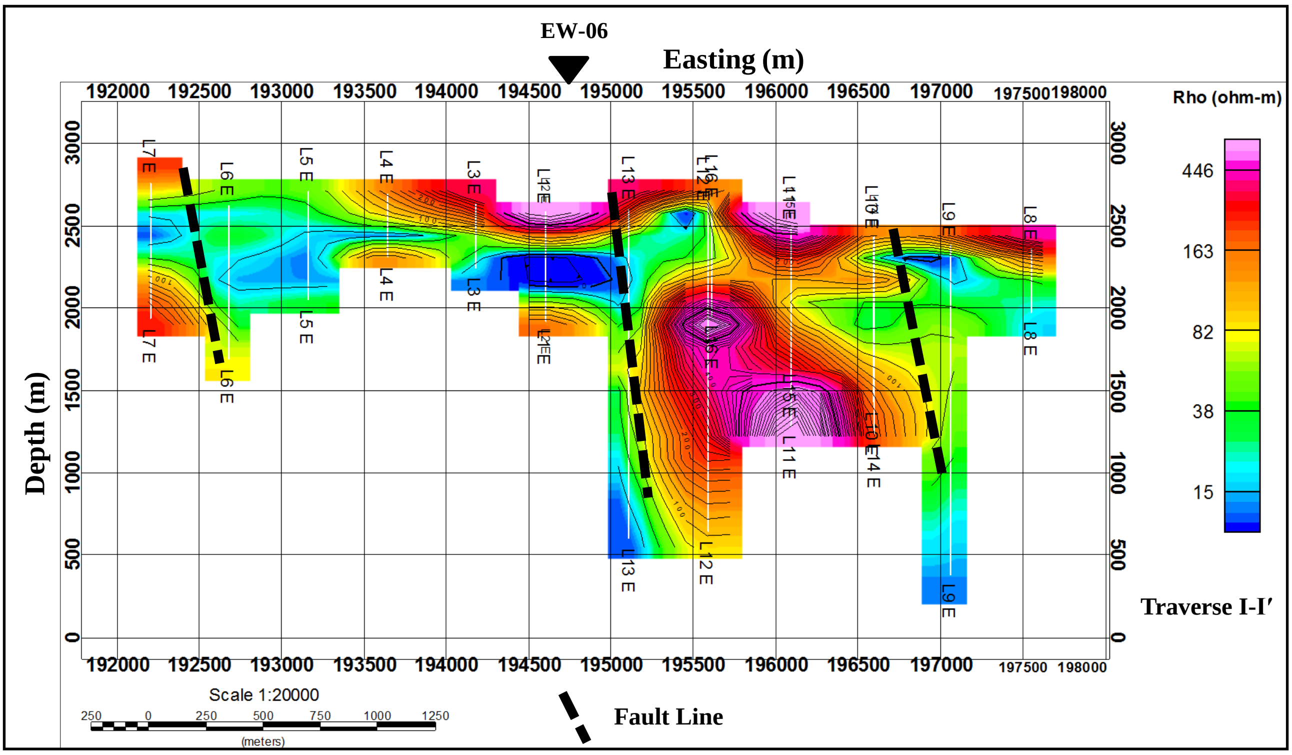

Figure 4.2: 2D Geo-electric Section along Traverse *I-I′* Running in E-W direction

4.2.2.2 Geo-electric Section along Traverse II-II′

To construct a geo-section along traverse ***II-II′*** running in N-S direction, 7 VES data points were used as illustrated in Figure 4.3. Like traverse ***I-I′*** above, traverse 2 also display H-curve type where low resistant zone is bounded by two highly resistive (> 200 Ωm) layers displaying a three layered earth. A highly resistive (> 200 Ωm) convex geo-electric structure (reddish in color) is observed terminating at about 2250 m.a.s.l and above it is a low electrical resistivity (< 10 Ωm) pocket indicating presence of hydrothermal alteration minerals such as clay. Unlike traverse ***I-I′***, traverse ***II-II′*** shows relative homogeneity within the geo-electric layers where electrical resistivity values are < 100 Ωm.

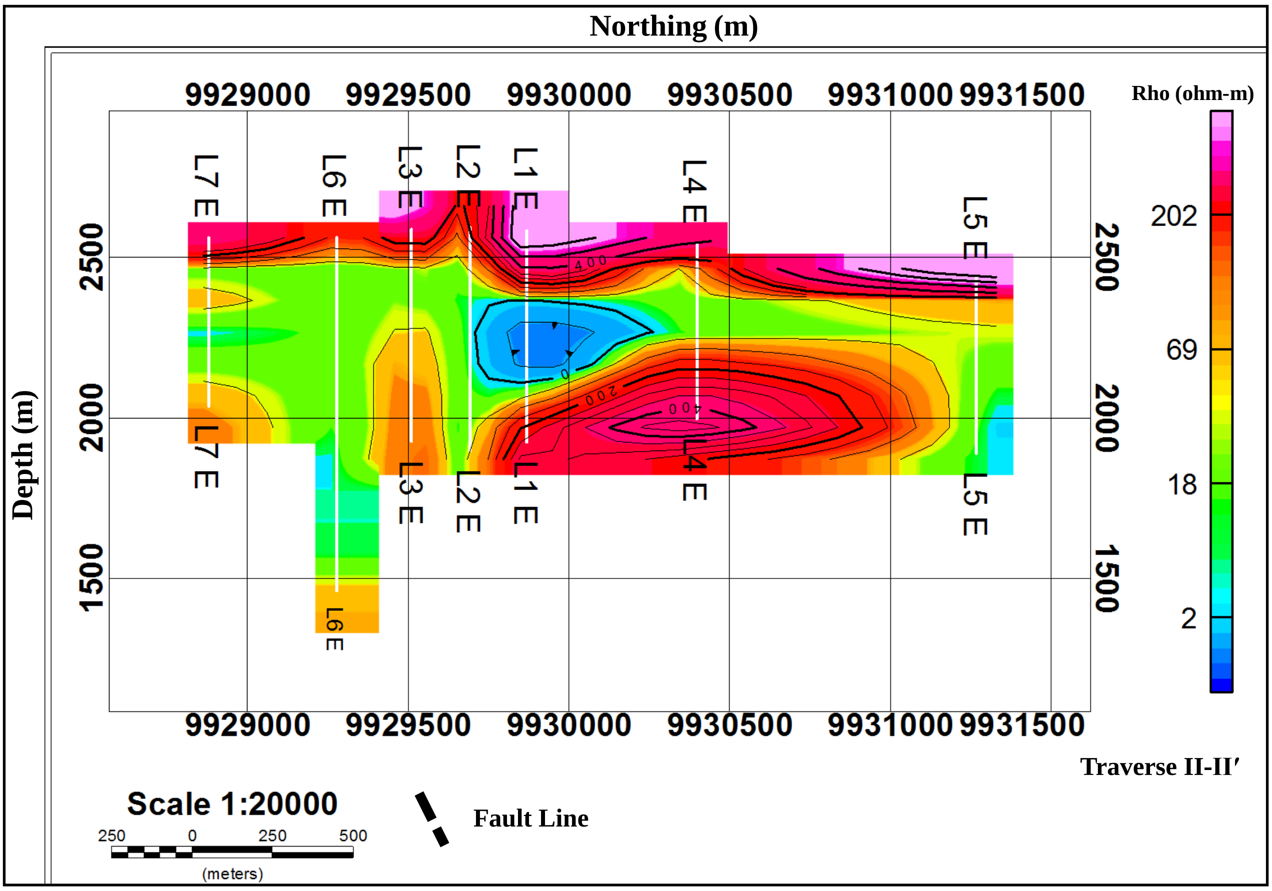

Figure 4.3: 2D Geo-electric Section along Traverse *II-II′* Running in N-S direction

4.2.2.3 Geo-electric Section along Traverse III-III′

2D geo-electric section for traverse ***III-III′*** was constructed from 10 VES data points plotted in N-S direction as illustrated in Figure 4.4. Like traverse ***I-I′*** and ***II-II′***, traverse ***III-III′*** also display H-type curve where the low resistant zone extends from about 1500 m.a.s.l to about 2500 m.a.s.l. Geo-electric layers shows electrical resistivity homogeneity within themselves. A convex structure with resistant (> 379 Ωm) occur in the southern side of the traverse terminating at about 2250 m.a.s.l. A low resistivity pocket caps the high resistivity body at slightly above 2250 m.a.s.l.

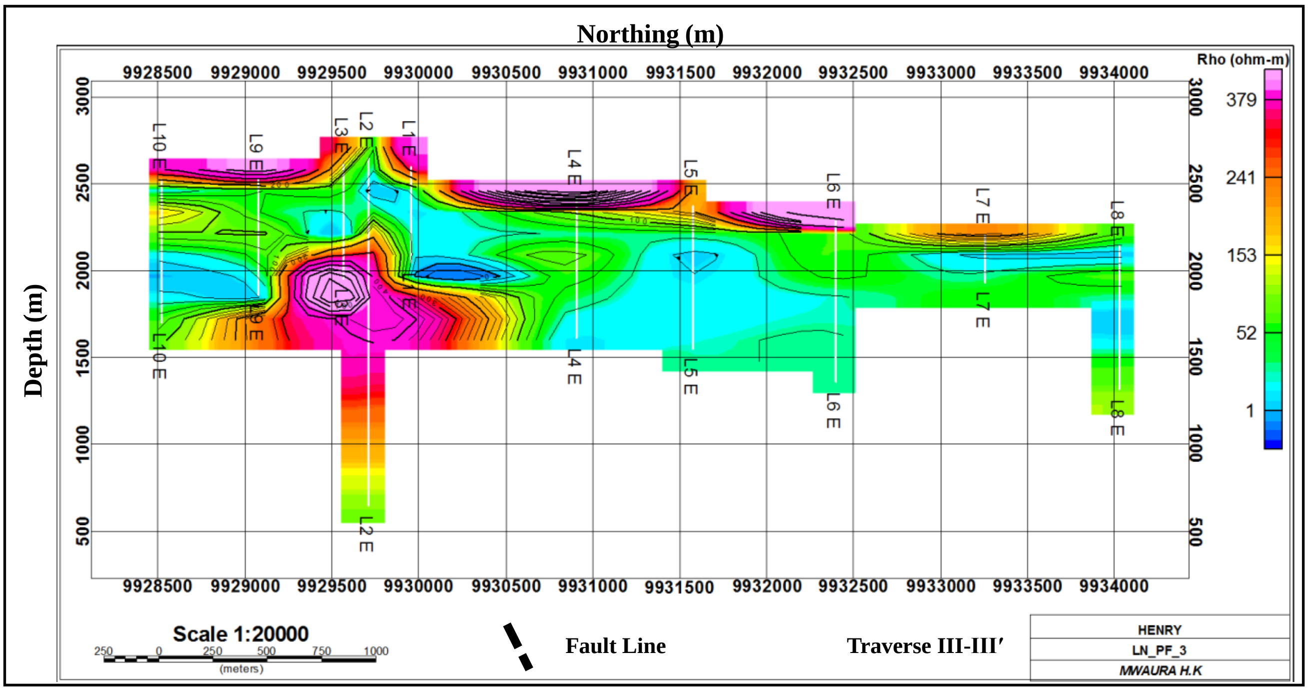

Figure 4.4: 2D Geo-electric Section along Traverse *III-III′* (N-S)

4.2.2.4 Geo-electric Section along Traverse IV-IV′

2D geo-electric section for traverse ***IV-IV′*** was plotted using 7 VES data points oriented in E-W direction as illustrated in Figure 4.5. A fault line is inferred in the western and eastern side and appears to be linked with localized low resistant region (< 15 Ωm). The two faults observed create step faults. At the mid-section of the 2D geo-section (blue), is a low resistant (< 15 Ωm) near vertical geo-electric structure rising from below 1000 m.a.s.l observed at L4E (Figure 4.5) and it extends for more than 500m.

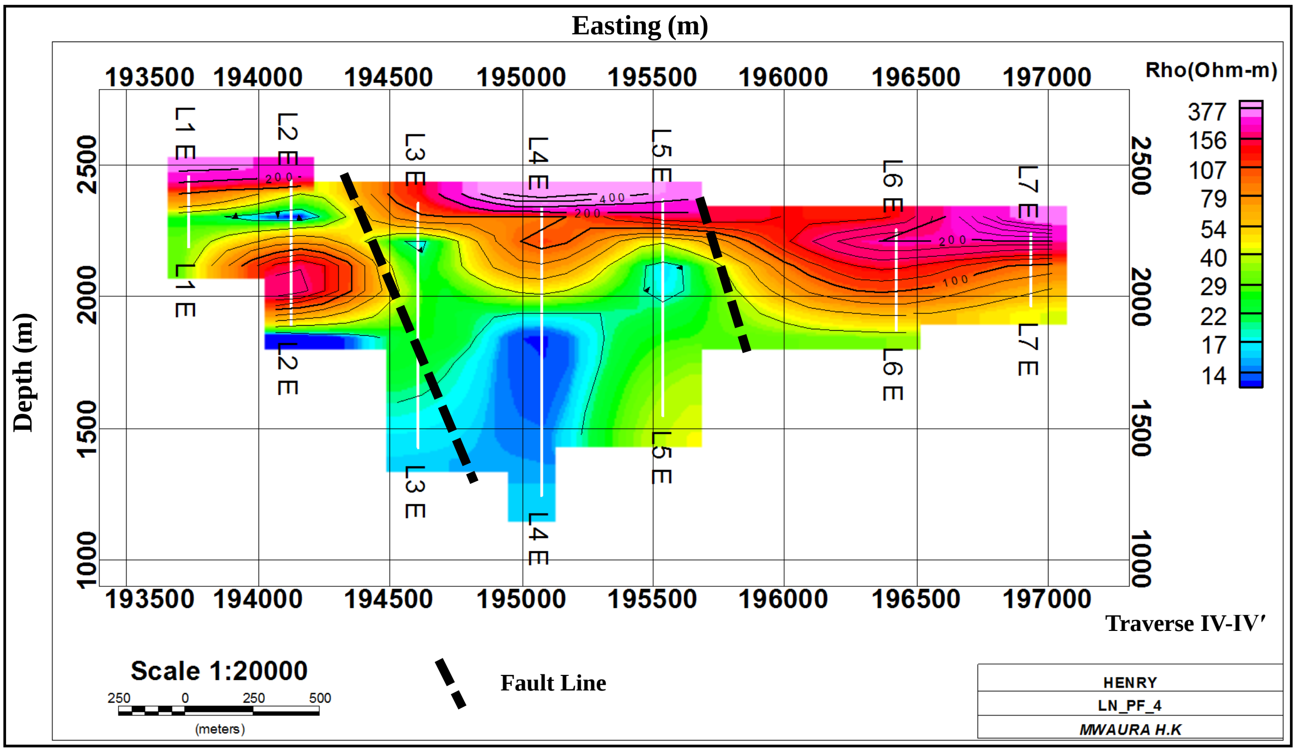

Figure 4.5: 2D Geo-electric Section along Traverse *IV-IV′* in Block B (E-W)

4.2.3 Geo-electric Structure Beneath Block A

Geo-electric structure beneath block A is presented as both iso-resistivity map and 3D image. It is located in the northern side of the study area (Figure 4.1) where Eburru badland is located.

4.2.3.1 Iso-resistivity Maps in Block A taken at 2000 m.a.s.l

An iso-resistivity map for block A taken at about 2000 m.a.s.l indicates zones of low resistivity (< 150 Ωm) oriented approximately N-S direction (Figure 4.6). A high resistivity structure (> 200 Ωm) oriented in NW-SE direction appear to influence groundwater flow at about 2000 m.a.s.l. The iso resistivity map for block A is consistent with the geo-electric structural pattern observed in 3D image (Figure 4.7) where a high resistivity (> 200 Ωm) vertical geo-electric structures extending for more than a kilometer.

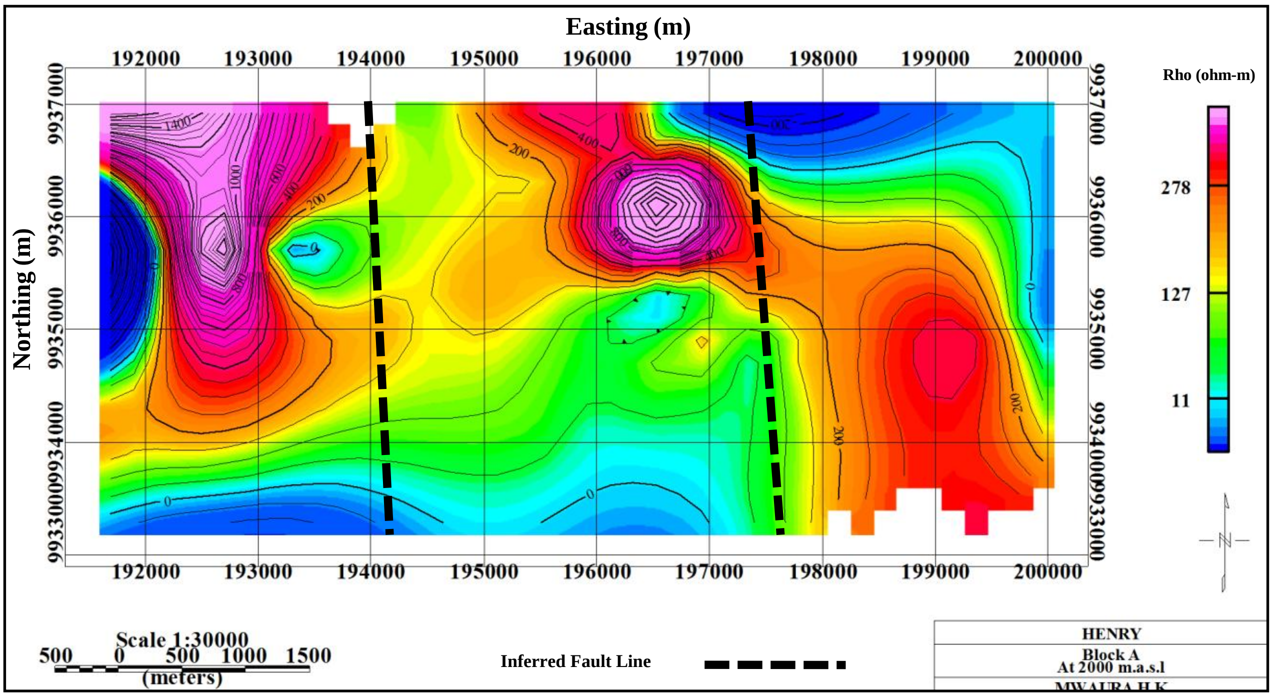

Figure 4.6: Iso-resistivity Map in Block A taken at about 2000 m.a.s.l

4.2.3.2 3D Visualization of Geo-electric Structure in Block A- Lines O-M-K

Three 2D geo-electric sections from lines O, M and K (Figure 3.1) were juxtaposed to create a 3D visualization (Figure 4.7) in block A (Figure 4.1). The 3D visualization indicates that linear geo-electric structures are oriented approximately in N-S direction. There is high variation in resistivity from the surface to about 2250 m.a.s.l indicating a complex geology, where both low and high resistivity zones occur intercalated with each other. One conspicuous feature visible on the 3D visualization is pockets of convex structure of very high (> 700 Ωm, shaded red-purple) and very low (< 10 Ω m) resistivity (shaded blue). A low resistivity zone (< 70 Ωm) occurring at about 1800 m.a.s.l., is the most dominant horizontal geo-electric feature noticeable in the 3D image. It is sandwiched between relatively high resistivity geo-electric layers creating a three layered earth. Another notable feature is the vertical geo-electric structures marked by vertical bands of electrical resistivity < 100 Ωm, where they intersect horizontal geo-electric layers and are likely indicators of a fault line or fracture zone.

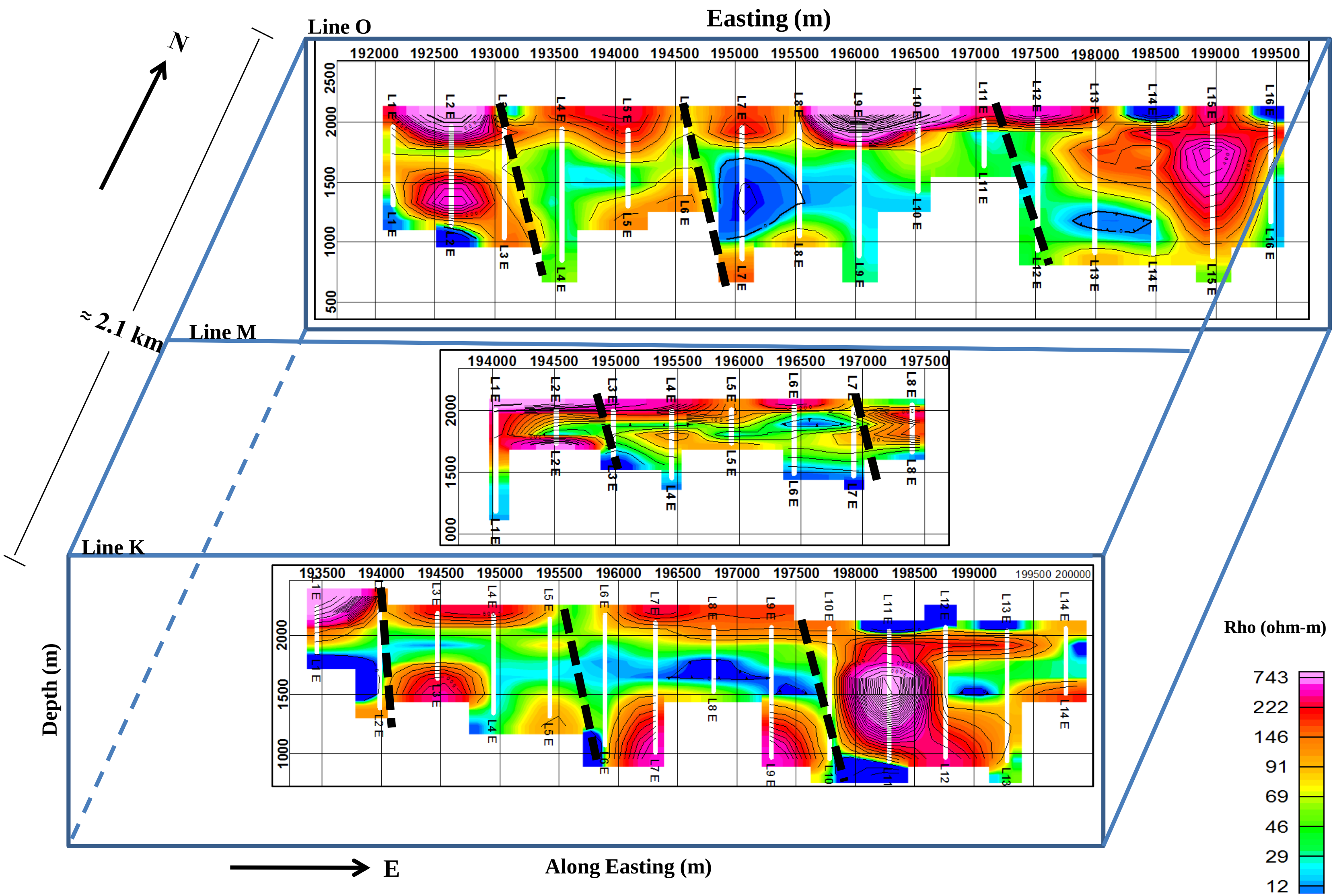

Figure 4.7: 3D Visualization between Survey Lines O, M and K

4.2.4 Geo-electric Structure Beneath Block B

Geo-electric structure beneath block B is presented as both iso-resistivity map and 3D image. It is located in the middle part of the study area (Figure 4.1) oriented in the NW-SE. Cedar hill is located within this block.

4.2.4.1 Iso-resistivity Maps in Block B taken at 2000 m.a.s.l

Iso-resistivity map in block taken at about 2000 m.a.s.l indicates presence of fault line oriented in N-S marked by a low resistivity zone (< 45 Ωm) as illustrated in Figure 4.8. Pockets of low resistivity (< 9 Ωm) are observed consistent with the inferred fault direction; an E-W oriented fault is also present and intersect N-S fault at approximately 90^0.

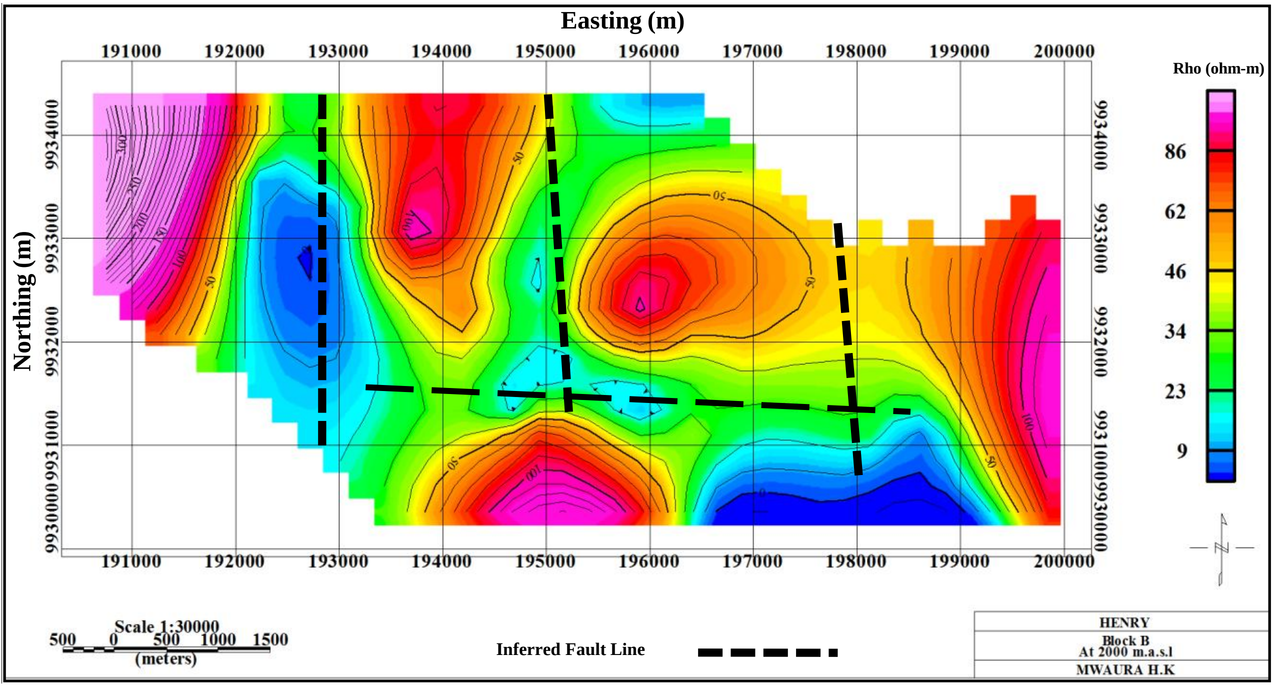

Figure 4.8: Iso-resistivity Map in Block B taken at about 2000 m.a.s.l

4.2.4.2 Combined Lines I-H-G in Block B

A 3D image (Figure 4.9) constructed from juxtaposing lines I, H and G (Figure 3.1) running in NW-SE direction through block B (Figure 4.1), gives strong indication of a 3 layered earth, where resistivity reduces gradually from about 500 Ωm to less than 10 Ωm. The middle geo-electric layer contains highly weathered material marked by resistivity of between 150 Ωm and 20 Ωm. Occasional pockets of low resistivity (< 15 Ωm) are observed within the geo-electric layers and are likely indicators of presence alteration minerals such as smectite and or hot water.

Geo-electric features observed appear to follow N-S direction and consistent with the trend observed from lines O-M-K (Figure 3.1) in block A (Figure 4.1). A conspicuous pattern is observed, where low resistivity convex geo-electric structures occur in association with high resistivity structures convex geo-electric structures. Other notable geo-electric features observed from the 3D map are the vertical geo-electric structures marked by low resistivity of about 100 Ωm. These vertically oriented geo-electric features indicate presence of weathered zones along inferred fault zone or fracture zone.

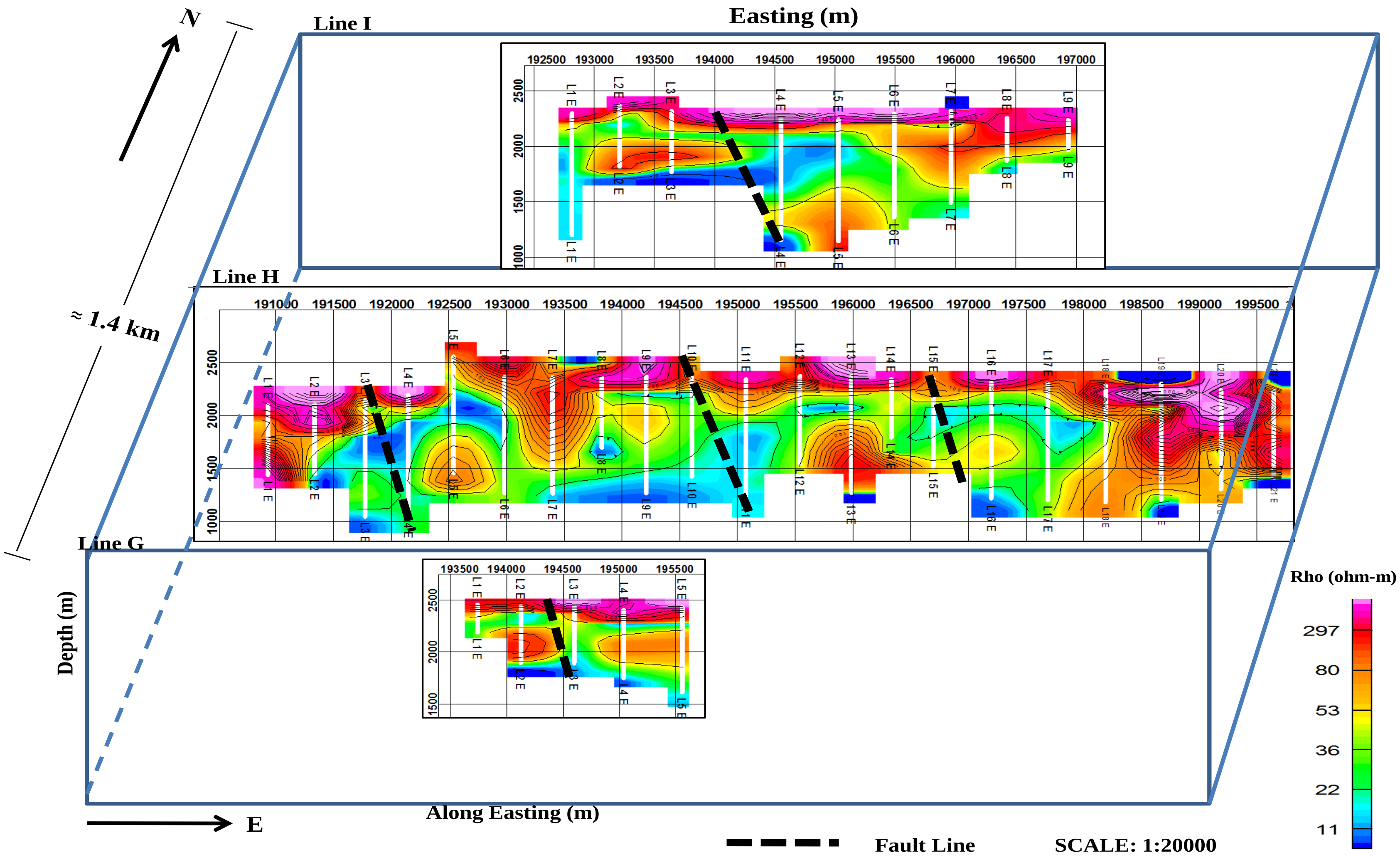

Figure 4.9: 3D Visualization between Survey Lines I, H and G

4.2.5 Geo-electric Structure Beneath Block C

Block C is located approximately within the main Eburru volcanic shield. Six well have been previously drilled in this block.

4.2.5.1 Iso-resistivity Maps in Block C taken at 2000 m.a.s.l

Key horizontal geo-electric structures observed in block C are oriented approximately N-S as marked by low resistivity zone (< 10 Ωm) as illustrated in Figure 4.10. The SW side of block shows a zone of very high electrical resistivity (> 300 Ωm) indicating presence of hot rock adjacent to low electrical resistivity zone (< 10 Ωm) which is an indication of alteration minerals of clay or even hot water; pattern consistent with observation made in the 3D image for block C.

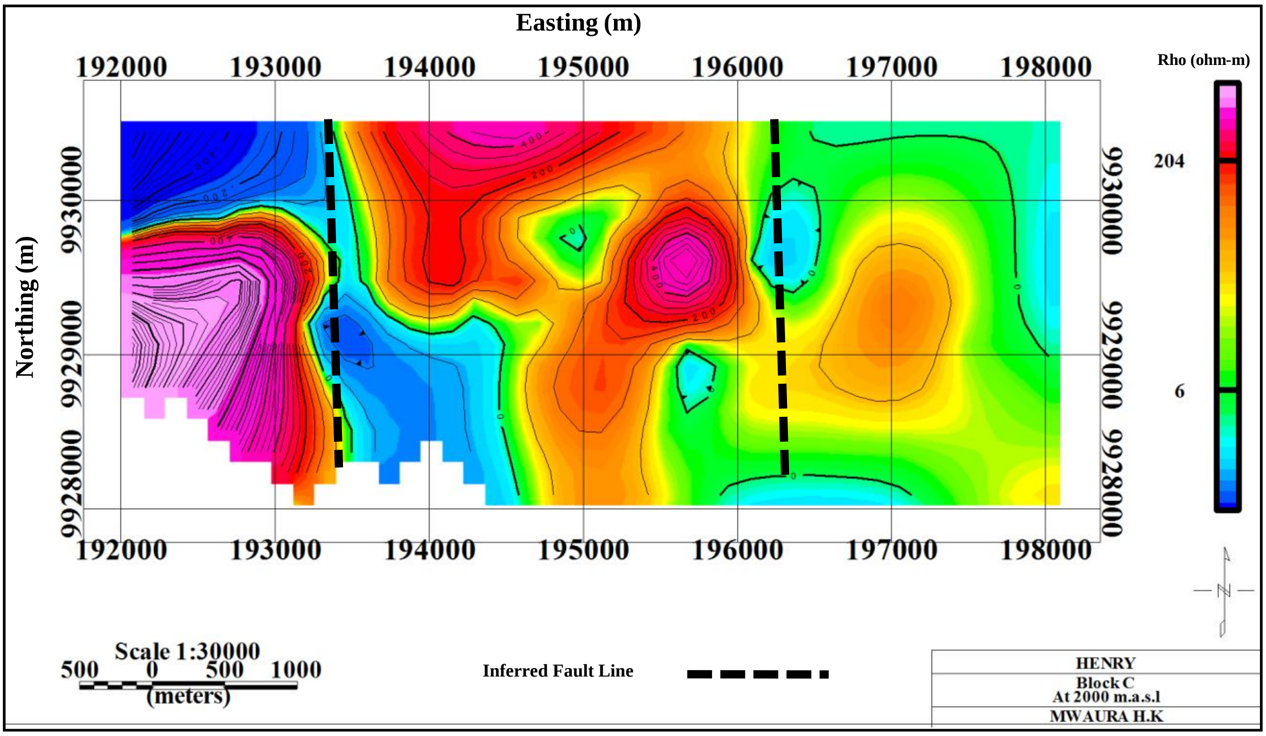

Figure 4.10: Iso-resistivity Map in Block C taken at about 2000 m.a.s.l

4.2.5.2 Combined Lines A-C-R in Block C

A combination of 2D geo-electric sections for lines A-C-R (Figure 3.1) has generated a 3D image (Figure 4.11) in block C where wells 1, 2, 5 and 6 (Figure 4.1) are located. From the 3D visualization, an H-type curve model can be observed where the middle layer has relatively low resistivity compared to its immediate top and bottom layer. The first geo-electric layer terminates at about 2600 m.a.s.l while the second geo-electric layer terminates at valid depths.

Like in previous 3D images (O-M-K and I-H-G), convex geo-electric structures are observed in A-C-R 3D image shown as zones of localized low and high resistivity zones. The low resistivity pockets (< 10 Ωm) are an indication of alteration minerals (smectite and illite). On the other hand, high localized resistivity values are an indication of high temperatures above 200^0c from a hot intrusive body. The high resistivity structure is linearly oriented from N-S and likely indicator of buried fissure volcano.

Other conspicuous features include vertical geo-electric structures marked by low electrical resistivity (< 100 Ωm) an indicator of fault lines/ fracture zone. These features cut across all the three layers and exhibit close correlation with very low resistivity (< 10 Ωm zones).

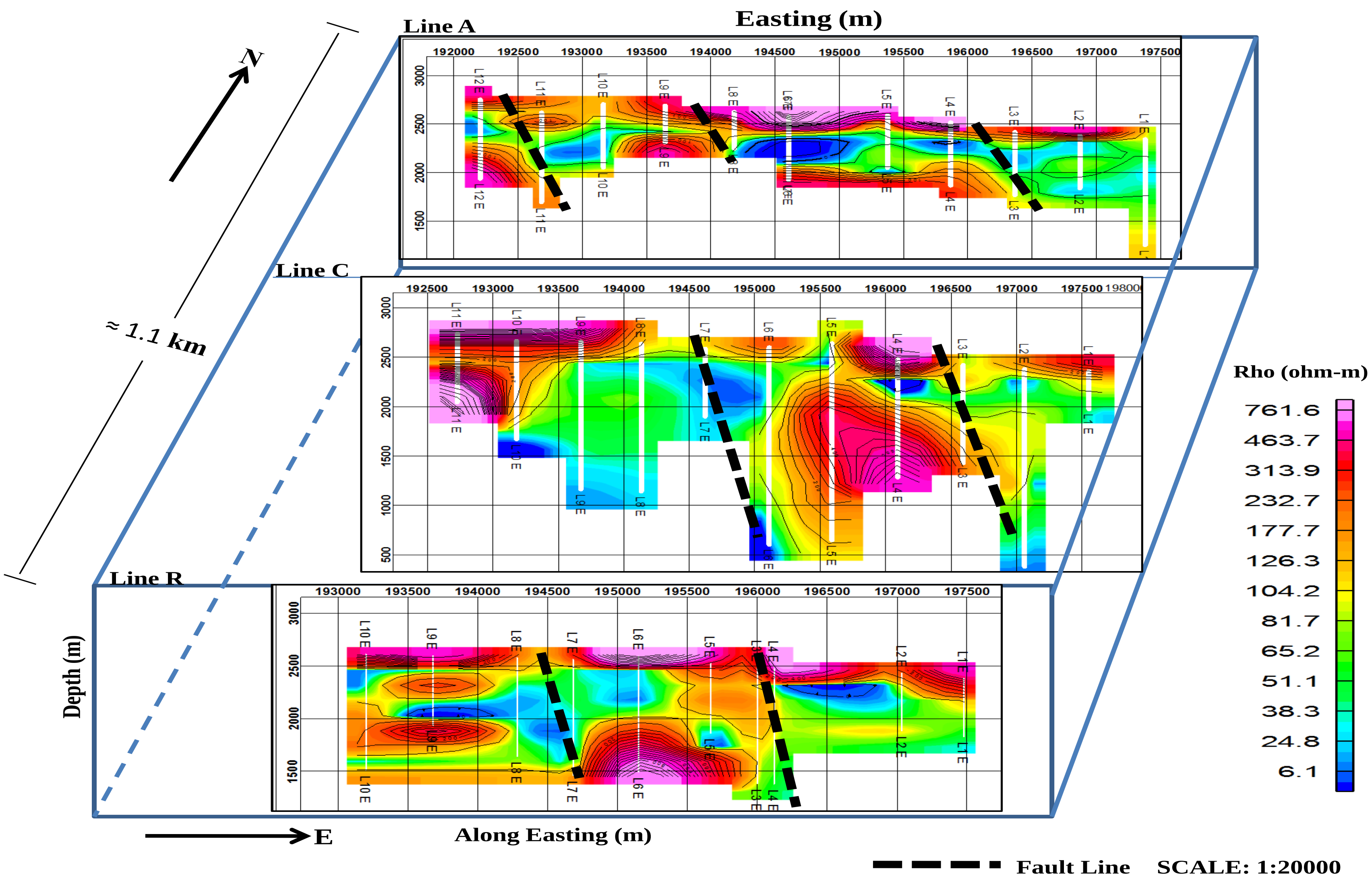

Figure 4.11: 3D Visualization between Survey Lines A, C and R

4.2.5.3 Geo-electric Structure Beneath Entire Study area

A combination of several 2D geo-electric sections from survey line O, K, H and A (Figure 3.1) covering the entire study area, depicts a three layered earth (Figure 4.12), where geo-electric structures are oriented generally in N-S direction.

The intermediate geo-electric layer marked by resistivity between 20 Ωm and 100 Ωm occurs at different depth in all the four 2D geo-electric sections under consideration. The 2D section along survey line-O has the intermediate layer starting at about 1900 m.a.s.l; 2D section along survey line-K starts at 2100m.a.s.l; that of line-H starting at 2300m.a.s.l and finally that of line-A starting at 2600 m.a.s.l.

Convex geo-electric structures marked by zones of low and high localized resistivity value are observed throughout the entire area. The localized high resistivity zone is capped by low resistivity zone as observed in the mid section of survey line K. In other cases, the localized high resistivity values extend to the surface and are indication of a dyke as observed in survey line-H and O (Figure 4.12).

Other conspicuous features are vertical geo-electric structures that intersect all the three geo-electric layers at an angle. They are marked by zones of displacement of geo-electric layers and zones of resistivity between 20 Ωm and 100 Ωm; they represent highly weathered and fractured zones.

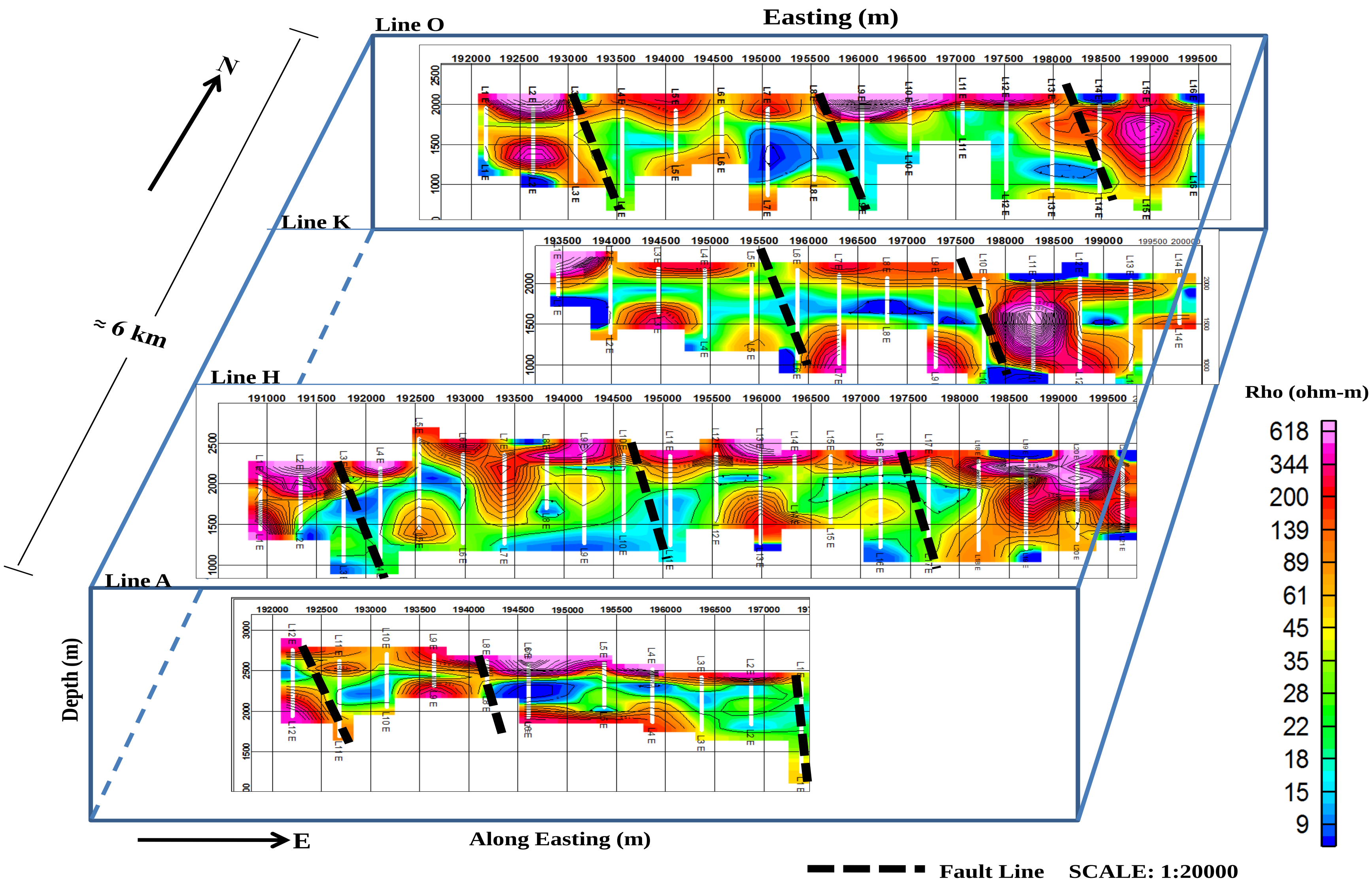

Figure 4.12: 3D Visualization between Survey Lines O, K,-H and A

4.3 Discussions

4.3.1 Geo-electric Structure

Traverses ***I-I′, II-II′, III-III′*** and ***IV-IV′*** (Figure 4.1) coincided with profile 1, 3 ,4 and 8 in Omiti (2013), where he used MT and TEM to create 2D geo-electric sections. TEM and MT gave better resolution at depth > 1000 m as compared to VES which has given better resolution especially for fractured zone along inferred fault lines. However, TEM an MT gives poor resolution at shallow depths as in profile 1 3, 4 and 8 in Omiti (2013).

Convex shaped and localized high resistivity structures have been observed virtually in both 2D geo-sections and 3D map obtained in the study area. They are capped by low resistivity structure, a pattern consistent with c where he observed that the high resistivity (> 200 Ωm) values are as result of high temperatures (> 220^{0}c). The immediate low resistivity (< 10 Ωm) cap is a clear indication of hydrothermal alteration of primary mineral into secondary mineral such as illite and smectite clay minerals (Spichak and Zakharova, 2014). Other localized high resistivity zones stretching from the surface to the bottom have been observed in geo-section along traverse ***I-I′-*** L12E (Figure 4.2) and are indication of hot steam or volcanic plugs.

Horizontal geo-electric structures observed in all the 2D geo-sections, give an impression of a three layered earth. The top layer has high resistivity (200 Ωm) an indication of a dry or unaltered rock formation. The middle geo-electric layer with resistivity (< 150 Ωm), represents a zone of high porosity either due to weathering, unconsolidated material and or fractured rock material where shallow aquifers are. One critical observation worth noting is that aquiferous material in block C shows that the formations dip towards the eastern side to as deep as 1000 m.a.s.l.

Vertical geo-electric structures observed in most of the 2D geo-sections; marked by low resistivity zone (< 100 Ωm) and intersecting geo-electric layers are a clear indication of a fractured zone and or fault line. Stratigraphic information shows that there was loss of circulation during drilling of wells EW 1, 4, and 6, (Figure 3.1) attributed to presence fractures. This is consistent with the results obtained in this study where highly weathered and loosely packed rock materials have been inferred. The vertical geo-electric structures have been observed to occur in association with localized low resistivity structures.

4.3.2 Influence of Shallow Geo-electric Structure to Recharge of Eburru Geothermal Reservoir

Both vertical and horizontal geo-electric structures have a profound effect on the recharge of geothermal reservoir. Fault lines and fractures provide conduits for movement of groundwater. Unconsolidated rock material provides pathway for infiltrating meteoric water. The following sub- section compares the geo-electric structures with information obtained from previously drilled wells in relation to the well productivity.

4.3.2.1 Correlation of Well EW-01 and Geo-electric Section along Survey Line R

Well EW-01 gave a discharge of 2.4 MW with the highest maximum temperature of 278.9^0C at a depth of 1400 m and production casing put (Mwarania, 2014). The results of 2D geo-electric section along survey line R at VES R 126 (Figure 3.1) compares well with the stratigraphic information obtained at well EW-01 drilled to a depth of 2466 m (Figure 4.13). The highly localized high resistivity convex geo-electric structure (> 300 Ωm) coincides approximately with rhyolite as observed in well EW-01 core log. The core log confirms existence of highly fractured zone that is in part related to faulting. This is supported by the core log information, where loss of circulation was reported between 200 m and 800 m.

The adjacent fault line supply water to shallow aquifer where groundwater is temporarily held before it seeps into deep aquifers via the fault line. From the 2D geo-section, it is observed that Well EW-01 is located in a region where the top geo-electric layer extends to about 2500 m.a.s.l hence capping an extended low resistivity layer (< 200 Ωm) between 2000 m.a.s.l and 2500 m.a.s.l. At the same time, well EW-01 is very close to a recharge zone hence probability of oversupply of meteoric water into the tapped reservoir.

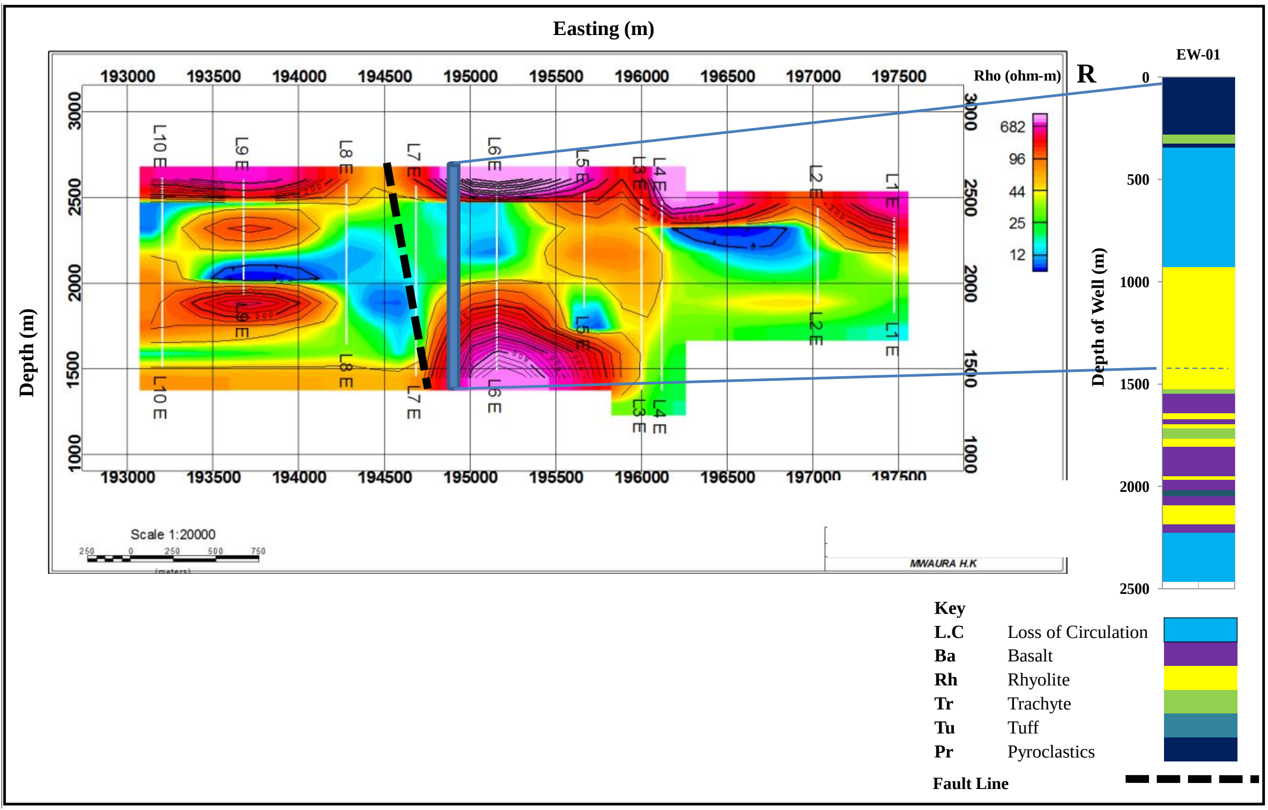

Figure 4.13: Comparison of Geological log of Well EW-01 and 2D geo-section along Survey Line R

4.3.2.2 Correlation of Well EW-02 and Geo-electric Section along Survey Line D

Well EW-02 drilled along or near survey line D at VES D78 (Figure 3.1) did not discharge (Omenda and Karingithi, 1993). A maximum temperature of 140.1^{0}C was recorded at about 1000 m depth (Mwarania, 2014). The stratigraphic pattern of the well closely compare with the geo-electric sections (Figure 4.14). The well intersects a relatively fresh water aquifer (resistivity above 20 Ωm) and located near a fracture zone and a recharge zone which is likely feeding the shallow aquifer.

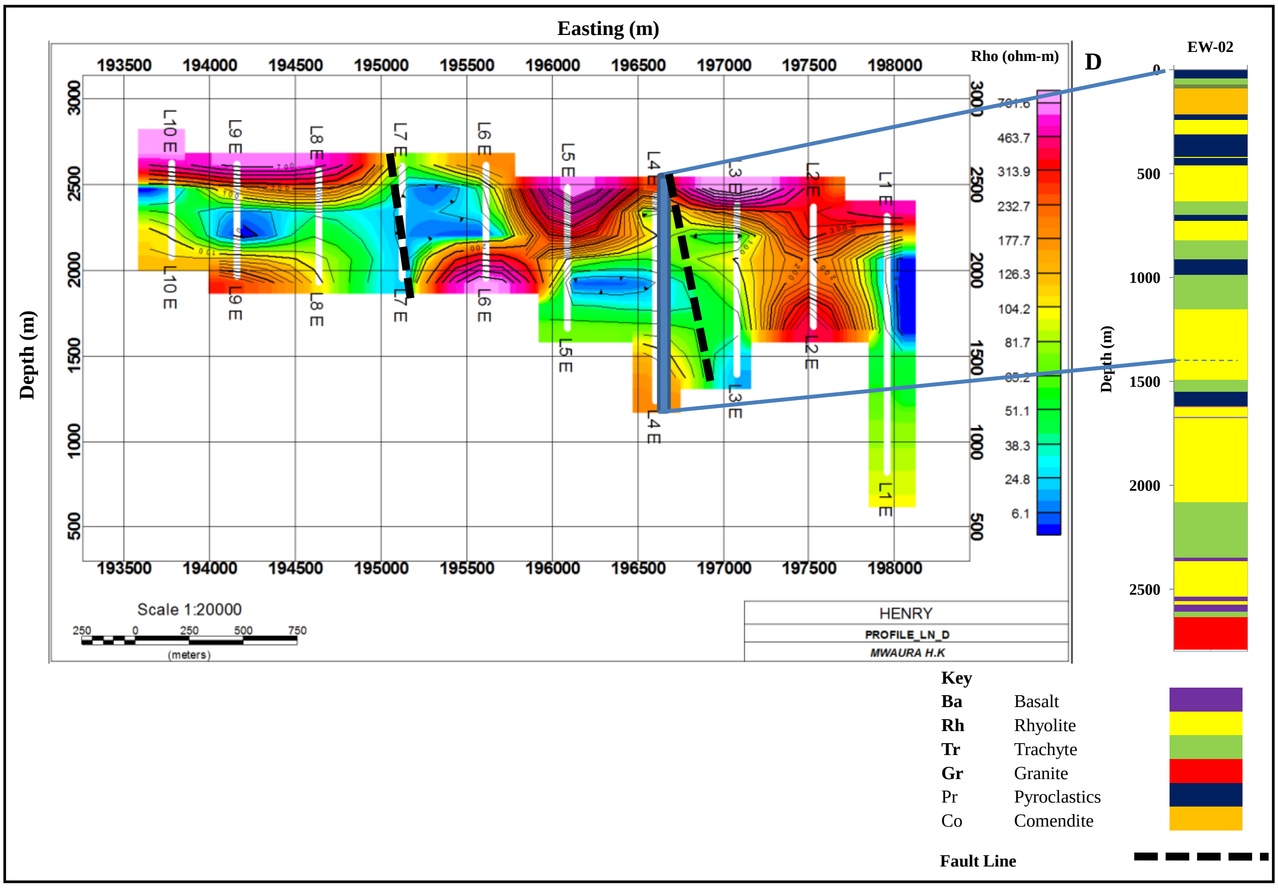

Figure 4.14: Comparison of Geological log of Well EW-02 and 2D geo-section along Survey Line D

4.3.2.3 Correlation of Well EW-03 and Geo-electric Section along Survey Line H

Well EW-03 was drilled to a depth of 2580 m along survey line H (Figure 4.15) but did not discharge. A maximum temperature of 167.8^{0}C was recorded at about 1000 m depth (Mwarania, 2014). It is located in a fractured zone and partially passes through high resistivity (> 200 Ωm) convex structures at about 1500 m.a.s.l. The well is located within a recharge zone and intersects a thick geo-electric layer (> 500 m); with electrical resistivity of about 40 Ωm. This region represents a weathered zone and or highly porous zone. The highly fractured zone facilitates direct infiltration of surface water.

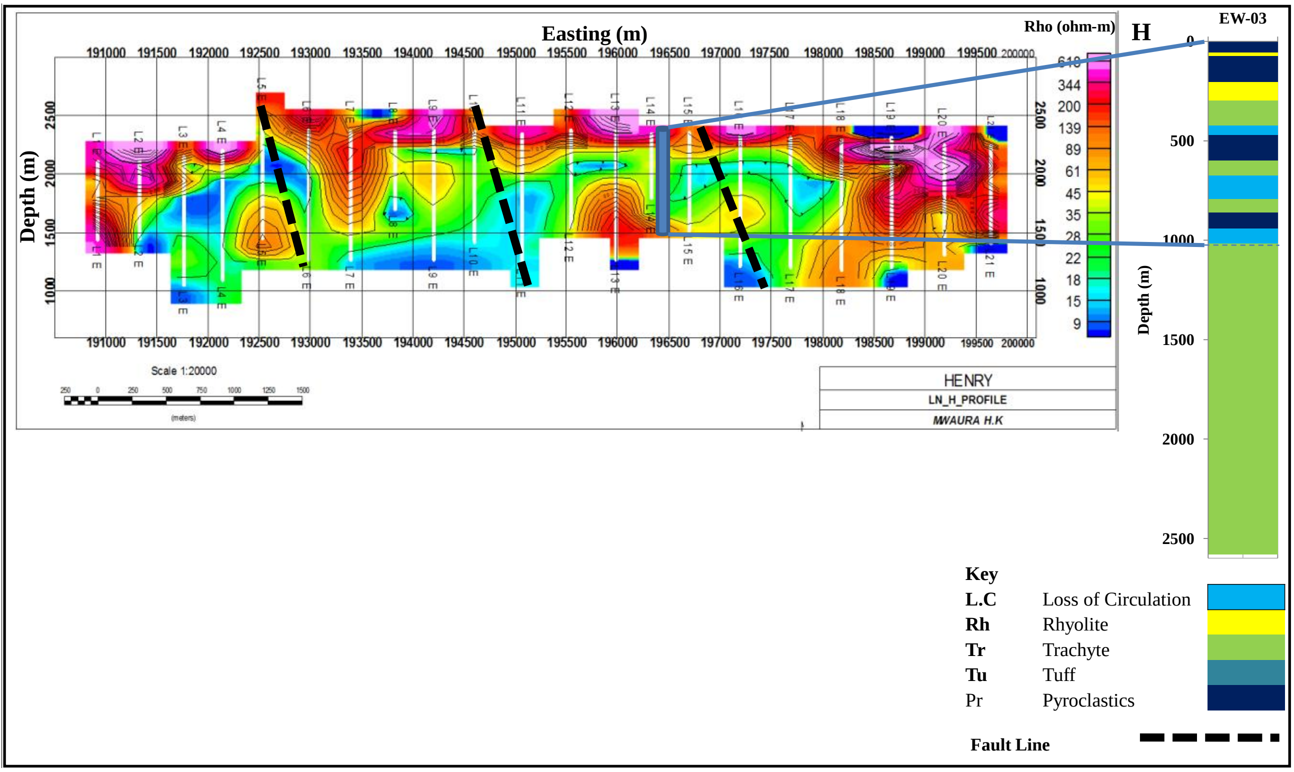

Figure 4.15: Comparison of Geological log of Well EW-03 and 2D geo-section along Survey Line H

4.3.2.4 Correlation of Well EW-04 and Geo-electric Section along Survey Line R

Well EW-04 was drilled to a depth of 2442 m with maximum temperature of about 193.2^{0}C (Mwarania, 2014) and a discharge of about 1.0 MW at 1000 m depth. It was drilled approximately 700 m south of survey line R at VES R142 (Figure 3.1) corresponding to approximately L9E (Figure 4.16). Loss of circulation was reported drilling well EW-04 at a depth about 250 m. This is attributed to the well penetrating a highly weathered or fractured section. The well penetrates a pocket of low resistivity (< 10 Ωm) at a depth of 2000 m a.s.l; likely to be of heated water and a zone of intense hydrothermal alteration into clay minerals.

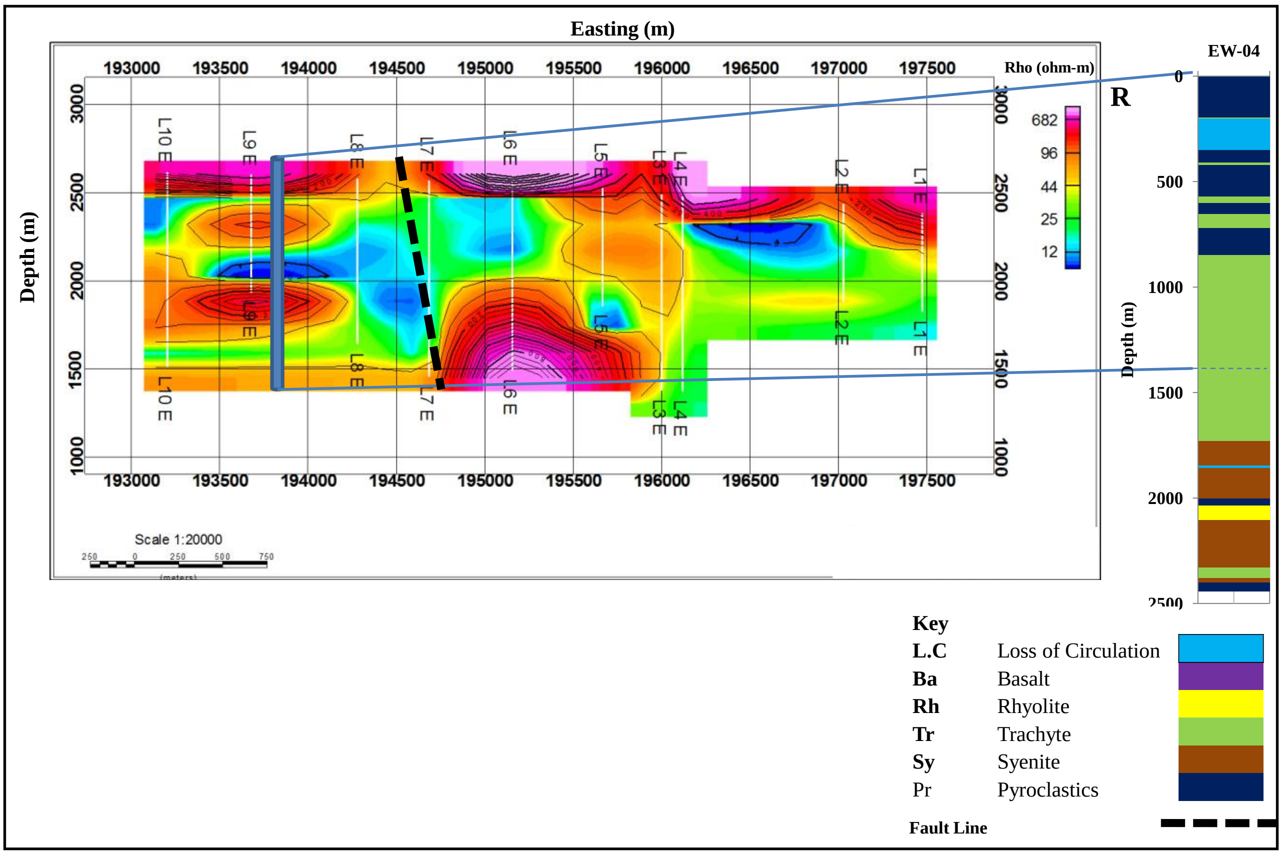

Figure 4.16: Comparison of Geological log of Well EW-04 and 2D geo-section along Survey Line R

4.3.2.5 Correlation of Well EW-05 and Geo-electric Section along Survey Line A

Well EW-05 is located along survey line A at location of VES A81(Figure 3.1) did not discharge according to Omenda and Karingithi (1993) and had a maximum temperature of about 165.5^{0}c at 1000m depth (Mwarania, 2014). The well is located near L9E as illustrated in Figure 4.17 and partially cut across a low resistivity (< 20 Ωm) zone implying nearness or on a recharge area. The zone represents an area of slightly brackish to fresh water, an indication of low temperature zone. The well however, intersects a high resistivity (> 200 Ωm) convex geo-electric structure at about 2200 m.a.s.l; this structure represents slightly elevated temperatures.

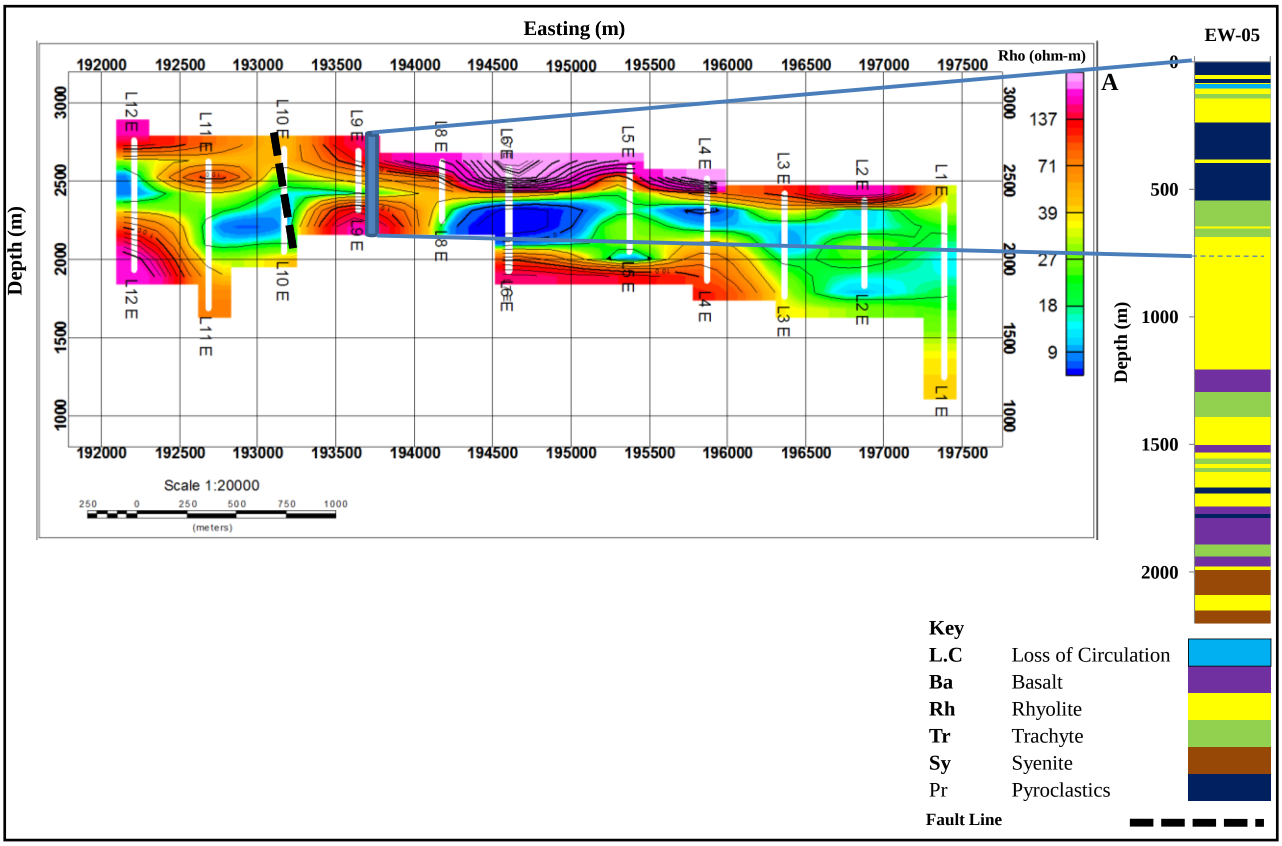

Figure 4.17: Comparison of Geological log of Well EW-05 and 2D geo-section along Survey Line A

4.3.2.6 Correlation of Well EW-06 and Geo-electric Section along Line A

Well EW-06 was drilled to a depth of 2486 m and gave a discharge of about 2.9 MW with maximum temperatures of about 219.9^{0}C at 1000 m (Omenda and Karingithi, 1993). The well is located at L6E along the 2D geo-electric section of survey line A (Figure 4.18) corresponding to VES point A56 (Figure 3.1). Unlike well EW-05, EW-06 penetrated through a low resistivity zone (< 10 Ωm) at a depth of about 2300 m.a.s.l. The low resistivity zone is likely indication of intensive hydrothermal alteration of primary minerals into secondary clay minerals. The well gave the highest discharged likely due to high pressurization of the heated water. At the location of Well EW-06, there is a continuous thick geo-electric layer (> 250 m) of very high resistivity (> 300 Ωm) which represents a fresh and dry rock formation.

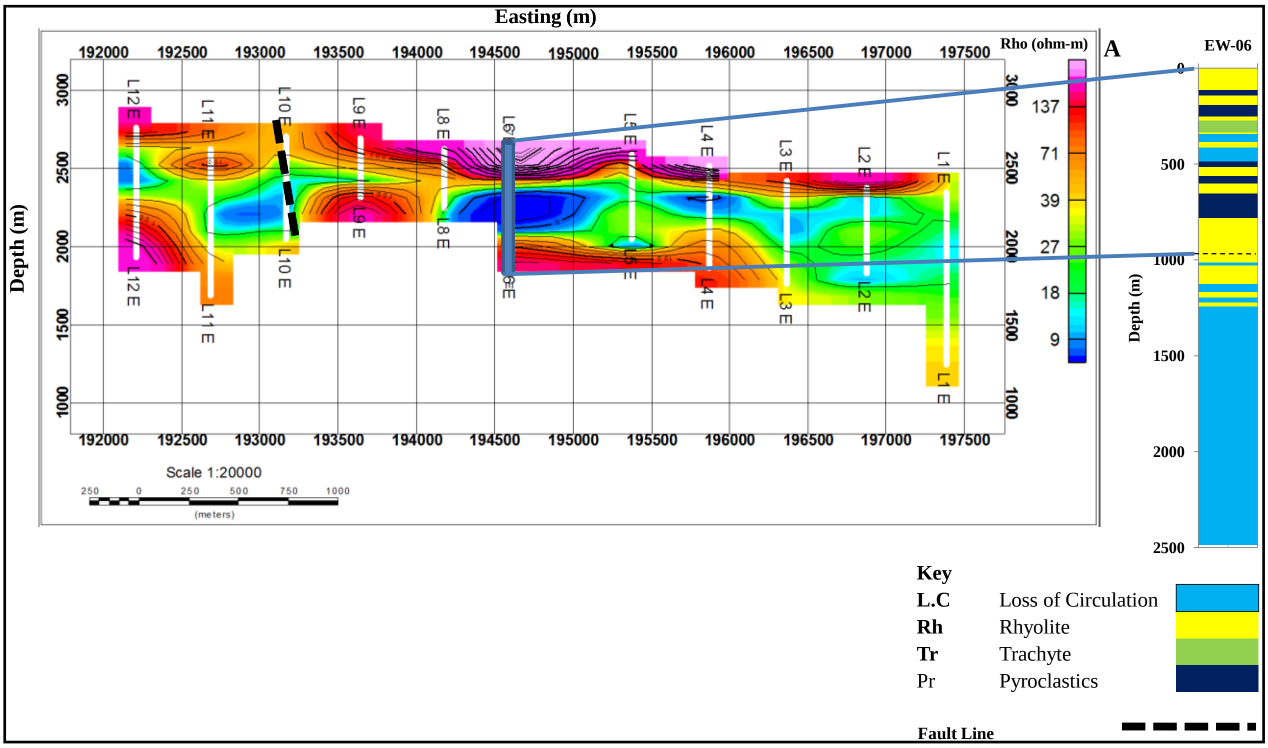

Figure 4.18: Comparison of Geological log of Well EW-06 and 2D geo-section along Survey Line A

Existence of low resistivity pockets (shaded blue) and moderately resistive formations (shaded green) in all the 2D and 3D images is attributed to differential replacement of fractured formation by secondary minerals mainly calcite and clay minerals. This is consistent with the observed breccias in virtually all the geological core logs from the drilled Eburru wells. Well EW-06 gave the highest discharge with temperature of about 219.9^{0}C as compared to well EW-01 which had a maximum temperature of 278.9^{0}C) yet it had lower discharge as compared to well EW-06. All wells (EW 1, 4 and 6) (Figure 4.1) located slightly far from the recharge area did discharge while wells (EW 2, 3, and 5) (Figure 4.1) located on or near a recharge zone didn't discharge. The discharging wells were observed to have a capping clay layer (shaded blue) at about 2250 m.a.s.l. A static water level was registered at about 1836 m.a.s.l and 1814 m.a.s.l in well EW-01 and EW-06 respectively; which is consistent with the surface elevation of Lake Naivasha (Mwarania, 2014). However, the rest of the wells were slightly lower by 100 m.

From the geophysical results and the Eburru well log data, a pattern is observed where discharging wells are located away from the fracture zone and in their place replaced by highly resistant formation. On the other hand, wells which did not discharge are located in inferred fractured zones.

4.3.3 Piezometric Surface Map

Piezometric surface map of the larger Nakuru County shows that the general recharge pattern is from the flanks of the rift valley (lateral recharge) while the discharge is axially along the rift. The high (Red – orange) in Figure 4.19 shows zone of higher hydraulic head and areas shown in blue indicates zones of low hydraulic head a pattern consistent with the general trend of the surface elevation and rift orientation. In the NW side of the study area, the hydraulic head drop to about 1450 m implying shallow groundwater flow towards that side.

The implication of the groundwater flow direction in the shallow aquifer is that there is higher chance for water to flow away from the Eburru geothermal reservoir rather than percolating into the deep aquifer. The piezometric surface map indicates that lateral ground water flow is largely controlled by successive volcanic formations rather than the fault lines.

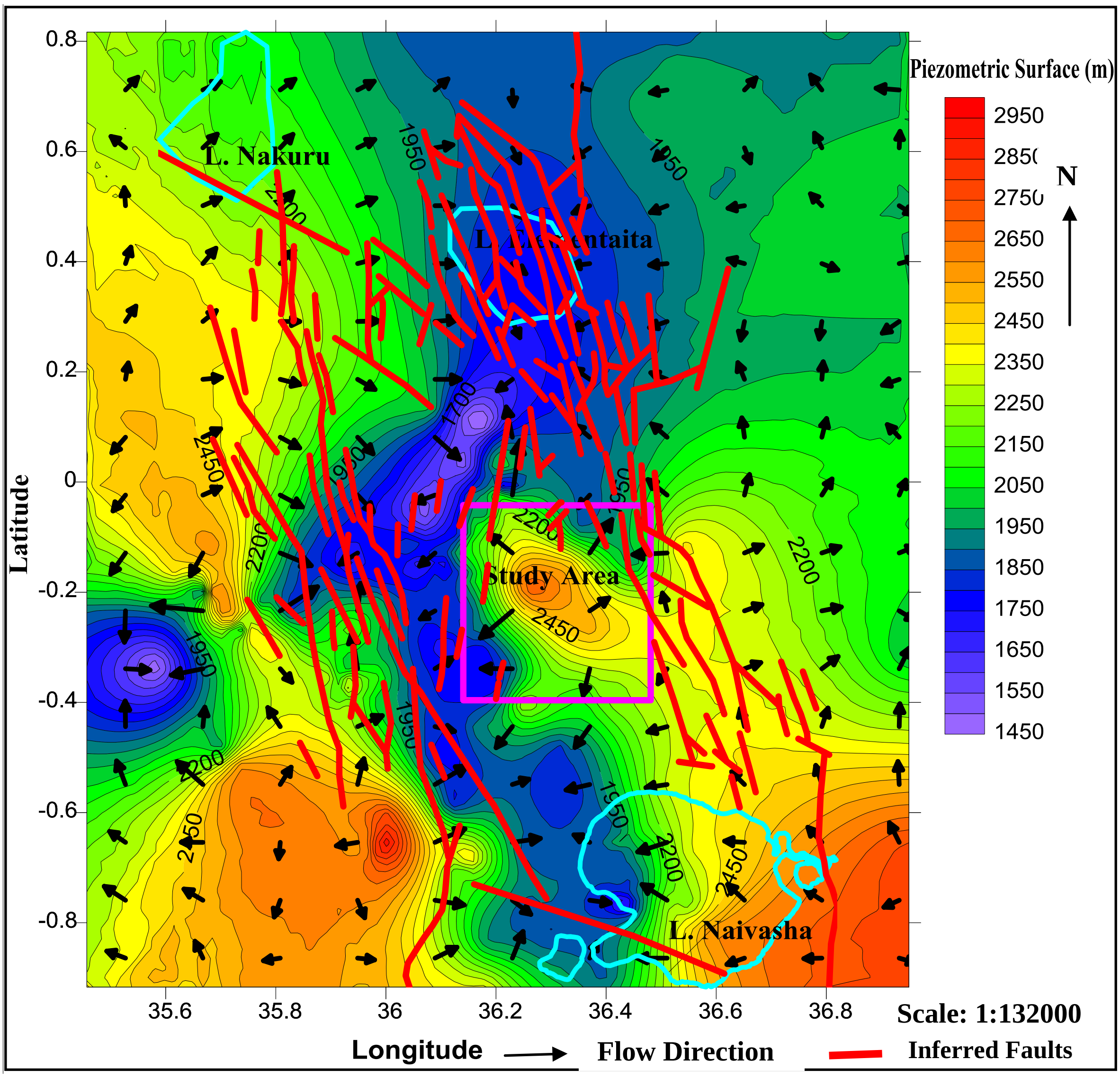

Figure 4.19: A Piezometric Surface Map of Nakuru County. The Study area is marked in purple rectangle.

4.3.4 *Shallow and Deep Aquifers*

There are two main aquifers in the study area i.e. deep and shallow aquifers. The result of geophysical analysis indicates that shallow aquifers are hosted within the first 200 m from the surface, contained in weathered trachyte and pyroclastic material. Deep aquifers on the other hand occur at more than 500 m below the surface as confirmed from the resistivity pattern. Deep aquifers are saline as has been observed from resistivity values < 12 Ωm.

The vertical electrical sounding method has given better resolution for shallow (< 1000 m) geo-electric structures, but at greater depths, the electrical resistivity becomes unstable hence VES method not suitable for detecting deep structures. Geological in-homogeneities affect quality of VES data; however this was overcame by presence of closely spaced survey lines and data points (< 450 m).

CHAPTER 5.0: CONCLUSIONS AND RECOMMENDATIONS

5.1 Conclusions

5.1.1 Shallow Geological Structures

From the research findings, it is envisaged that the study area is a three layered earth up to a depth of 1000 m.b.g.l. The layering is concluded to be as a result of: - rock types; differential weathering; uneven temperature distribution within the rock system; water within the pores; pore connectivity and chemical composition of dissolved minerals among others. Slight variations within these layers especially the middle one could be as a result of replacement minerals (calcite and clays among others) within the fractured formation.

Cross cutting vertical geo-electric features are interpreted to be fault lines and have connected shallow aquifers to deep aquifers. Siting of a productive well is directly related to the recharge pattern; the pattern is influenced by the shallow geological structures. Buried fissure volcanoes have acted as barriers; this is evident from the formation of low resistivity zone adjacent to them.

Pockets of low resistivity (< 10 Ωm) observed in the study area contains low temperature secondary minerals such as smectite and illite that have low electrical resistivity signature.

5.1.2 Influence of Shallow Geological Structures to Recharge of Geothermal Reservoir

On the basis of the research findings, it can be concluded that the geothermal reservoir is recharged from both the surface infiltration and deep faults.

Buried fissure volcanoes have facilitated accumulation of water behind them and in some cases dictated groundwater flow. Water hosted within the shallow aquifers is temporary held as it flows into deep aquifers via the fault zone. The accumulation of water in the shallow aquifer is faster than it is in deep aquifers and eventually into the geothermal reservoir. Clay layer play a pivotal role in capping the geothermal reservoir hence allowing the geothermal fluids to circulate within the reservoir.

5.1.3 Relationship between Shallow and Deep Aquifers

Fault zones in the study area contain highly weathered material and are aquiferous; they act as conduits from which shallow semi-confined aquifers interact with deep aquifers. Presence of pockets of clay has been observed in all the section especially along inferred faults causing damming of water behind the fault.

5.2 Recommendations

To establish fluid flow pattern, a geochemical analysis should be carried out for groundwater in Eburru geothermal field and the hot springs in the Elementaita area in order to establish whether groundwater in Eburru seeps out in Elmenteita area.

More deep boreholes should be sunk in the study area in order to continuously monitor the ground water flow pattern especially between Lake Naivasha and Elementaita catchment area/ basins.

REFERENCES

Aguado, T. (2010). Los Azufres Conceptual Modelling in Mexican Geothermal Field. Geotermia, **26**(2), 1–38.

Aizebeokhai, A. P. (2010). 2D and 3D geoelectrical resistivity imaging : Theory and field design. Scientific Research and Essays, **5**(23), 3592–3605.

Arusei, M. K. (1991). Hydrochemistry of Olkaria and Eburru Geothermal Fields, Kenyan Rift Valley (No. 2) Reykjavik, Iceland: Unpublished.

Barongo, J. (1982). Eburru Geothermal Prospect, Riftvalley Kenya (No.15). Nairobi, Kenya: Unpublished Technical/ Training Report, Ministry of Energy Kenya.

Barongo, J. O. (2016). Conversion Software for Apparent Resistivity Data for EarthImager. *Per comm*.

Biggs, J., Anthony, E. Y., and Ebinger, C. J. (2009). Multiple inflation and deflation events at Kenyan volcanoes, East African Rift. Geology Society of America, **37**(11), 979–982.

Flores, C., and López-moya, A. (2011). A comparison of three geoelectric methods in the presence of shallow 2-D inhomogeneities : A case study. Geofísica Internacional, 371–399.

Gad, E., Ushijima, K., and Ahmed, E. (2000). Delineation of Geothermal Reservoir by 2D Inversion of Resistivity Data at Hamam Faraun Area, Sinai, Egypt. In World Geothermal Congress 2000 (1103–1108). Kyushu-Tohoku, Japan: Conference Paper.

Ha, N. H. (1997). The Use of Schlumberger Sounding in Geothermal (Report No.6). Reykjavik. Iceland, Iceland: Unpublished Report in UNU.

Harðarson, B. S., Flóvenz, Ó. G., and Axelsson, G. (2012). Geothermal Systems. Iceland: Unpublished Report in UNU.

Herman, R. (2001). An introduction to electrical resistivity in geophysics. American Association of Physics Teachers, **69**(9), 943 – 952.

Hersir, G. P., and Árnason, K. (2009). Resistivity of rocks. Short Course IV on Exploration for Geothermal Resources. Reykjavik. Iceland: Unpublished.

Kariuki, P., and Russell, K. (2007). GIS Services. Open access ILRI Database.

KENGEN. (1990). Geological Logs for Eburru Wells. Kenya: KENGEN Internal Report.

Kiende, R., and Kandie, R. (2015). Structural Geology of Eburru Volcano and Badlands Geothermal Prospects in Kenya. In Fourtieth Workshop on Geothermal Reservoir Engineering 1–10. Stanford.

Koefoed, O., and Mallick, K. (1979). Geosounding Principles: Resistivity sounding measurements (2nd edition.). Elsevier Scientific Publishing Company.

Kuria, Z. N. (2011). Seismotectonics of Active Faults : Magadi Fault System, Southern Kenya Rift. 1 - 210; Published Dissertation in the University of Twente.

Lagat, J. (2003). Geology and the geothermal systems of the southern segment of the Kenya Rift. International Geothermal Conference, 33–40.

Leli, P., Oldenburg, D., and Williams, N. (2003). Constraining geophysical inversions with geologic information. Earth, (m), 1–4.

Loke, M. H. (2013). Tutorial : 2-D and 3-D electrical imaging surveys. Geotomo Software Malaysia. Unpublished.

Lowrie, W. (2007). Fundamentals of geophysics. Cambridge University press (Second Edition). Cambridge: Cambridge University Press.

Mang'erere, O. S. (2005). Morphological Structure and the Anthropogenic Dynamics in the Lake Naivasha Drainage Basin and its Implications to Water Flows. In Topics of Intergrated Watershed Management . **3**, 141–160.

Mburu, M. (2009). Geothermal Energy Utilization. In Exploration for Geothermal Resources 1–11. Naivasha, Kenya, Kenya: Unpublished Report in UNU.

Mwangi, A. W. (2012). Eburru Geothermal Prospect, Kenya—Joint 1D Inversion of MT and TEM Data. In Thirty-Seventh Workshop on Geothermal reservoir Engineering 1–7. Unpublished Paper.

Mwarania, F. M. (2014). Reservoir Evaluation and Modelling of the Eburru Geothermal System, Kenya. United Nations University.

Odada, E., Olago, D., Ochola, W., Ntiba, M., Wandiga, S., Gichuki, N., and Oyieke, H. (2005). 11th Wold Lakes Conference. **2,** 1-639. Conference Proccedings; Ministry of Water and Irrigation International Lake Environment Committee.

Olaka, L. A. (2011). Hydrology Across Scales: Sensitivity of East African Lakes to Climate Changes. Published Dissertation in Universität Potsdam.

Omenda, P., and Karingithi, C. (1993). Hydrothermal Model of Eburru Geothermal Field, Kenya. Geothermal Resource Council Transactions, **17**(4), 155–160.

Omiti, A. (2013). Resistivity Structure of the Eburru Geothermal Field, Kenya Depicted Through 1D Joint Inversion of MT and TEM Data (No.26). World Geothermal Congress 2015. Reykjavik, Iceland: Unpublished.

Onacha, S. A. (1990). Application of Schlumberger Sounding at Eburru , Kenya and TEM and MT Methods at Bakki , S-Iceland (No. 11). Reykjavik. Iceland: Unpublished Report in UNU.

Reta, G. L. (2011). Groundwater and Lake Water Balance of Lake Naivasha Using 3-D Transient Groundwater Model Groundwater and Lake Water Balance of Lake Naivasha Using 3-D Transient Groundwater Model. 1-54. Unpublished Thesis inUniversity of Twente.

Roy, K. (2008). Inversion of Potential Field Data. 561–624. Springer Berlin Heidelberg.

Rutley, F. (1988). Rutleys Element of Mineralogy, 1-482. edition. New Delhi : ISBN: 8123909160, CBS Publishers and Distributors.

Saemundsson, K. (2008). East African Rift System - an Overview. Short Course III on Exploration for Geothermal Resources. Kenya: Unpublished.

Spichak, V., and Zakharova, O. (2014). Electromagnetic Geothermometry. ISBN: 9780128022108; Elsevier.

Thompson, A. (1956). Geological Map of the Naivasha Area. Accompanying Report No. 55; Kenya.

Thompson, A., and Dodson, R. (1963). Geology of the Naivasha Area (No. 55). Kenya: Unpublished.

Ussher, G., Harvey, C., Johnstone, R., Anderson, E., and Zealand, N. (2000). Understanding the resistivities observed in geothermal systems. In Proceedings World Geothermal Congress. 1915–1920. Kyushu-Tohoku, Japan: World Geothermal Congress.

Ward, S. (1990). Resistivity and Induced Polarization Methods. In Geotechnical and Environmental geophysics. 147–190. Society of Exploration Geophysicists.

Yihdego, Y. (2005). A three dimensional ground water model of the aquifers around Lake Navaisha area, Kenya. 1–107: Unpublished thesis in International Institute for Geo-information Science and Earth Observation.

APPENDICES

Appendix 1: FORTRAN Codes for Converting Raw VES Data for use in Earth Imager (Barongo, 2016)

```
C   Last change:  G    22 Feb 2016    5:05 pm
      DIMENSION ab2(50),xmn2(50),rho(50),xk(50),vi(50)
      CHARACTER*20 fname1, fname2
      Write (*,'(a\)') 'Enter filename for input :--------->       '
      read(*,'(a20)') fname1
      write(*,'(a\)') 'Enter filename for output:--------->       '
      read(*,'(a20)') fname2
      OPEN(10,file=fname1)
      OPEN(20,FILE=fname2)
      pi=3.14159265
      READ(10,*) n
      do 5 i=1,n
 5    READ(10,*) ab2(i),xmn2(i),rho(i)
      do 10 i=1,n
      xk(i)=(pi*ab2(i)**2)/(2.0*xmn2(i))
      vi(i)=rho(i)/xk(i)
 10   continue
      do 15 i=1,n
 15   WRITE(20,20) i,ab2(i),xmn2(i),vi(i)
 20   FORMAT(i4,1x,f8.0,1x,f6.1,1x,f10.6)
      stop
      end
```

Appendix 2: Modeled VES Data within the Study Area (Barongo, 1982)

Traverse I-I′

VES Station A48

Layer	Est. (m)	Depth (m.a.s.l)	E.R (Ωm)
1	194603	2581	447.1
2	194603	2574	885.4
3	194603	2560	1723.0
4	194603	2532	743.1
5	194603	2414	22.4
6	194603	2227	4.3
7	194603	1924	33.4

VES Station A56

Layer	Est. (m)	Depth (m.a.s.l)	E.R (Ωm)
1	194604	2582	463.3
2	194604	2582	2202.3
3	194604	2579	917.0
4	194604	2570	2489.9
5	194604	2560	667.2
6	194604	2528	998.2
7	194604	2427	88.9
8	194604	2085	18.3
9	194604	1924	272.1

VES Station A74

Layer	Est. (m)	Depth (m.a.s.l)	E.R (Ωm)
1	194181	2628	39.0
2	194181	2624	169.7
3	194181	2616	635.6
4	194181	2598	249.2
5	194181	2506	73.3
6	194181	2245	19.9

VES Station A81

Layer	Est. (m)	Depth (m.a.s.l)	E.R (Ωm)
1	193643	2693	57.9
2	193643	2691	174.7
3	193643	2685	536.6
4	193643	2679	188.8
5	193643	2667	42.9
6	193643	2605	110.9
7	193643	2449	9.6
8	193643	2310	136.8

VES Station A86

Layer	Est. (m)	Depth (m.a.s.l)	E.R (Ωm)
1	193165	2708	29.2
2	193165	2707	24.8
3	193165	2705	40.6
4	193165	2698	106.1
5	193165	2683	71.4
6	193165	2665	39.9
7	193165	2548	27.8
8	193165	2086	23.0
9	193165	2050	34.0

VES Station A93

Layer	Est. (m)	Depth (m.a.s.l)	E.R (Ωm)
1	192682	2624	20.5
2	192682	2622	5.4
3	192682	2619	29.4
4	192682	2611	105.2
5	192682	2576	22.3
6	192682	2530	108.1
7	192682	2440	38.0
8	192682	2089	18.9
9	192682	1691	76.6

VES Station A102

Layer	Est. (m)	Depth (m.a.s.l)	E.R (Ωm)
1	192206	2759	239.3
2	192206	2757	22.1
3	192206	2755	34.2
4	192206	2749	137.6
5	192206	2742	76.6
6	192206	2688	49.4
7	192206	2628	30.8
8	192206	2377	13.6
9	192206	1935	241.1

VES StationC87

Layer	Est. (m)	Depth (m.a.s.l)	E.R (Ωm)
1	197553	2359	45.1
2	197553	2358	173.7
3	197553	2358	536.6
4	197553	2354	253.2
5	197553	2337	1210.5
6	197553	2285	101.2
7	197553	2198	44.2
8	197553	1975	23.5

Traverse I-I′

VES Station C95

Layer	Est. (m)	Depth (m.a.s.l)	E.R (Ωm)
1	197062	2380.7	37.0
2	197062	2377.3	201.0
3	197062	2365.5	51.7
4	197062	2365.5	149.0
5	197062	2347.3	414.5
6	197062	2310.9	6.0
7	197062	2142.3	19.3
8	197062	1825.0	62.4
9	197062	382.0	12.4

VES Station C99

Layer	Est. (m)	Depth (m.a.s.l)	E.R (Ωm)
1	196592	2424.7	15.4
2	196592	2412.6	60.5
3	196592	2333.2	12.3
4	196592	2197.5	205.3
5	196592	2084.7	21.6
6	196592	1885.5	53.7
7	196592	1430.0	177.4

VES Station C105

Layer	Est. (m)	Depth (m.a.s.l)	E.R (Ωm)
1	196094	2480.0	1050.9
2	196094	2474.9	1318.0
3	196094	2454.0	188.6
4	196094	2345.8	39.0
5	196094	2109.5	7.9
6	196094	1283.0	840.1

VES Station C116

Layer	Est. (m)	Depth (m.a.s.l)	E.R (Ωm)
1	195589	2645.2	100.9
2	195589	2642.7	11.7
3	195589	2639.7	75.7
4	195589	2636.4	36.3
5	195589	2624.6	4.6
6	195589	2606.6	7.0
7	195589	2562.7	27.7
8	195589	2489.4	8.1
9	195589	1853.6	464.6
10	195589	647.0	105.1

VES Station C123

Layer	Est. (m)	Depth (m.a.s.l)	E.R (Ωm)
1	195111	2600.2	260.5
2	195111	2598.8	424.7
3	195111	2596.3	55.4
4	195111	2591.1	107.0
5	195111	2581.1	159.8
6	195111	2557.1	79.5
7	195111	2516.8	7.7
8	195111	2434.9	38.7
9	195111	2285.6	20.4
10	195111	2013.9	13.2
11	195111	1614.9	71.3
12	195111	603.0	7.6

VES Station D78

Layer	Est. (m)	Depth (m.a.s.l)	E.R (Ωm)
1	196602	2435.4	34.3
2	196602	2433.1	99.9
3	196602	2431.1	156.5
4	196602	2423.2	598.7
5	196602	2408.1	323.8
6	196602	2390.6	86.7
7	196602	2313.7	21.7
8	196602	2207.7	101.1
9	196602	1840.3	19.7
10	196602	1238.0	183.6

VES Station D85

Layer	Est. (m)	Depth (m.a.s.l)	E.R (Ωm)
1	196092	2482.2	69.4
2	196092	2464.9	1371.5
3	196092	2423.7	6.1
4	196092	2344.0	525.5
5	196092	1934.7	3.1
6	196092	1660.0	71.5

VES Station D89

Layer	Est. (m)	Depth (m.a.s.l)	E.R (Ωm)
1	195615	2610.6	36.1
2	195615	2600.1	219.1
3	195615	2579.9	352.2
4	195615	2542.1	14.6
5	195615	2441.3	81.0
6	195615	2188.8	8.8
7	195615	1952.0	785.5

Traverse II-II′

VES Station A56

Layer	Nthg.(m)	Depth (m.a.s.l)	E.R (Ωm)
1	9929869	2582	463.3
2	9929869	2582	2202.3
3	9929869	2579	917.0
4	9929869	2570	2489.9
5	9929869	2560	667.2
6	9929869	2528	998.2
7	9929869	2427	88.9
8	9929869	2085	18.3
9	9929869	1924	272.1

VES Station C130

Layer	Nthg.(m)	Depth (m.a.s.l)	E.R (Ωm)
1	9929692	2591	54.9
2	9929692	2589	96.3
3	9929692	2581	139.6
4	9929692	2573	12.5
5	9929692	2455	19.2
6	9929692	2324	10.2
7	9929692	1897	15.9

VES Station D102

Layer	Nthg.(m)	Depth (m.a.s.l)	E.R (Ωm)
1	9929510	2586	1454.2
2	9929510	2584	522.6
3	9929510	2580	154.3
4	9929510	2572	108.1
5	9929510	2563	299.3
6	9929510	2545	101.0
7	9929510	2407	33.2
8	9929510	1938	20.3
9	9929510	1928	187.8

VES Station E120

Layer	Nthg.(m)	Depth (m.a.s.l)	E.R (Ωm)
1	9930397	2542	134.0
2	9930397	2539	428.4
3	9930397	2529	619.0
4	9930397	2507	6.0
5	9930397	2445	103.5
6	9930397	2281	4.6
7	9930397	1996	448.2

VES StationG136

Layer	Nthg.(m)	Depth (m.a.s.l)	E.R (Ωm)
1	9931267	2438	426.0
2	9931267	2434	1864.1
3	9931267	2425	902.1
4	9931267	2399	99.5
5	9931267	2266	43.5
6	9931267	1889	13.5

VES Station R126

Layer	Nthg.(m)	Depth (m.a.s.l)	E.R (Ωm)
1	9929277	2561	86.4
2	9929277	2559	515.3
3	9929277	2557	154.9
4	9929277	2550	5.5
5	9929277	2534	9.3
6	9929277	2455	18.8
7	9929277	2239	23.4
8	9929277	1584	12.2
9	9929277	1462	56.6

VES Station T145

Layer	Nthg.(m)	Depth (m.a.s.l)	E.R (Ωm)
1	9928879	2561	476.0
2	9928879	2561	34.3
3	9928879	2561	700.4
4	9928879	2535	59.0
5	9928879	2475	27.1
6	9928879	2325	64.6
7	9928879	2256	5.1
8	9928879	2036	71.8

Modeled VES Data within the Study Area Continued

Traverse III-III′
VES Station A40

Layer	Nthg.(m)	Depth (m.a.s.l)	E.R (Ωm)
1	9929951	2594.4	301.0
2	9929951	2590.5	429.2
3	9929951	2540.6	118.4
4	9929951	2360.3	15.4
5	9929951	2098.0	26.8
6	9929951	2046.0	14.1
	VES Station C116		
1	9929711	2645.2	100.9
2	9929711	2642.7	11.7
3	9929711	2639.7	75.7
4	9929711	2636.4	36.3
5	9929711	2624.6	4.6
6	9929711	2606.6	7.0
7	9929711	2562.7	27.7
8	9929711	2489.4	8.1
9	9929711	1853.6	464.6
10	9929711	647.0	105.1
	VES Station D89		
1	9929563	2610.6	36.1
2	9929563	2600.1	219.1
3	9929563	2579.9	352.2
4	9929563	2542.1	14.6
5	9929563	2441.3	81.0
6	9929563	2188.8	8.8
7	9929563	1952.0	785.5
	VES Station G120		
1	9930904	2435.6	633.1
2	9930904	2428.0	1126.8
3	9930904	2409.7	1868.6
4	9930904	2361.1	201.5
5	9930904	2262.9	13.7
6	9930904	2115.6	88.6
7	9930904	1612.0	20.0
	VES Station H120		
1	9931574	2373.9	58.3
2	9931574	2371.5	864.9
3	9931574	2368.3	96.9
4	9931574	2361.3	263.0
5	9931574	2347.8	69.5
6	9931574	2318.0	190.5
7	9931574	2253.6	68.9
8	9931574	2086.4	15.4
9	9931574	1550.0	37.9
	VES Station I87		
1	9932397	2293.1	970.8
2	9932397	2290.7	1324.1
3	9932397	2280.4	732.6
4	9932397	2262.6	543.0
5	9932397	2256.0	116.1
6	9932397	2196.6	53.2
7	9932397	2019.4	72.5
8	9932397	1811.1	36.6
9	9932397	1360.0	45.8
	VES Station J112		
1	9933256	2205.9	80.7
2	9933256	2203.3	18.7
3	9933256	2198.9	493.7
4	9933256	2182.0	202.4
5	9933256	2139.2	10.6
6	9933256	1940.0	35.2
7	9933256	1932.0	64.8
	VES Station K94		
1	9934024	2139.0	14.9
2	9934024	2138.1	39.4
3	9934024	2134.1	6.1
4	9934024	2122.1	140.0
5	9934024	2089.3	9.5
6	9934024	1972.4	77.8
7	9934024	1673.9	5.5
8	9934024	1316.0	100.8
	VES Station R109		
1	9929077	2521.9	82.8
2	9929077	2517.3	1550.6
3	9929077	2510.9	87.9
4	9929077	2486.2	181.0

Traverse III-III′
VES Station R109

Layer	Nthg.(m)	Depth (m.a.s.l)	E.R (Ωm)
1	9929077	2432.8	7.1
2	9929077	2234.4	108.5
3	9929077	1863.0	7.5
	VES Station T130		
1	9928522	2523.7	313.3
2	9928522	2520.3	257.8
3	9928522	2514.2	304.7
4	9928522	2504.0	54.8
5	9928522	2477.8	13.9
6	9928522	2414.6	178.5
7	9928522	1907.6	7.0
8	9928522	1700.0	76.2

Traverse IV-IV′
VES Station G151

Layer	Est. (m)	Depth (m.a.s.l)	E.R (Ωm)
1	193735	2457.4	237.3
2	193735	2449.9	479.8
3	193735	2444.9	274.2
4	193735	2432.8	32.1
5	193735	2399.2	108.6
6	193735	2325.5	23.3
	193735	2186.0	33.4
	VES Station G143		
1	194121	2439.9	208.9
2	194121	2438.3	188.1
3	194121	2434.6	315.5
4	194121	2429.7	65.4
5	194121	2390.0	36.5
6	194121	2301.0	10.3
7	194121	2020.3	176.1
	194121	1893.0	36.2
	VES Station H112		
1	194604	2357.3	46.4
2	194604	2350.5	173.5
3	194604	2333.0	229.7
4	194604	2305.5	96.2
5	194604	2270.2	34.5
6	194604	2224.0	16.6
7	194604	1975.2	28.5
	194604	1424.0	16.4
	VES Station H104		
1	195074	2341.0	180.1
2	195074	2338.9	589.2
3	195074	2314.6	157.5
4	195074	2303.3	31.4
5	195074	2252.3	121.2
6	195074	1853.3	11.8
	195074	1243.0	15.9
	VES Station H102		
1	195540	2371.5	864.9
2	195540	2368.3	96.9
3	195540	2361.3	263.0
4	195540	2347.8	69.5
5	195540	2318.0	190.5
6	195540	2253.6	68.9
7	195540	2086.4	15.4
	195540	1550.0	37.9
	VES Station I78		
1	196426	2253.6	53.2
2	196426	2252.1	301.4
3	196426	2247.0	81.6
4	196426	2242.0	239.0
5	196426	2221.5	204.1
6	196426	2157.6	143.6
7	196426	2128.9	148.4
	196426	1870.0	40.3
	VES Station I74		
1	196935	2236.2	415.7
2	196935	2234.9	151.6
3	196935	2231.3	33.8
4	196935	2196.1	240.2
5	196935	2184.3	63.6
6	196935	2129.4	98.0
7	196935	1981.2	84.6
8	196935	1964.0	14.7

Modeled VES Data within Block A

VES Station O152

Layer	Est. (m)	Depth (m.a.s.l)	E.R (Ωm)
1	192151	1963	75.4
2	192151	1958	30.4
3	192151	1937	449.9
4	192151	1891	27.6
5	192151	1594	89.0
6	192151	1307	7.0

VES Station O144

Layer	Est. (m)	Depth (m.a.s.l)	E.R (Ωm)
1	192637	1963	1151.4
2	192637	1961	1608.1
3	192637	1945	153.9
4	192637	1871	214.9
5	192637	1663	45.2
6	192637	1304	451.7
7	192637	1140	20.8

VES Station O141

Layer	Est. (m)	Depth (m.a.s.l)	E.R (Ωm)
1	193075	1964	91.4
2	193075	1956	37.8
3	193075	1918	182.7
4	193075	1715	33.9
5	193075	1042	28.9
6	193075	1032	241.1

VES Station O135

Layer	Est. (m)	Depth (m.a.s.l)	E.R (Ωm)
1	193556	1944	91.4
2	193556	1940	208.6
3	193556	1916	93.2
4	193556	1872	27.6
5	193556	1559	14.0
6	193556	974	18.5
7	193556	846	27.9

VES Station O120

Layer	Est. (m)	Depth (m.a.s.l)	E.R (Ωm)
1	194107	1932	94.8
2	194107	1919	635.4
3	194107	1909	27.6
4	194107	1584	6.9
5	194107	1480	20.8
6	194107	1454	3.8
7	194107	1300	86.0

VES Station O116

Layer	Est. (m)	Depth (m.a.s.l)	E.R (Ωm)
1	194583	1950	18.0
2	194583	1948	3.4
3	194583	1938	152.0
4	194583	1930	29.1
5	194583	1803	20.2
6	194583	1401	28.3
7	194583	1401	182.7

VES Station O112

Layer	Est. (m)	Depth (m.a.s.l)	E.R (Ωm)
1	195057	1956	164.3
2	195057	1952	434.0
3	195057	1940	24.9
4	195057	1901	227.0
5	195057	1784	26.8
6	195057	1026	6.7
7	195057	857	100.0

VES Station O88

Layer	Est. (m)	Depth (m.a.s.l)	E.R (Ωm)
1	195536	1981	29.8
2	195536	1975	192.0
3	195536	1962	30.5
4	195536	1922	60.1
5	195536	1247	3.9
6	195536	1049	79.2

VES Station O96

Layer	Est. (m)	Depth (m.a.s.l)	E.R (Ωm)
1	196029	1981	483.6
2	196029	1978	4140.0
3	196029	1943	1239.6
4	196029	1777	19.5
5	196029	1418	5.4
6	196029	882	12.7

VES Station O95

Layer	Est. (m)	Depth (m.a.s.l)	E.R (Ωm)
1	196519	1969	59.7
2	196519	1964	2349.2
3	196519	1954	475.6
4	196519	1921	130.2

VES Station O95

Layer	Est. (m)	Depth (m.a.s.l)	E.R (Ωm)
1	196519	1699.8	43.6
2	196519	1492.4	23.7
3	196519	1420.0	11.5

VES Station O89

Layer	Est. (m)	Depth (m.a.s.l)	E.R (Ωm)
1	197069	2015.6	33.1
2	197069	2013.2	722.9
3	197069	2007.8	37.7
4	197069	1998.8	443.4
5	197069	1981.3	158.9
6	197069	1946.7	6.4
7	197069	1632.0	15.2
8	197069	1632.0	28.6

VES Station O80

Layer	Est. (m)	Depth (m.a.s.l)	E.R (Ωm)
1	197517	2024.9	34.4
2	197517	2010.9	555.1
3	197517	1980.6	12.3
4	197517	1851.8	44.8
5	197517	1604.0	7.7
6	197517	928.0	22.6

VES Station O73

Layer	Est. (m)	Depth (m.a.s.l)	E.R (Ωm)
1	197995	2005.5	25.1
2	197995	2004.0	148.6
3	197995	1999.8	32.9
4	197995	1987.5	318.9
5	197995	1951.3	16.4
6	197995	1849.0	174.2
7	197995	1036.8	10.7
8	197995	907.0	73.8

VES Station O64

Layer	Est. (m)	Depth (m.a.s.l)	E.R (Ωm)
1	198481	1993.9	9.1
2	198481	1986.8	36.3
3	198481	1951.4	285.8
4	198481	1810.3	74.0
5	198481	1657.8	164.0
6	198481	1025.6	1.6
7	198481	897.0	47.2

VES Station O56

Layer	Est. (m)	Depth (m.a.s.l)	E.R (Ωm)
1	198971	1972.5	37.8
2	198971	1969.8	16.3
3	198971	1965.5	19.7
4	198971	1950.4	1033.5
5	198971	1904.4	210.8
6	198971	1758.2	491.0
7	198971	874.0	17.5
8	198971	874.0	115.7

VES Station O48

Layer	Est. (m)	Depth (m.a.s.l)	E.R (Ωm)
1	199457	1990.0	9.5
2	199457	1988.3	26.4
3	199457	1983.1	8.8
4	199457	1975.9	37.3
5	199457	1928.0	242.7
6	199457	1869.6	116.1
7	199457	1448.9	13.5
8	199457	1167.0	9.5

VES Station M 182

Layer	Est. (m)	Depth (m.a.s.l)	E.R (Ωm)
1	194028	2004.0	538.3
2	194028	2002.2	1724.5
3	194028	1998.2	178.3
4	194028	1983.8	577.3
5	194028	1961.3	155.0
6	194028	1859.9	264.8
7	194028	1371.5	24.6
8	194028	1181.0	15.7

VES Station M 120

Layer	Est. (m)	Depth (m.a.s.l)	E.R (Ωm)
1	194516	2003.0	498.0
2	194516	1990.7	136.8
3	194516	1979.3	182.1
4	194516	1921.7	97.1
5	194516	1772.7	20.6
6	194516	1731.0	641.5

VES Station M114

Layer	Est. (m)	Depth (m.a.s.l)	E.R (Ωm)
1	194978	1997	185.0
2	194978	1993	529.2
3	194978	1937	25.2
4	194978	1831	66.9
5	194978	1613	5.1

VES Station M 109

Layer	Est. (m)	Depth (m.a.s.l)	E.R (Ωm)
1	195452	1999	172.9
2	195452	1994	670.4
3	195452	1988	41.4
4	195452	1971	204.7
5	195452	1922	20.0
6	195452	1815	115.8
7	195452	1452	20.0

VES Station M 103

Layer	Est. (m)	Depth (m.a.s.l)	E.R (Ωm)
1	195937	2006	174.4
2	195937	2003	31.1
3	195937	2000	161.8
4	195937	1995	88.3
5	195937	1982	12.3
6	195937	1938	130.0
7	195937	1825	13.3
8	195937	1733	88.9

VES Station M 96

Layer	Est. (m)	Depth (m.a.s.l)	E.R (Ωm)
1	196442	2035	502.8
2	196442	2028	83.3
3	196442	1967	37.2
4	196442	1891	7.6
5	196442	1747	71.1
6	196442	1487	7.5

VES Station M91

Layer	Est. (m)	Depth (m.a.s.l)	E.R (Ωm)
1	196924	2015	149.3
2	196924	2013	26.0
3	196924	2001	183.3
4	196924	1986	17.1
5	196924	1928	11.7
6	196924	1784	97.6
7	196924	1468	10.7

VES Station M 71

Layer	Est. (m)	Depth (m.a.s.l)	E.R (Ωm)
1	197399	2044	98.1
2	197399	2038	40.0
3	197399	2035	68.1
4	197399	2000	331.6
5	197399	1931	95.8
6	197399	1839	202.5
7	197399	1661	23.9

VES Station K117

Layer	Est. (m)	Depth (m.a.s.l)	E.R (Ωm)
1	193456	2238	1227.4
2	193456	2233	5293.7
3	193456	2094	337.3
4	193456	1855	12.2

VES Station K102

Layer	Est. (m)	Depth (m.a.s.l)	E.R (Ωm)
1	193987	2211	157.4
2	193987	2208	32.0
3	193987	2199	90.8
4	193987	2171	52.1
5	193987	2037	30.5
6	193987	1500	13.5
7	193987	1388	123.9

VES Station K99

Layer	Est. (m)	Depth (m.a.s.l)	E.R (Ωm)
1	194474	2186	156.2
2	194474	2185	532.5
3	194474	2181	669.3
4	194474	2171	395.0
5	194474	2129	22.0
6	194474	2051	48.2
7	194474	1809	9.7
8	194474	1638	538.3

Modeled VES Data within Block A Continued

VES Station 98

Layer	Est. (m)	Depth (m.a.s.l)	E.R (Ωm)
1	194945	2166.5	136.4
2	194945	2164.9	1087.8
3	194945	2160.2	466.6
4	194945	2147.8	43.1
5	194945	2103.1	77.0
6	194945	1897.2	22.7
7	194945	1420.1	10.3
8	194945	1343.0	14.7

VES Station K94

1	195421	2139.0	14.9
2	195421	2138.1	39.4
3	195421	2134.1	6.1
4	195421	2122.1	140.0
5	195421	2089.3	9.5
6	195421	1972.4	77.8
7	195421	1673.9	5.5
8	195421	1316.0	100.8

VES Station K90

1	195889	2170.7	63.3
2	195889	2168.6	36.3
3	195889	2162.9	198.9
4	195889	2148.4	56.3
5	195889	2121.6	124.7
6	195889	2069.7	92.0
7	195889	2035.6	32.8
8	195889	1701.2	6.5
9	195889	1074.0	37.3

VES Station K82

1	196314	2110.0	102.5
2	196314	2107.7	1155.3
3	196314	2102.8	23.1
4	196314	2071.7	62.0
5	196314	2034.0	118.5
6	196314	1990.2	60.9
7	196314	1725.2	7.2
8	196314	1577.6	14.9
9	196314	1011.0	994.8

VES Station K80

1	196801	2071.5	150.3
2	196801	2069.9	489.5
3	196801	2067.2	230.8
4	196801	2058.8	32.4
5	196801	1967.6	82.8
6	196801	1590.9	10.8
7	196801	1524.0	42.2

VES Station K78

1	197292	2067.6	184.0
2	197292	2066.1	382.5
3	197292	2057.7	121.0
4	197292	1984.8	25.8
5	197292	1885.0	40.6
6	197292	1491.2	5.6
7	197292	969.0	1082.6

VES Station K70

1	197781	2056.9	39.5
2	197781	2054.4	515.2
3	197781	2037.5	297.6
4	197781	1999.9	161.6
5	197781	1918.2	81.4
6	197781	1799.9	37.4
7	197781	1060.2	11.2
8	197781	958.0	20.0

VES Station K62

1	198281	2033.5	39.0
2	198281	2031.0	54.7
3	198281	2009.4	236.6
4	198281	1981.8	971.6
5	198281	1854.2	79.8
6	198281	1570.4	3214.3
7	198281	936.0	57.8

VES Station K54

Layer	Est. (m)	Depth (m.a.s.l)	E.R (Ωm)
1	198760	2067.4	8.9
2	198760	2059.6	47.4
3	198760	1945.7	439.8
4	198760	1739.5	30.3
5	198760	1380.1	108.4
6	198760	969.0	714.2

VES Station K46

1	199279	2037.6	18.0
2	199279	2034.5	32.6
3	199279	2027.8	77.5
4	199279	1958.6	398.8
5	199279	1763.7	23.4
6	199279	996.2	70.2
7	199279	940.0	39.6

VES Station K12

1	199775	2058.9	89.2
2	199775	2055.8	29.7
3	199775	2046.9	202.0
4	199775	2033.2	72.3
5	199775	2004.6	25.5
6	199775	1868.7	20.1
7	199775	1657.4	11.1
8	199775	1510.0	332.7

Modeled VES Data within Block B

VES Station I123

Layer	Est. (m)	Depth (m.a.s.l)	E.R (Ωm)
1	192816	2298	106.5
2	192816	2296	222.9
3	192816	2289	364.0
4	192816	2282	192.6
5	192816	2252	38.3
6	192816	2209	59.0
7	192816	2143	45.3
8	192816	1894	27.7
9	192816	1210	17.1
10	192816	1201	31.3

VES Station I112

Layer	Est. (m)	Depth (m.a.s.l)	E.R (Ωm)
1	193211	2365	233.9
2	193211	2362	308.5
3	193211	2356	514.1
4	193211	2345	30.0
5	193211	2321	116.4
6	193211	2301	40.5
7	193211	2179	25.5
8	193211	1817	29.3
9	193211	1817	184.2

VES Station I108

Layer	Est. (m)	Depth (m.a.s.l)	E.R (Ωm)
1	193641	2318	40.8
2	193641	2311	497.2
3	193641	2305	11.7
4	193641	2120	34.7
5	193641	1892	113.9
6	193641	1769	8.7

VES Station I102

Layer	Est. (m)	Depth (m.a.s.l)	E.R (Ωm)
1	194550	2253	619.4
2	194550	2250	2666.5
3	194550	2245	865.4
4	194550	2234	356.0
5	194550	2217	645.9
6	194550	2180	44.3
7	194550	2067	28.1
8	194550	1740	16.0
9	194550	1279	54.0
10	194550	1155	2.0

VES Station I95

Layer	Est. (m)	Depth (m.a.s.l)	E.R (Ωm)
1	195027	2243	931.5
2	195027	2242	212.5
3	195027	2238	678.6
4	195027	2229	28.0
5	195027	2207	82.1
6	195027	2110	36.0
7	195027	1933	18.1
8	195027	1539	60.4
9	195027	1145	104.9

VES Station I87

Layer	Est. (m)	Depth (m.a.s.l)	E.R (Ωm)
1	195490	2293	970.8
2	195490	2291	1324.1
3	195490	2280	732.6
4	195490	2263	543.0
5	195490	2256	116.1
6	195490	2197	53.2
7	195490	2019	72.5
8	195490	1811	36.6
9	195490	1360	45.8

VES Station I79

Layer	Est. (m)	Depth (m.a.s.l)	E.R (Ωm)
1	195961	2316	101.3
2	195961	2312	388.7
3	195961	2309	137.8
4	195961	2305	252.3
5	195961	2268	1415.8
6	195961	2230	32.0
7	195961	1965	105.1
8	195961	1492	35.1

VES Station I123

Layer	Est. (m)	Depth (m.a.s.l)	E.R (Ωm)
1	196426	2253.6	53.2
2	196426	2252.1	301.4
3	196426	2247.0	81.6
4	196426	2242.0	239.0
5	196426	2221.5	204.1
6	196426	2157.6	143.6
7	196426	2128.9	148.4
8	196426	1870.0	40.3

VES Station I74

Layer	Est. (m)	Depth (m.a.s.l)	E.R (Ωm)
1	196935	2236.2	415.7
2	196935	2234.9	151.6
3	196935	2231.3	33.8
4	196935	2196.1	240.2
5	196935	2184.3	63.6
6	196935	2129.4	98.0
7	196935	1981.2	84.6
8	196935	1964.0	14.7

VES Station H190

Layer	Est. (m)	Depth (m.a.s.l)	E.R (Ωm)
1	190931	2095.6	158.5
2	190931	2094.2	451.7
3	190931	2091.0	54.1
4	190931	2083.4	445.1
5	190931	2072.5	279.6
6	190931	2047.5	892.4
7	190931	2012.6	269.8
8	190931	1927.7	74.8
9	190931	1738.2	147.6
10	190931	1437.0	442.0

VES Station H175

Layer	Est. (m)	Depth (m.a.s.l)	E.R (Ωm)
1	191336	2107.0	401.2
2	191336	2097.8	1086.7
3	191336	2080.7	352.4
4	191336	2060.1	497.5
5	191336	2019.3	233.9
6	191336	1930.2	505.9
7	191336	1879.6	90.1
8	191336	1450.0	9.2

VES Station H162

Layer	Est. (m)	Depth (m.a.s.l)	E.R (Ωm)
1	191773	2145.2	81.0
2	191773	2141.0	55.2
3	191773	2119.3	23.8
4	191773	2100.1	58.3
5	191773	2049.9	10.6
6	191773	1980.6	106.2
7	191773	1830.2	7.0
8	191773	1097.1	18.0
9	191773	1048.0	10.6

VES Station H158

Layer	Est. (m)	Depth (m.a.s.l)	E.R (Ωm)
1	192147	2193.2	89.9
2	192147	2188.8	633.9
3	192147	2177.0	1809.7
4	192147	2164.8	23.9
5	192147	2086.1	80.2
6	192147	1979.4	7.7
7	192147	1096.0	19.8

VES Station H151

Layer	Est. (m)	Depth (m.a.s.l)	E.R (Ωm)
1	192537	2553.5	28.3
2	192537	2545.7	234.1
3	192537	2533.5	35.4
4	192537	2507.9	101.7
5	192537	2445.8	49.0
6	192537	2040.4	6.2
7	192537	1456.0	104.4

VES Station H142

Layer	Est. (m)	Depth (m.a.s.l)	E.R (Ωm)
1	192983	2366	161.6
2	192983	2362	258.0
3	192983	2355	119.2
4	192983	2345	189.5
5	192983	2302	42.0
6	192983	2255	117.7
7	192983	2179	48.1
8	192983	1951	7.8
9	192983	1269	33.2

VES Station H136

Layer	Est. (m)	Depth (m.a.s.l)	E.R (Ωm)
1	193401	2363	19.3
2	193401	2361	40.6
3	193401	2346	376.8
4	193401	2289	215.2
5	193401	1341	19.2
6	193401	1265	14.5

VES Station H123

Layer	Est. (m)	Depth (m.a.s.l)	E.R (Ωm)
1	193825	2355	340.6
2	193825	2352	559.3
3	193825	2349	430.3
4	193825	2338	514.2
5	193825	2324	1114.0
6	193825	2301	760.3
7	193825	2231	27.8
8	193825	2029	41.9
9	193825	1696	6.9

VES Station H120

Layer	Est. (m)	Depth (m.a.s.l)	E.R (Ωm)
1	194209	2368	295.4
2	194209	2367	863.4
3	194209	2362	507.7
4	194209	2357	1178.1
5	194209	2345	132.5
6	194209	2312	389.0
7	194209	2210	10.6
8	194209	2019	62.2
9	194209	1269	8.5

VES Station H1112

Layer	Est. (m)	Depth (m.a.s.l)	E.R (Ωm)
1	194604	2357	46.4
2	194604	2350	173.5
3	194604	2333	229.7
4	194604	2305	96.2
5	194604	2270	34.5
6	194604	2224	16.6
7	194604	1975	28.5
8	194604	1424	16.4

VES Station H104

Layer	Est. (m)	Depth (m.a.s.l)	E.R (Ωm)
1	195074	2341	180.1
2	195074	2339	589.2
3	195074	2315	157.5
4	195074	2303	31.4
5	195074	2252	121.2
6	195074	1853	11.8
7	195074	1243	15.9

VES Station H102

Layer	Est. (m)	Depth (m.a.s.l)	E.R (Ωm)
1	195540	2374	58.3
2	195540	2371	864.9
3	195540	2368	96.9
4	195540	2361	263.0
5	195540	2348	69.5
6	195540	2318	190.5
7	195540	2254	68.9
8	195540	2086	15.4
9	195540	1550	37.9

VES Station H94

Layer	Est. (m)	Depth (m.a.s.l)	E.R (Ωm)
1	195987	2371	1827.0
2	195987	2369	165.2
3	195987	2365	495.2
4	195987	2356	39.9
5	195987	2310	195.7
6	195987	2091	10.0

Modeled VES Data within Block B Continued

Layer	Est. (m)	Depth (m.a.s.l)	E.R (Ωm)
		VES Station K94	
1	195987	1363.9	162.8
2	195987	1273.0	10.3
		VES Station K92	
1	196333	2341.5	612.2
2	196333	2331.6	258.1
3	196333	2318.2	82.4
4	196333	2292.1	186.0
5	196333	2282.0	45.5
6	196333	2230.5	33.0
7	196333	2054.7	41.5
8	196333	1793.0	23.8
		VES Station K88	
1	196697	2343.7	125.9
2	196697	2339.2	38.7
3	196697	2316.1	55.2
4	196697	2290.3	19.3
5	196697	2249.3	101.7
6	196697	2132.3	16.6
7	196697	1699.1	27.0
8	196697	1520.0	45.2
		VES Station K80	
1	197197	2311.3	308.6
2	197197	2309.2	124.6
3	197197	2306.6	652.9
4	197197	2296.0	829.3
5	197197	2202.3	28.0
6	197197	1603.9	49.0
7	197197	1217.0	11.1
		VES Station K72	
1	197689	2301.5	118.2
2	197689	2291.6	344.5
3	197689	2286.3	118.7
4	197689	2268.3	24.0
5	197689	2217.4	54.4
6	197689	2041.1	16.0
7	197689	1735.2	17.9
8	197689	1203.0	31.5
		VES Station K64	
1	198189	2282.7	52.2
2	198189	2279.9	30.2
3	198189	2278.4	71.3
4	198189	2274.9	960.5
5	198189	2243.5	457.2
6	198189	2182.4	289.5
7	198189	1895.4	22.2
8	198189	1184.0	100.4
		VES Station K56	
1	198672	2300.4	37.3
2	198672	2265.7	1305.0
3	198672	2059.2	6.1
4	198672	1827.0	329.7
5	198672	1207.0	2.0
6	198672	1207.0	45.0
		VES Station K48	
1	199186	2239.8	164.0
2	199186	2236.8	1165.3
3	199186	2230.8	203.2
4	199186	2221.9	441.3
5	199186	2184.7	190.0
6	199186	2113.1	801.1
7	199186	1665.5	39.9
8	199186	1307.0	68.0
		VES Station K40	
1	199648	2237.2	108.6
2	199648	2233.6	42.3
3	199648	2213.4	127.1
4	199648	2154.0	343.6
5	199648	2013.5	104.8
6	199648	1534.8	252.2
7	199648	1414.0	15.4

Layer	Est. (m)	Depth (m.a.s.l)	E.R (Ωm)
		VES Station G151	
1	193735	2457.4	237.3
2	193735	2449.9	479.8
3	193735	2444.9	274.2
4	193735	2432.8	32.1
5	193735	2399.2	108.6
6	193735	2325.5	23.3
7	193735	2186.0	33.4
		VES Station G143	
1	194121	2439.9	208.9
2	194121	2438.3	188.1
3	194121	2434.6	315.5
4	194121	2429.7	65.4
5	194121	2390.0	36.5
6	194121	2301.0	10.3
7	194121	2020.3	176.1
8	194121	1893.0	36.2
		VES Station G136	
1	194597	2437.8	426.0
2	194597	2434.2	1864.1
3	194597	2425.4	902.1
4	194597	2399.0	99.5
5	194597	2265.8	43.5
6	194597	1889.0	13.5
		VES Station G124	
1	195039	2405.8	229.1
2	195039	2403.3	2551.0
3	195039	2396.8	276.2
4	195039	2371.8	912.4
5	195039	2303.9	9.6
6	195039	2022.1	88.1
7	195039	1747.0	11.7
		VES Station G120	
1	195558	2435.6	633.1
2	195558	2428.0	1126.8
3	195558	2409.7	1868.6
4	195558	2361.1	201.5
5	195558	2262.9	13.7
6	195558	2115.6	88.6
7	195558	1612.0	20.0

Modeled VES Data within Block C

VES Station A6

Layer	Est. (m)	Depth (m.a.s.l)	E.R (Ωm)
1	197382	2347	44.8
2	197382	2342	28.5
3	197382	2322	14.0
4	197382	2215	22.4
5	197382	1912	15.2
6	197382	1250	26.5
7	197382	1250	51.8

VES Station A13

1	196873	2382	124.4
2	196873	2380	39.4
3	196873	2369	335.9
4	196873	2316	11.6
5	196873	2070	27.9
6	196873	1834	13.2

VES Station A21

1	196367	2421	173.9
2	196367	2412	58.0
3	196367	2392	17.0
4	196367	2309	35.5
5	196367	2126	8.9
6	196367	1765	32.9

VES Station A32

1	195867	2519	729.8
2	195867	2514	1498.7
3	195867	2496	570.8
4	195867	2412	46.3
5	195867	2237	6.1
6	195867	1864	100.4

VES Station A40

1	195376	2594	301.0
2	195376	2591	429.2
3	195376	2541	118.4
4	195376	2360	15.4
5	195376	2098	26.8
6	195376	2046	14.1

VES Station A48

1	194603	2581	447.1
2	194603	2574	885.4
3	194603	2560	1723.0
4	194603	2532	743.1
5	194603	2414	22.4
6	194603	2227	4.3
7	194603	1924	33.4

VES Station A56

1	194604	2582	463.3
2	194604	2582	2202.3
3	194604	2579	917.0
4	194604	2570	2489.9
5	194604	2560	667.2
6	194604	2528	998.2
7	194604	2427	88.9
8	194604	2085	18.3
9	194604	1924	272.1

VES Station A74

1	194181	2628	39.0
2	194181	2624	169.7
3	194181	2616	635.6
4	194181	2598	249.2
5	194181	2506	73.3
6	194181	2245	19.9

VES Station A81

1	193643	2693	57.9
2	193643	2691	174.7
3	193643	2685	536.6
4	193643	2679	188.8
5	193643	2667	42.9
6	193643	2605	110.9
7	193643	2449	9.6
8	193643	2310	136.8

VES Station A86

Layer	Est. (m)	Depth (m.a.s.l)	E.R (Ωm)
1	193165	2708.3	29.2
2	193165	2706.7	24.8
3	193165	2704.7	40.6
4	193165	2697.7	106.1
5	193165	2682.6	71.4
6	193165	2665.4	39.9
7	193165	2548.1	27.8
8	193165	2085.6	23.0
9	193165	2050.0	34.0

VES Station A93

1	192682	2624.0	20.5
2	192682	2621.9	5.4
3	192682	2618.6	29.4
4	192682	2610.6	105.2
5	192682	2575.5	22.3
6	192682	2530.1	108.1
7	192682	2440.1	38.0
8	192682	2089.0	18.9
9	192682	1691.0	76.6

VES Station A102

1	192206	2758.5	239.3
2	192206	2757.4	22.1
3	192206	2755.2	34.2
4	192206	2748.5	137.6
5	192206	2742.2	76.6
6	192206	2687.5	49.4
7	192206	2628.3	30.8
8	192206	2376.8	13.6
9	192206	1935.0	241.1

VES Station C87

1	197553	2358.7	45.1
2	197553	2358.5	173.7
3	197553	2357.7	536.6
4	197553	2354.3	253.2
5	197553	2336.7	1210.5
6	197553	2284.5	101.2
7	197553	2198.2	44.2
8	197553	1975.0	23.5

VES Station C95

1	197062	2380.7	37.0
2	197062	2377.3	201.0
3	197062	2365.5	51.7
4	197062	2365.5	149.0
5	197062	2347.3	414.5
6	197062	2310.9	6.0
7	197062	2142.3	19.3
8	197062	1825.0	62.4
9	197062	382.0	12.4

VES Station C99

1	196592	2424.7	15.4
2	196592	2412.6	60.5
3	196592	2333.2	12.3
4	196592	2197.5	205.3
5	196592	2084.7	21.6
6	196592	1885.5	53.7
7	196592	1430.0	177.4

VES Station C105

1	196094	2480.0	1050.9
2	196094	2474.9	1318.0
3	196094	2454.0	188.6
4	196094	2345.8	39.0
5	196094	2109.5	7.9
6	196094	1283.0	840.1

VES Station C116

Layer	Est. (m)	Depth (m.a.s.l)	E.R (Ωm)
1	195589	2645	100.9
2	195589	2643	11.7
3	195589	2640	75.7
4	195589	2636	36.3
5	195589	2625	4.6
6	195589	2607	7.0
7	195589	2563	27.7
8	195589	2489	8.1
9	195589	1854	464.6
10	195589	647	105.1

VES Station C123

1	195111	2600	260.5
2	195111	2599	424.7
3	195111	2596	55.4
4	195111	2591	107.0
5	195111	2581	159.8
6	195111	2557	79.5
7	195111	2517	7.7
8	195111	2435	38.7
9	195111	2286	20.4
10	195111	2014	13.2
11	195111	1615	71.3
12	195111	603	7.6

VES Station C130

1	194622	2591	54.9
2	194622	2589	96.3
3	194622	2581	139.6
4	194622	2573	12.5
5	194622	2455	19.2
6	194622	2324	10.2
7	194622	1897	15.9

VES Station C138

1	194133	2640	95.2
2	194133	2637	32.0
3	194133	2625	225.1
4	194133	2597	17.9
5	194133	2548	42.3
6	194133	2367	11.3
7	194133	2150	35.4
8	194133	1141	17.3

VES Station C144

1	193673	2659	457.1
2	193673	2657	1243.3
3	193673	2653	616.9
4	193673	2646	65.8
5	193673	2638	106.2
6	193673	2615	201.1
7	193673	2561	58.5
8	193673	2357	18.1
9	193673	1962	33.5
10	193673	1162	14.9

VES Station C158

1	193182	2667	165.6
2	193182	2664	1796.4
3	193182	2659	149.6
4	193182	2641	637.8
5	193182	2568	5.0
6	193182	2427	205.5
7	193182	1668	12.3

VES Station C165

1	192726	2741	264.2
2	192726	2739	493.4
3	192726	2733	3534.7
4	192726	2724	371.5
5	192726	2705	2445.4
6	192726	2526	13.7
7	192726	2043	1756.8

Modeled VES Data within Block C Continued

Layer	Est. (m)	Depth (m.a.s.l)	E.R (Ωm)
		VES Station R76	
1	197477	2380.0	11.4
2	197477	2373.4	2031.0
3	197477	2367.7	8.5
4	197477	2242.3	63.7
5	197477	1831.0	23.0
		VES Station R88	
1	197034	2434.2	175.9
2	197034	2428.4	25.4
3	197034	2405.7	159.8
4	197034	2333.9	52.1
5	197034	2052.3	21.9
6	197034	1887.0	44.5
		VES Station R94	
1	196001	2483.3	20.6
2	196001	2480.7	9.9
3	196001	2461.9	339.8
4	196001	2391.4	5.4
5	196001	2259.8	86.2
6	196001	1385.0	31.4
		VES Station R103	
1	196121	2476.2	317.9
2	196121	2469.9	3764.4
3	196121	2462.7	77.1
4	196121	2429.3	215.5
5	196121	2349.1	5.9
6	196121	2114.4	44.4
7	196121	1378.0	23.9
		VES Station R109	
1	195667	2521.9	82.8
2	195667	2517.3	1550.6
3	195667	2510.9	87.9
4	195667	2486.2	181.0
5	195667	2432.8	7.1
6	195667	2234.4	108.5
7	195667	1863.0	7.5
		VES Station R117	
1	195152	2593.1	247.8
2	195152	2591.9	5556.7
3	195152	2585.8	2391.1
4	195152	2515.0	124.6
5	195152	2426.3	9.5
6	195152	1884.0	171.5
7	195152	1495.0	1016.3
		VES Station R126	
1	194682	2560.8	86.4
2	194682	2559.0	515.3
3	194682	2557.1	154.9
4	194682	2549.7	5.5
5	194682	2534.3	9.3
6	194682	2455.1	18.8
7	194682	2239.5	23.4
8	194682	1584.5	12.2
R126	194682	1462.0	56.6
		VES Station R134	
1	194282	2577.6	161.3
2	194282	2568.9	44.2
3	194282	2547.4	19.8
4	194282	2398.2	29.6
5	194282	2056.5	11.9
6	194282	1646.0	33.7
		VES Station R142	
1	193679	2597.6	1070.2
2	193679	2593.3	335.7
3	193679	2585.3	30.7
4	193679	2564.6	90.8
5	193679	2538.4	26.7
6	193679	2473.5	3.1
7	193679	2358.7	157.2
8	193679	1993.8	3.4
9	193679	1939.0	250.3

Layer	Est. (m)	Depth (m.a.s.l)	E.R (Ωm)
		VES Station R150	
1	193201	2613.5	897.0
2	193201	2613.0	45.6
3	193201	2598.0	1001.4
4	193201	2587.7	94.2
5	193201	2525.2	47.8
6	193201	2403.5	6.2
7	193201	1735.0	100.0
8	193201	1625.0	5.0
9	193201	1514.0	58.0
	Others		
		VES Station D57	
Layer	**Est. (m)**	**Nthg. (m)**	**E.R (Ωm)**
1	197955	9928895.0	66.5
2	197955	9928895.0	791.9
3	197955	9928895.0	236.7
4	197955	9928895.0	10.2
5	197955	9928895.0	87.7
		VES Station D63	
1	197528	9929109.0	35.2
2	197528	9929109.0	632.1
3	197528	9929109.0	336.4
4	197528	9929109.0	16.5
5	197528	9929109.0	378.8
6	197528	9929109.0	407.9
		VES Station D25	
1	197081	9929323.0	16.3
2	197081	9929323.0	1404.7
3	197081	9929323.0	261.3
4	197081	9929323.0	28.0
5	197081	9929323.0	102.3
6	197081	9929323.0	15.3
		VES Station D78	
1	196602	9929513.0	34.3
2	196602	9929513.0	99.9
3	196602	9929513.0	156.5
4	196602	9929513.0	598.7
5	196602	9929513.0	323.8
6	196602	9929513.0	86.7
7	196602	9929513.0	21.7
8	196602	9929513.0	101.1
9	196602	9929513.0	19.7
10	196602	9929513.0	183.6
		VES Station D85	
1	196092	9929620.0	69.4
2	196092	9929620.0	1371.5
3	196092	9929620.0	6.1
4	196092	9929620.0	525.5
5	196092	9929620.0	3.1
6	196092	9929620.0	71.5
		VES Station D89	
1	195615	9929563.0	36.1
2	195615	9929563.0	219.1
3	195615	9929563.0	352.2
4	195615	9929563.0	14.6
5	195615	9929563.0	81.0
6	195615	9929563.0	8.8
7	195615	9929563.0	785.5
		VES Station D95	
1	195125	9929534.0	37.4
2	195125	9929534.0	140.7
3	195125	9929534.0	18.8
4	195125	9929534.0	46.6
5	195125	9929534.0	20.1
6	195125	9929534.0	16.8
7	195125	9929534.0	12.7
		VES Station D102	
1	194638	9929510.0	1454.2
2	194638	9929510.0	522.6
3	194638	9929510.0	154.3
4	194638	9929510.0	108.1
5	194638	9929510.0	299.3
6	194638	9929510.0	101.0
7	194638	9929510.0	33.2
8	194638	9929510.0	20.3
9	194638	9929510.0	187.8

Other Modeled VES Data within the Study Area

Layer	Est. (m)	Nthg. (m)	E.R (Ωm)
	VES Station D112		
1	194160	9929502	497.0
2	194160	9929502	2635.4
3	194160	9929502	206.7
4	194160	9929502	998.6
5	194160	9929502	36.5
6	194160	9929502	295.6
7	194160	9929502	7.3
8	194160	9929502	13.4
9	194160	9929502	242.4
	VES Station D120		
1	193779	9929482	1010.3
2	193779	9929482	54.5
3	193779	9929482	243.4
4	193779	9929482	1.2
5	193779	9929482	3.5
6	193779	9929482	121.5
	VES Station E109		
1	194063	9930391	206.7
2	194063	9930391	155.4
3	194063	9930391	381.5
4	194063	9930391	35.9
5	194063	9930391	108.1
6	194063	9930391	50.7
7	194063	9930391	29.4
8	194063	9930391	37.7
	VES Station E120		
1	194583	9930397	134.0
2	194583	9930397	428.4
3	194583	9930397	619.0
4	194583	9930397	6.0
5	194583	9930397	103.5
6	194583	9930397	4.6
7	194583	9930397	448.2
	VES Station E130		
1	195061	9930389	251.6
2	195061	9930389	125.6
3	195061	9930389	433.8
4	195061	9930389	82.3
5	195061	9930389	528.9
6	195061	9930389	9.7
	VES Station F144		
1	196553	9930512	234.9
2	196553	9930512	454.4
3	196553	9930512	114.1
4	196553	9930512	84.7
5	196553	9930512	29.3
6	196553	9930512	10.9
	VES Station F135		
1	197027	9930550	288.0
2	197027	9930550	80.4
3	197027	9930550	628.2
4	197027	9930550	426.3
5	197027	9930550	81.7
6	197027	9930550	386.1
7	197027	9930550	3.0
	VES Station F126		
1	197501	9930640	1181.5
2	197501	9930640	390.3
3	197501	9930640	5005.0
4	197501	9930640	1709.8
5	197501	9930640	41.5
6	197501	9930640	4282.7
	VES Station J120		
1	195003	9933279	63.7
2	195003	9933279	44.9
3	195003	9933279	360.8
4	195003	9933279	203.3
5	195003	9933279	131.8
6	195003	9933279	21.8
7	195003	9933279	28.9

		VES Station J112	
1	195483	9933256.0	80.7
2	195483	9933256.0	18.7
3	195483	9933256.0	493.7
4	195483	9933256.0	202.4
5	195483	9933256.0	10.6
6	195483	9933256.0	35.2
7	195483	9933256.0	64.8
		VES Station L108	
1	196448	9934745.0	61.1
2	196448	9934745.0	86.2
3	196448	9934745.0	56.9
4	196448	9934745.0	249.8
5	196448	9934745.0	65.9
6	196448	9934745.0	105.9
7	196448	9934745.0	32.1
		VES Station L99	
1	196929	9934820.0	183.3
2	196929	9934820.0	56.1
3	196929	9934820.0	37.2
4	196929	9934820.0	185.9
5	196929	9934820.0	11.0
6	196929	9934820.0	83.8
7	196929	9934820.0	4.4
		VES Station L74	
1	197444	9934866.0	82.9
2	197444	9934866.0	125.0
3	197444	9934866.0	2791.2
4	197444	9934866.0	49.0
5	197444	9934866.0	163.7
6	197444	9934866.0	126.7
		VES Station P116	
1	194581	9936189.0	24.4
2	194581	9936189.0	14.0
3	194581	9936189.0	47.3
4	194581	9936189.0	668.4
5	194581	9936189.0	8.1
6	194581	9936189.0	26.7
		VES Station P110	
1	195066	9936271.0	219.2
2	195066	9936271.0	59.6
3	195066	9936271.0	140.3
4	195066	9936271.0	960.0
5	195066	9936271.0	533.2
6	195066	9936271.0	15.8
7	195066	9936271.0	73.5
8	195066	9936271.0	2.5
		VES Station P100	
1	195544	9936351.0	159.6
2	195544	9936351.0	1375.5
3	195544	9936351.0	442.1
4	195544	9936351.0	343.8
5	195544	9936351.0	35.3
6	195544	9936351.0	46.2
7	195544	9936351.0	12.5
8	195544	9936351.0	19.6
		VES Station P95	
1	196027	9936441.0	220.4
2	196027	9936441.0	16581.5
3	196027	9936441.0	620.8
4	196027	9936441.0	2900.8
5	196027	9936441.0	40.2
6	196027	9936441.0	21.6
		VES Station P85	
1	196510	9936560.0	128.5
2	196510	9936560.0	3192.8
3	196510	9936560.0	1320.7
4	196510	9936560.0	90.1
5	196510	9936560.0	1006.1
		VES Station Q119	
1	194592	9936509.0	17.7
2	194592	9936509.0	149.1
3	194592	9936509.0	64.3
4	194592	9936509.0	32.5
5	194592	9936509.0	80.7
6	194592	9936509.0	23.1
7	194592	9936509.0	8.7
8	194592	9936509.0	19.6

Layer	Est. (m)	Nthg. (m)	E.R (Ωm)
	VES Station Q114		
1	195065	9936581	191.4
2	195065	9936581	1206.2
3	195065	9936581	635.2
4	195065	9936581	347.0
5	195065	9936581	897.5
6	195065	9936581	517.3
7	195065	9936581	70.0
8	195065	9936581	97.1
9	195065	9936581	17.0
	VES Station Q104		
1	195583	9936677	884.8
2	195583	9936677	581.9
3	195583	9936677	861.8
4	195583	9936677	5386.0
5	195583	9936677	827.0
6	195583	9936677	75.8
7	195583	9936677	9.0
8	195583	9936677	217.5
	VES Station Q94		
1	196070	9936771	557.3
2	196070	9936771	4437.3
3	196070	9936771	835.4
4	196070	9936771	8042.7
5	196070	9936771	3820.2
6	196070	9936771	77.5
7	196070	9936771	17.4
8	196070	9936771	34.1
9	196070	9936771	506.6
10	196070	9936771	1000.0
	VES Station Q86		
1	196549	9936880	64.6
2	196549	9936880	40.4
3	196549	9936880	32.1
4	196549	9936880	9.0
5	196549	9936880	132.4
6	196549	9936880	26.4
7	196549	9936880	2.1
	VES Station T130		
1	195581	9928522	313.3
2	195581	9928522	257.8
3	195581	9928522	304.7
4	195581	9928522	54.8
5	195581	9928522	13.9
6	195581	9928522	178.5
7	195581	9928522	7.0
8	195581	9928522	76.2
	VES Station T137		
1	195184	9928757	60.6
2	195184	9928757	314.1
3	195184	9928757	75.7
4	195184	9928757	301.8
5	195184	9928757	19.9
6	195184	9928757	121.3
7	195184	9928757	11.9
8	195184	9928757	145.4
	VES Station T145		
1	194686	9928879	476.0
2	194686	9928879	34.3
3	194686	9928879	700.4
4	194686	9928879	59.0
5	194686	9928879	27.1
6	194686	9928879	64.6
7	194686	9928879	5.1
8	194686	9928879	71.8

Appendix 3: Hydrological Condition around L. Naivasha (Adapted from Reta, 2011)

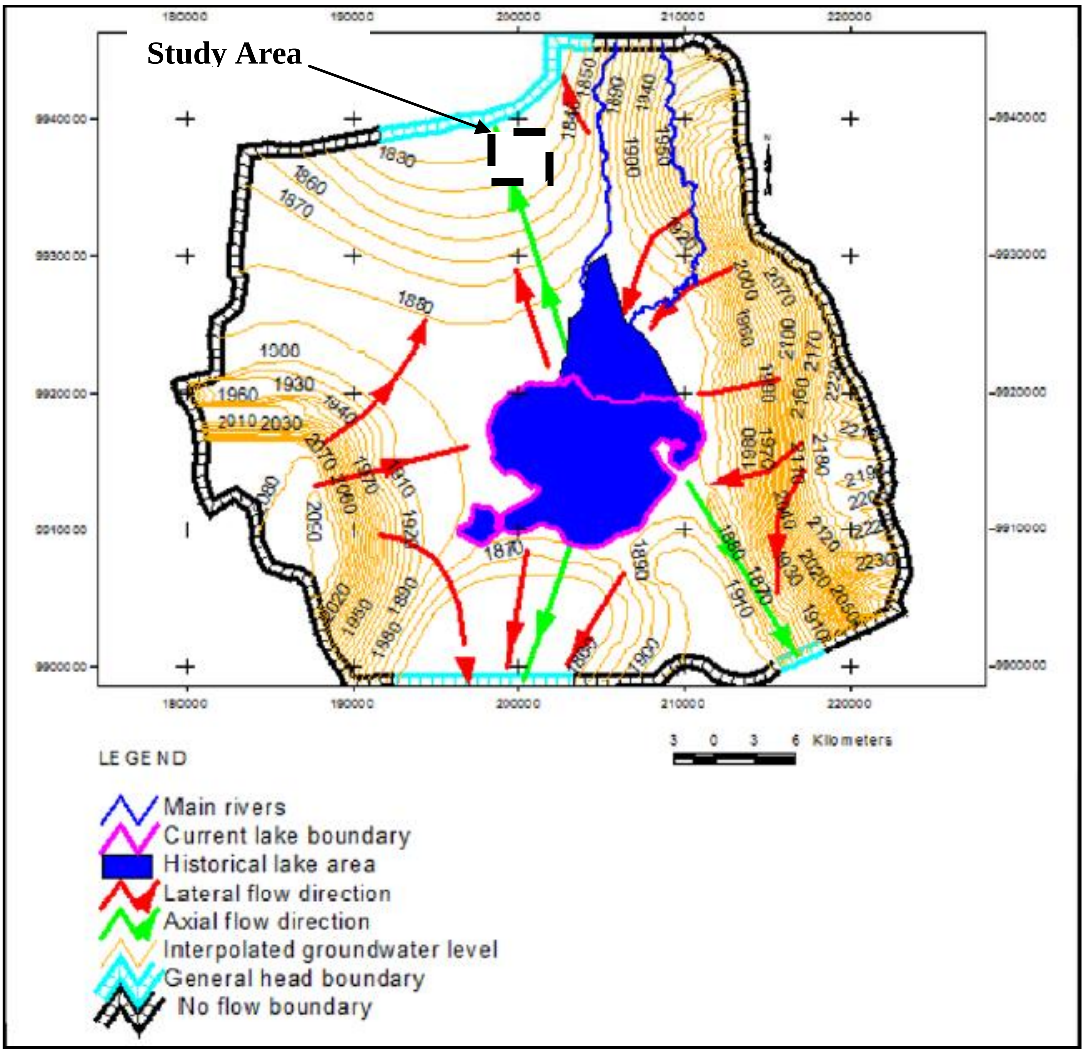

Appendix 4: Eburru Geological Well Log Data (KENGEN, 1990)

EW-01

Top	Bottom (m)	Soil Code	Rock type	Depth (m)
0	282	4	Pyroclastic	282
282	325	2	Trachyte	43
325	344	4	Pyroclastic	19
344	930	0	Loss of Circulation	586
930	1527	3	Rhyolite	597
1527	1547	2	Trachyte	20
1547	1643	1	Basalt	96
1643	1673	3	Rhyolite	30
1673	1695	1	Basalt	22
1695	1717	3	Rhyolite	22
1717	1767	2	Trachyte	50
1767	1807	3	Rhyolite	40
1807	1951	1	Basalt	144
1951	1969	3	Rhyolite	18
1969	2019	1	Basalt	50
2019	2049	5	Tuff	30
2049	2093	1	Basalt	44
2093	2185	3	Rhyolite	92
2185	2228	1	Basalt	43
2228	2466	0	Loss of Circulation	238

EW-02

Top	Bottom(m)	Depth m)	Soil Code	Rock type
0	42	42	4	Pyroclastic
42	72	30	2	Trachyte
72	91	19	5	Tuff
91	215	124		Comendite
215	243	28	5	Tuff
243	311	68	3	Rhyolite
311	421	110	5	Tuff
421	427	6	3	Rhyolite
427	461	34	5	Tuff
461	635	174	3	Rhyolite
635	699	64	2	Trachyte
699	727	28	5	Tuff
727	823	96	3	Rhyolite
823	913	90	2	Trachyte
913	988	75	5	Tuff
988	1155	167	2	Trachyte
1155	1493	338	3	Rhyolite
1493	1549	56	2	Trachyte
1549	1621	72	5	Tuff
1621	1625	4	1	Basalt
1625	1671	46	3	Rhyolite
1671	1677	6	2	Trachyte
1677	2083	406	3	Rhyolite
2083	2350	267	2	Trachyte
2350	2365	15	1	Basalt
2365	2536	171	3	Rhyolite
2536	2560	24	1	Basalt
2560	2575	15	3	Rhyolite
2575	2608	33	1	Basalt
2608	2636	28	2	Trachyte
2636	2791	155		Granite

EW-03

Top	Bottom	Depth(m)	Soil Code	Rock type
0	56	56	4	Pyroclastic
56	74	18	3	Rhyolite
74	204	130	4	Pyroclastic
204	298	94	3	Rhyolite
298	424	126	2	Trachyte
424	470	46	0	Loss of Circulation
470	600	130	5	Tuff
600	676	76	2	Trachyte
676	774	98	-999	no information
774	794	20	0	Loss of Circulation
794	860	66	2	Trachyte
860	940	80	5	Tuff
940	1018	78	0	Loss of Circulation
1018	2580	1562	2	Trachyte

EW-04

Top	Bottom	Depth(m)	Soil Code	Rock type
0	198	198	4	Pyroclastic
198	200	2	2	Trachyte
200	352	152	0	Loss of Circulation
352	410	58	5	Tuff
410	422	12	2	Trachyte
422	572	150	5	Tuff
572	602	30	2	Trachyte
602	656	54	5	Tuff
656	720	64	2	Trachyte
720	850	130	5	Tuff
850	1732	882	2	Trachyte
1732	1848	116		Syenite
1848	1858	10	0	Loss of Circulation
1858	2002	144		Syenite
2002	2036	34	5	Tuff
2036	2104	68	3	Rhyolite
2104	2330	226		Syenite
2330	2380	50	2	Trachyte
2380	2400	20		Syenite
2400	2442	42	5	Tuff

Eburru Geological Well Log Data Continued

EW-05

Top (m)	Bottom(m)	Depth (m)	Soil Code	Rock type
0	52	52	4	Pyroclastic
52	68	16	3	Rhyolite
68	82	14	4	Pyroclastic
82	88	6	3	Rhyolite
88	104	16	0	Loss of Circulation
104	128	24	3	Rhyolite
128	144	16	2	Trachyte
144	238	94	3	Rhyolite
238	384	146	5	Tuff
384	397	13	3	Rhyolite
397	544	147	5	Tuff
544	645	101	2	Trachyte
645	654	9	3	Rhyolite
654	688	34	2	Trachyte
688	1206	518	3	Rhyolite
1206	1296	90	1	Basalt
1296	1394	98	2	Trachyte
1394	1502	108	3	Rhyolite
1502	1532	30	1	Basalt
1532	1556	24	3	Rhyolite
1556	1578	22	2	Trachyte
1578	1592	14	3	Rhyolite
1592	1608	16	2	Trachyte
1608	1670	62	3	Rhyolite
1670	1692	22	5	Tuff
1692	1744	52	3	Rhyolite
1744	1772	28	1	Basalt
1772	1790	18	5	Tuff
1790	1892	102	1	Basalt
1892	1940	48	2	Trachyte
1940	1980	40	1	Basalt
1980	1994	14	3	Rhyolite
1994	2090	96		Syenite
2090	2150	60	3	Rhyolite
2150	2221	71		Syenite

EW-06

Top(m)	Bottom(m)	Depth (m)	Soil Code	Rock type
0	114	114	3	Rhyolite
114	143	29	5	Tuff
143	194	51	3	Rhyolite
194	252	58	5	Tuff
252	274	22	3	Rhyolite
274	336	62	2	Trachyte
336	342	6	3	Rhyolite
342	386	44	0	Loss of Circulation
386	414	28	3	Rhyolite
414	488	74	0	Loss of Circulation
488	516	28	5	Tuff
516	562	46	3	Rhyolite
562	602	40	5	Tuff
602	655	53	3	Rhyolite
655	782	127	5	Tuff
782	1014	232	3	Rhyolite
1014	1030	16	0	Loss of Circulation
1030	1126	96	3	Rhyolite
1126	1168	42	0	Loss of Circulation
1168	1196	28	3	Rhyolite
1196	1222	26	0	Loss of Circulation
1222	1244	22	3	Rhyolite
1244	2486	1242	0	Loss of Circulation

Appendix 5: Piezometric Data for the Larger Nakuru County (Courtesy of Water Resource Management Authority)

BH-No.	DLONG.	DLAT.	ALT. (m)	W.R.L(m)	BH-No	DLONG.	DLAT.	ALT.(m)	W.R.L(m)
C-2346	35.8833	-0.1833	1920	14	C-9358	36.1667	-0.2964	1900	162
C-2360	36.2167	0.1333	1707	43	C-10764	36.1303	-0.3056	1910	136
C-2394	36.15	-0.15	2097	74	C-2636	36.4	-0.8	1887	5
C-2397	36.15	-0.1667	1998	88	C-4057	36.4	-0.8	250	3
C-4489	36.0833	0.1333	2030	12	C-2063	36.5833	-0.8167	2682	99
C-4494	36.15	-0.1333	2081	40	C-2420	36.6	-0.85	2644	68
C-4496	36.1667	-0.1167	2172	25	C-2421	36.6167	-0.8333	2636	21.3
C-4817	36.1333	-0.0833	1920	145	C-2663	36.5833	-0.8167	2658	98
C-2674	36.15	-0.1833	2109	73	C-1926	36.3833	-0.85	1981	91
C-4389	36.15	-0.1333	2030	12	C-9441	36.1181	0.2042	1960	69
C-10813	36.1342	-0.2944	1880	69.2	C-4555	36.3333	-0.5667	1830	28
C-10812	36.1811	0.3417	1900	121.1	C-9342	36.5292	0.7633	2150	149
C-3136	36.25	-0.4	2333	46	C-9353	36.4739	0.7667	2095	185
C-10714	36.2083	0.05	2012	14.4	C-1867	35.7667	-0.2167	2118	158
C-1325	35.8333	-0.2833	2255	90	C-3327	36	-0.6	2835	69
C-2099	35.8	-0.2333	2164	84	C-3353	35.9833	-0.6667	2804	45
C-2281	35.8	-0.25	2195	76	C-3650	35.9833	-0.65	2819	8
C-3005	35.8	-0.3	2423	38	C-6056	36.95	-0.6667	2790	14
C-3925	35.8	-0.25	2276	94	C-8473	35.9667	-0.6333	2730	96
C-3955	35.75	-0.25	2270	3	C-2496	35.9667	-0.6667	2740	144
C-1798	36.1333	-0.5333	1936	134	C-2157	35.7167	-0.15	2636	174
C-1913	36	-0.65	2987	40	C-2323	35.6833	-0.1167	2682	76
C-1914	35.9833	-0.6667	2896	23	C-2366	35.6833	-0.0833	2621	91
C-2118	36.25	-0.3667	2210	151	C-3130	35.6167	-0.167	2591	187
C-2289	36.1	-0.5833	2070	88	C-2428	35.7	-0.1667	2575	53
C-2480	36.1333	-0.4667	1830	40	C-2832	35.6667	-0.2	1920	34
C-4564	36.0833	-0.5	1850	53	C-2164	36.15	-0.1167	2145	23
C-8308	36.2	-0.3667	1820	32	C-2311	36.1833	0.1167	1524	55
C-2851	36.1167	-0.5833	2012	235	C-9345	36.3444	-0.6767	1950	71
C-9359	36.0444	-0.1139	1980	97	C-7379	35.5833	-0.3333	1580	138
C-2234	36.2167	-0.5833	1990	79	C-7380	35.5833	-0.3333	1580	135
C-2332	36.2667	-0.2667	2362	56	C-1873	35.7667	-0.2167	2324	153
C-2388	36.3167	-0.4833	2056	243	C-2505	35.7333	-0.2333	2500	43
C-3010	36.2667	-0.2	2697	12	C-2970	36.15	-0.2833	1911	29
C-7630	36.3333	-0.4333	2200	157	C-3150	35.7	-0.2333	2621	38
C-8021	36.3167	-0.4333	2175	127	C-5276	35.75	-0.2833	2420	50
C-2773	36.3667	-0.3833	2134	23	C-5753	36.15	-0.1333	2130	18
C-2775	36.3667	-0.3833	2103	42	C-6664	35.9667	-0.3167	2110	90
C-1361	36.3667	-0.4	2286	188	C-6929	35.6833	-0.2	2620	19
C-2499	36.25	-0.3667	1938	106	C-2545	35.7	-0.55	2591	46
C-13910	36.1747	-0.5653	1960	83.6	C-2578	35.7333	-0.5167	2652	45
C-8891	35.9667	-0.1333	1980	210	C-2553	35.75	-0.2333	2423	67
C-7377	36.15	-0.2	2000	82	C-9362	36.2944	0.4833	1900	110
C-11093	36.5328	0.7933	1940	59.9	C-4639	36.1833	-0.0167	1900	2
C-6520	36.4667	-0.6833	2125	112	C-9344	36.4778	-0.6903	2120	100
C-10708	36.4306	-0.7944	1920	20.7	C-9347	36.4833	-0.6625	2180	130
C-3431	36.1167	-0.6333	2316	116	C-10816	35.4567	-0.5083	2120	138.1
C-10809	36.1428	-0.2817	1890	37.3	C-1947	36.45	-0.7333	1920	16
C-10706	36.5358	-0.8	2460	96.2	C-1970	36.1833	-0.9167	2499	130
C-6300	36.5167	-0.7667	2410	132	C-2017	36.3833	-0.8167	1892	16
C-2160	36.5	-0.3833	2453	136	C-2220	36.4333	-0.7667	1615	30
C-4547	36.0833	-0.15	1855	100	C-2246	36.4	-0.6833	1903	14
C-4116	36.05	-0.4833	2100	160	C-2304	36.2833	-0.75	1935	5
C-10296	36.1194	-0.2944	1780	96	C-2347	36.4667	-0.7333	2073	119
C-4493	36.1333	-0.1333	2060	12	C-2997	36.4	-0.9	2164	280
C-5143	36.1167	-0.2667	1878	35	C-3551	36.4	-0.7	1897	5
C-6355	36.15	-0.3333	1897	122	C-3924	36.35	-0.0833	1888	7
C-8022	36.1333	-0.05	1880	106	C-3929	36.3667	-0.6167	1896	16

Piezometric Data for Larger Nakuru County (Continued)

BH-No.	DLONG.	DLAT.	ALT.(m)	W.R.L.(m)	BH-No.	DLONG.	DLAT.	ALT.(m)	W.R.L(m)
C-3932	36.1333	-0.7	2255	125	C-2930	36.1	-0.2833	1842	91
C-4155	36.4333	-0.6667	1929	27	C-2129	36.1667	-0.2833	1928	49
C-4161	36.4167	-0.7	1900	16	C-2493	36.2	-0.3167	1920	94
C-4168	36.4167	-0.65	2083	17	C-8996	36.2833	-0.75	2100	9
C-4177	36.4	-0.65	1920	16	C-2210	36.2333	-0.3333	1966	52
C-4208	36.4167	-0.7167	1889	6	C-2276	35.9333	-0.4	2316	33
C-4301	36.4167	-0.65	1920	33	C-2619	35.9333	-0.3667	2561	80
C-4600	36.25	-0.6667	1920	45	C-3490	35.9167	-0.3667	2286	107
C-5002	36.4667	-0.6333	2230	108	C-4206	35.9333	-0.3333	2100	100
C-5324	36.2	-0.3833	1810	16	C-4214	35.9333	-0.3667	2162	103
C-6379	36.4333	-0.7667	1951	60	C-4506	36.95	-0.3167	2120	121
C-6924	36.4333	-0.7333	1982	95	C-4785	35.9167	-0.35	2070	52
C-8994	36.4167	-0.6667	1899	15	C-4919	35.85	-0.2833	2130	82
C-8995	36.4167	-0.6667	1900	17	C-5017	35.85	-0.2167	1860	21
C-9351	36.4417	-0.7917	1926	42	C-5206	35.9333	-0.3667	2215	34
C-9352	36.4472	-0.7556	1885	78	C-5547	36.0166	0	1950	186
C-9357	36.4406	-0.7231	1930	76	C-6032	35.9333	-0.3667	2200	70
C-1850	36.6	-0.7	2530	140	C-6205	35.9833	-0.2167	2040	40
C-2706	36.3	-0.7	1920	39	C-6206	35.9	-0.35	2330	35
C-9356	36.4436	-0.725	1875	109	C-6314	35.9167	-0.3333	2160	110
C-3292	36.4167	-0.7167	1897	8	C-7627	35.9333	-0.2667	2290	104
C-1830	36.55	-0.6667	2478	128	C-8167	36	-0.3	2050	92
C-2005	36.5667	-0.7833	2591	241	C-8515	35.9333	-0.3833	2250	102
C-2062	36.5667	-0.7833	2621	228	C-9065	36.5	-0.55	2400	105.3
C-4157	36.4333	-0.7167	1900	11	C-1585	35.9167	-0.3833	2179	87
C-2069	36.3	-0.8167	1890	46	C-1934	35.9333	-0.3333	2167	97
C-2076	36.3333	-0.4833	2042	121	C-2448	35.65	-0.45	2179	156
C-2077	36.35	-0.4833	1981	96	C-3627	35.95	-0.3333	2143	100
C-2058	36.4333	-0.7667	1895	15	C-2745	35.9167	-0.35	2346	92
C-2015	36.3333	-0.8167	1890	12	C-3559	35.9667	-0.3333	2145	104
C-2539	36.3333	-0.7167	1905	5	C-2432	35.9833	-0.35	2248	117
C-3299	36.4	-0.7	1897	2	C-2894	35.95	-0.3833	2194	12
C-3024	36.1333	-0.6833	2438	93	C-2670	36	-0.3	1981	167
C-2661	36.2667	-0.7667	1890	21	C-2607	36.5333	-0.1167	2560	132
C-2657	36.25	-0.7833	1890	23	C-9341	36.4917	0.075	2195	206
C-2659	36.2833	-0.7833	1890	8	C-9346	36.4583	0.6917	2100	135
C-2701	36.2667	-0.65	1890	7	C-10814	35.9911	-0.1806	2000	221.1
C-3164	36.15	-0.6833	2484	19	C-2250	36.3333	-0.15	2591	88
C-2667	36.55	-0.7667	2347	155	C-1951	36.4167	-0.4	2347	112
C-2709	36.1833	-0.8333	2133	196	C-1952	36.4167	-0.3833	2303	112
C-1892	35.7	-0.4833	2195	233	C-10703	36.37	-0.2683	2560	30.8
C-2128	36.15	-0.2833	1875	32	C-1902	36.45	-0.2167	2347	8
C-2269	36.1333	-0.3	1859	61	C-1891	36.4333	-0.2167	2355	14.9
C-2278	36.0667	-0.2833	1874	102	C-1924	36.3833	-0.3833	2347	125
C-2409	36.15	-0.2333	1951	98	C-4366	36.033	0.8167	1900	11
C-2984	36.1167	-0.0833	1798	32	C-9339	36.4406	-0.7175	1880	44
C-2996	36.15	-0.1667	2073	64	C-1869	35.85	-0.2333	1960	64
C-3288	36.0667	-0.05	1664	161	C-4404	35.9333	-0.15	1800	126
C-3797	36.0833	-0.1333	1874	23	C-9067	35.8636	-0.1719	1835	21
C-2853	35.8	-0.2	2042	101	C-2563	35.85	-0.2167	1921	20
C-719	36.1333	-0.2833	1859	65	C-2564	35.85	-0.25	2073	110
C-1807	36.1167	-0.1667	1844	65	C-2170	36.6333	-0.6833	2609	187
C-3361	36.2	-0.1833	2356	101	C-1786	36.0667	-0.0833	1701	101
C-2946	36.1833	-0.1833	2164	18	C-2309	36.15	-0.05	1943	87
C-2784	36.1667	-0.45	1951	6	C-2398	36.15	-0.1333	2118	30
C-2131	35.8167	-0.2333	1852	29	C-3018	36.1833	0.1	1524	44
C-2504	36.1833	-0.2833	1951	70	C-3432	36.15	0.0333	1524	15
					C-3535	36.1333	-0.1	1830	27